NATIONAL DEVELOPMENT PLAN 2020 | EUROPEAN UNION European Regional Development Fund | UNIVERSITY OF LATVIA | ASI

INVESTING IN YOUR FUTURE

ERDF project No. 1.1.1.1/18/A/132

"Multimodal imaging technology for in-vivo diagnostics of skin malformations"

MIDTERM REPORT
on the project activities performed during May 2019 - October 2020

Contents

A1.1. *Comparative laboratory tests of the equipment for MSDRI measurements*

May - October 2019

The main contributors: Dr.phys. Ilona Kuzmina, PhD student Ilze Oshina and BSc student Laura Ozolina

Protocol of the test results

A comparative study was performed for four imaging devices:

1. *Nuance EX* (commercial hyperspectral camera),
2. *SkImager* (laboratory prototype),
3. Smartphone *Nexus5* with *RGB LED* (LED) illuminator (laboratory prototype),
4. Smartphone *Nexus5* with *three wavelength laser* (Laser) illuminator (laboratory prototype).

Spectra of the light sources for the imaging devices were measured using *Avaspec-2048-USB2* spectrometer. Hyperspectral and RGB images were captured from 24 colour checker areas (*Xrite Color Checker Classic*). Images were captured three times from each square. Settings of *Nuance EX* and *SkImager* are given in Table 1-1, settings of the smartphone devices – in Table 1-2. Two smartphone applications – *AZ Camera* and *SkinViewer* - were used for image capturing by smartphone prototypes. Both apps were used for image capturing by LED illuminator: *SkinViewer* was used to analyse settings experimentally adjusted for in vivo measurements, *AZ Camera* app was used to adjust exposition in order to meet the tabulated values of the grey square (Ch20) of the colour checker. *AZ Camera* was also used for image capturing by Laser illuminator to analyse the influence of settings experimentally adjusted for in vivo measurements. *MatLab* software were used

for mean intensity reading from the manually selected region of interest in the image. Images of all 24 squares and grey squares (No. 19 – 24) of the colour checker were analysed for each channel (R, G and B) of the prototype camera under corresponding illumination (R channel of the camera at red illumination, G channel of the camera at green illumination, B channel of the camera at blue illumination).

Table 1-1. Settings of the hyperspectral camera *Nuance EX* and *Skimager*

Device	**Nuance EX**	**SkImager**
Exposition time	Auto (reference square No.20)	
	Wavelength (nm)	
R	665	667
G	530	530
B	460	462

Table 1-2. Settings of the smartphone devices.

Device	**Nexus5+RGB LED**		**Nexus5+Laser**
Smartphone App	***AZ Camera***	***SkinViewer***	***AZ Camera***
White balance	6609K	-	6647K
ISO	100	100	100
Exposition time (s)			
t_R	0.08	0.02	0.25
t_G	0.06	0.02	0.25
t_B	0.04	0.02	0.25
Wavelength (nm)			
R	663		659
G	535		532
B	460		448

Results

Fig.1-1 shows spectra of the light sources of the imaging devices.
Fig.1-2, 3 and **4** show the intensity distribution on the illumination area for R, G, B channels of the laboratory prototypes.
Fig.1-5. compares mean (a, c, e) and normalized (b, d, f) values obtained from grey scale squares of the colour checker by three prototypes for the settings experimentally adjusted for *in vivo* measurements in previous studies.
Fig.1-6 compares mean (a, c, e) and normalized (b, d, f) values obtained from all 24 squares of the colour checker by three prototypes for the settings experimentally adjusted for *in vivo* measurements in previous studies.
Fig.1-7. illustrates the difference of measured mean intensity values obtained by the prototypes from reference values for grey scale (a, c, e) and all squares of the colour checker (b, d, f).
Fig.1-8 compares results (mean and normalized values) obtained by smartphone RGB LED prototype at settings experimentally adjusted for in vivo measurements (*SkinViewer* App) with results obtained at exposition time adjusted to the reference RGB values of the grey square No.20 of the colour checker using *Camera AZ* App.
Fig.1-9 illustrates the difference of measured mean intensity values from reference values for two type of settings (experimentally selected for in vivo measurements and adjusted to the grey colour checker square No.20) of the smartphone RGB LED prototype (fig.9).
Fig.1-10 shows the dependence of the mean values obtained from the grey scale (a, c, e) and all squares (b, d, f) by *Nuance EX* at 665nm, 530nm, 460nm on the reference values.

Fig.1-11 compares the results obtained at 665nm, 530nm, 460nm from the grey scale (a) and all squares (b) by *Nuance EX*.
Fig.1-12 compares the results obtained by prototypes with results obtained by *Nuance EX* at 665nm, 530nm, 460nm from all squares.
Fig.1-13 compares the results obtained by prototypes with results obtained by *Nuance EX* at 665nm, 530nm, 460nm for grey scale of the colour checker.
Fig.1-14 illustrates the difference of measured mean intensity values obtained by prototypes from the values obtained by *Nuance EX* at 665nm, 530nm, 460nm for grey scale of the colour checker.

I. *Emission spectra of the light sources*

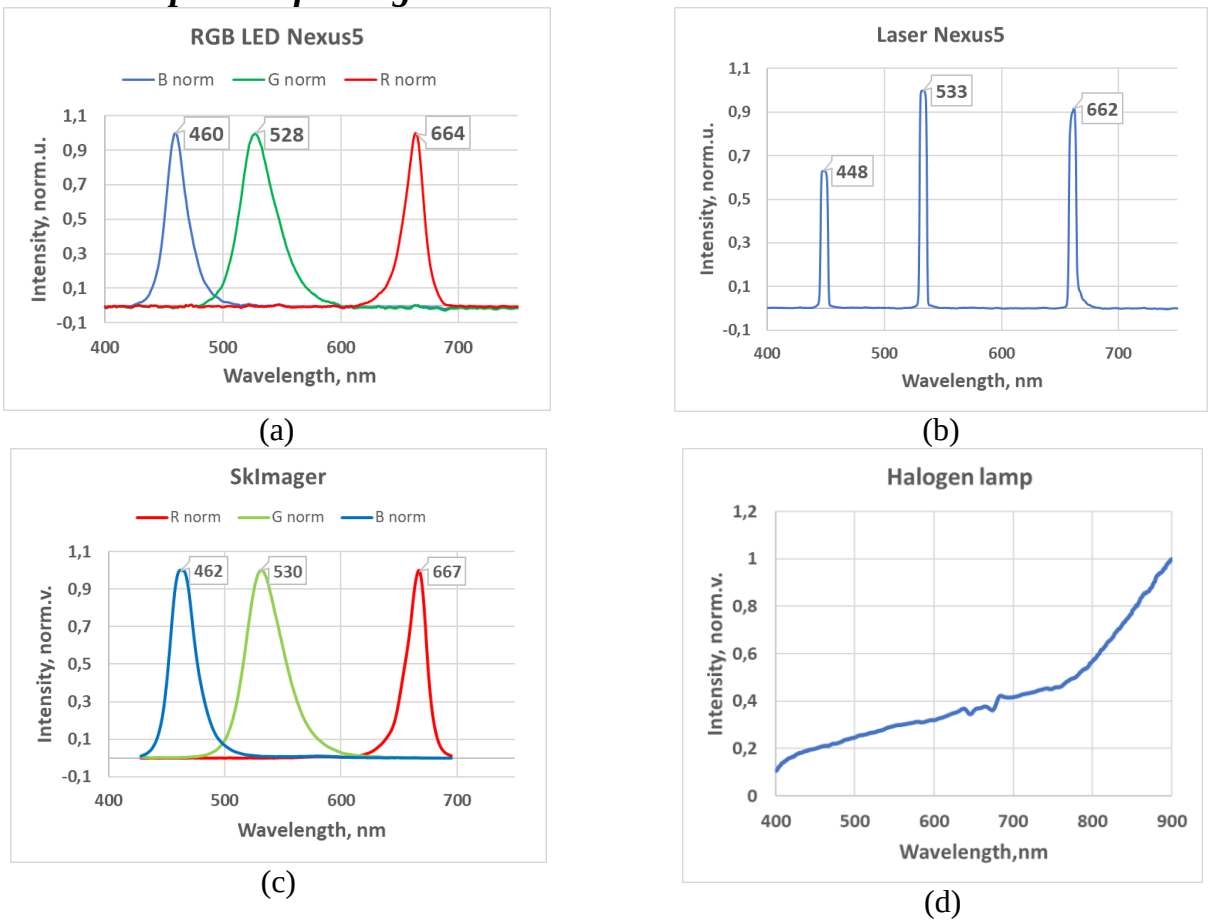

Fig.1-1. Normalized spectra of the light sources: smartphone prototypes (a, b), *SkImager* (c) and *Nuance EX* (d).

II. *Intensity distributions on the illumination area*

1. LED prototype

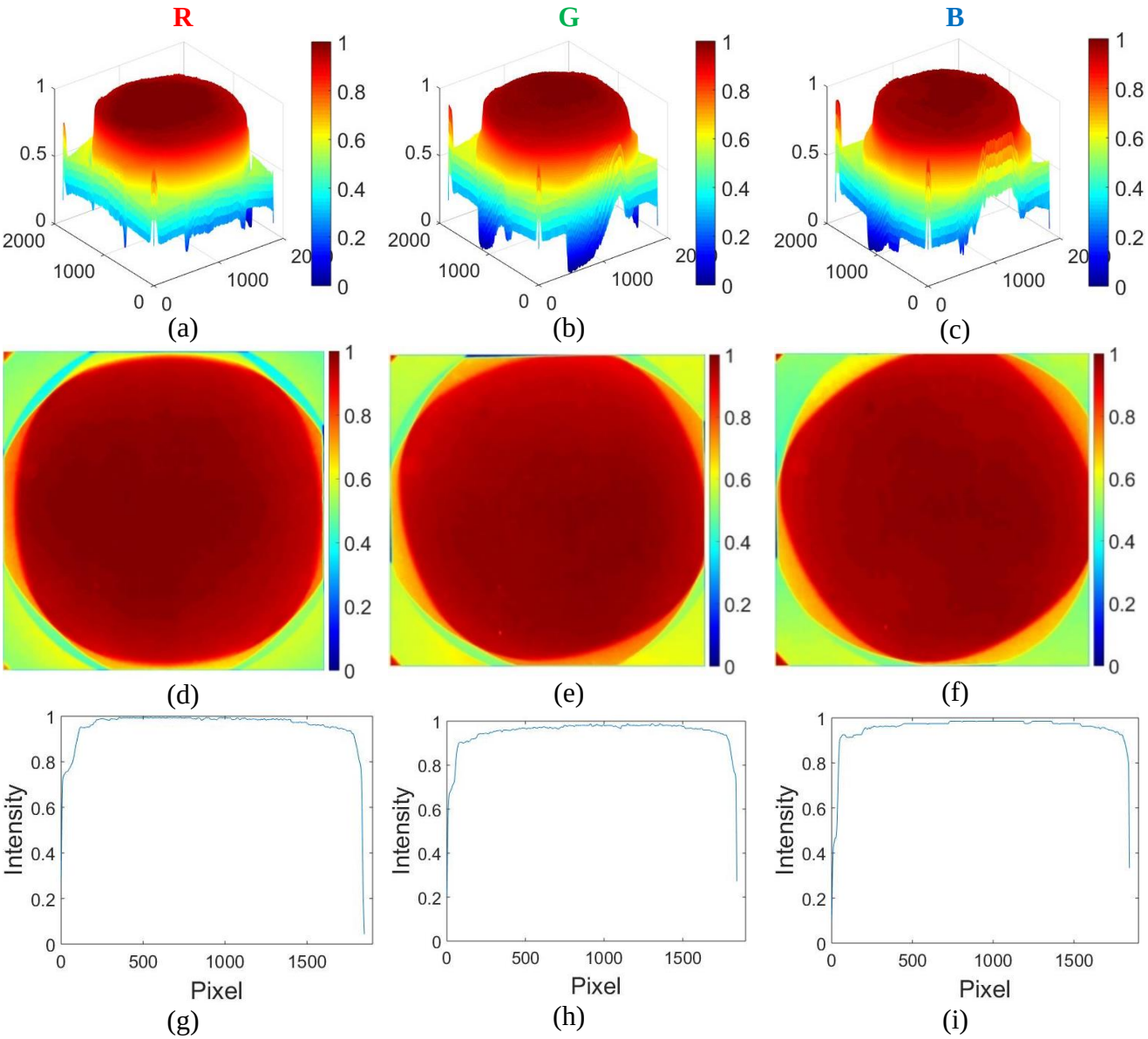

Fig.1-2. Intensity distribution (normalized) on the area of the LED smartphone prototype: 3D representation (a,b,c), x-y plane (d,e,f), intensity profile (g,h,i).

2. Laser prototype

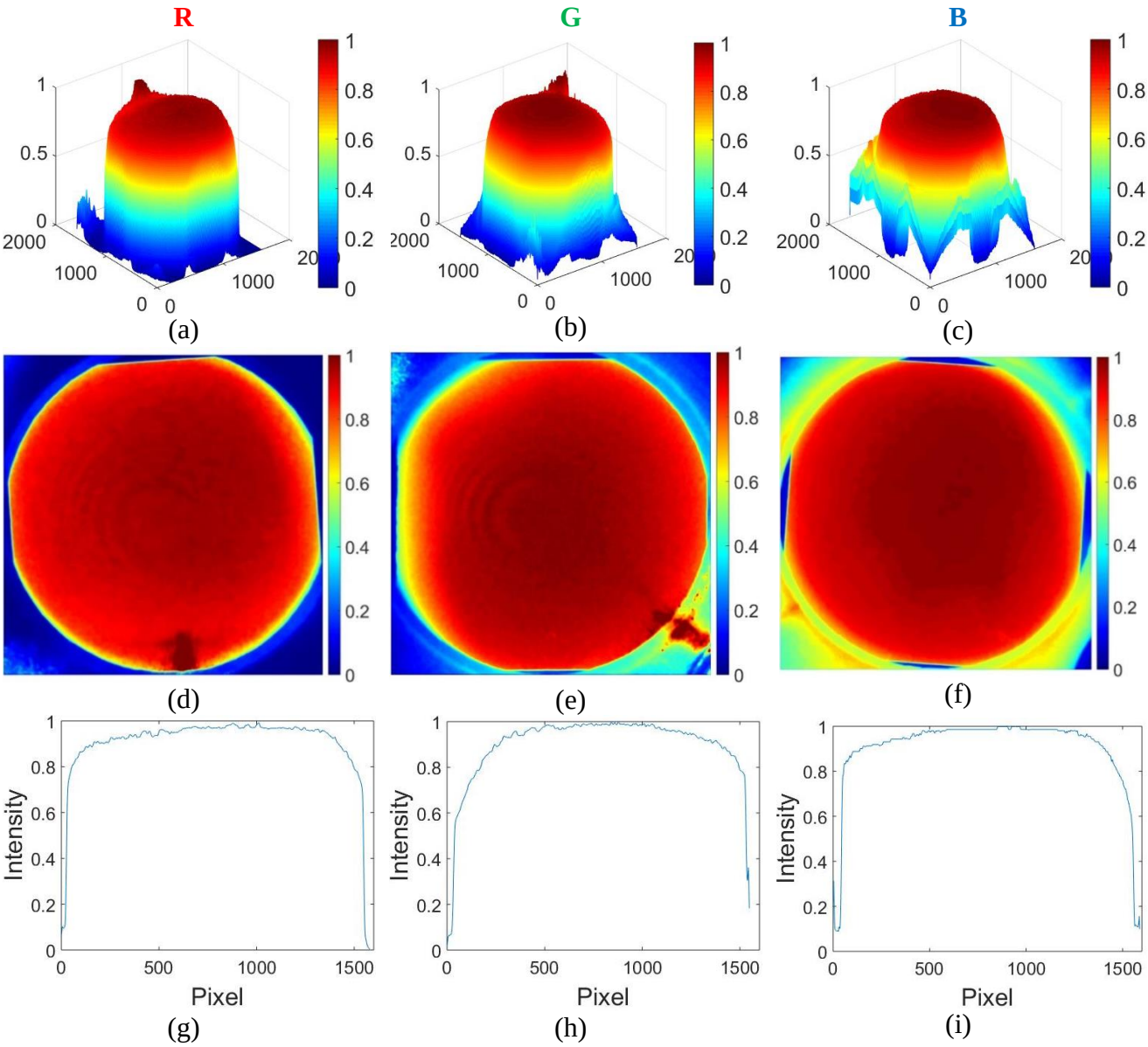

Fig.1-3. Intensity distribution (normalized) on the area of the Laser prototype 3D representation (a,b,c), x-y plane (d,e,f), intensity profile (g,h,i).

3. SkImager prototype

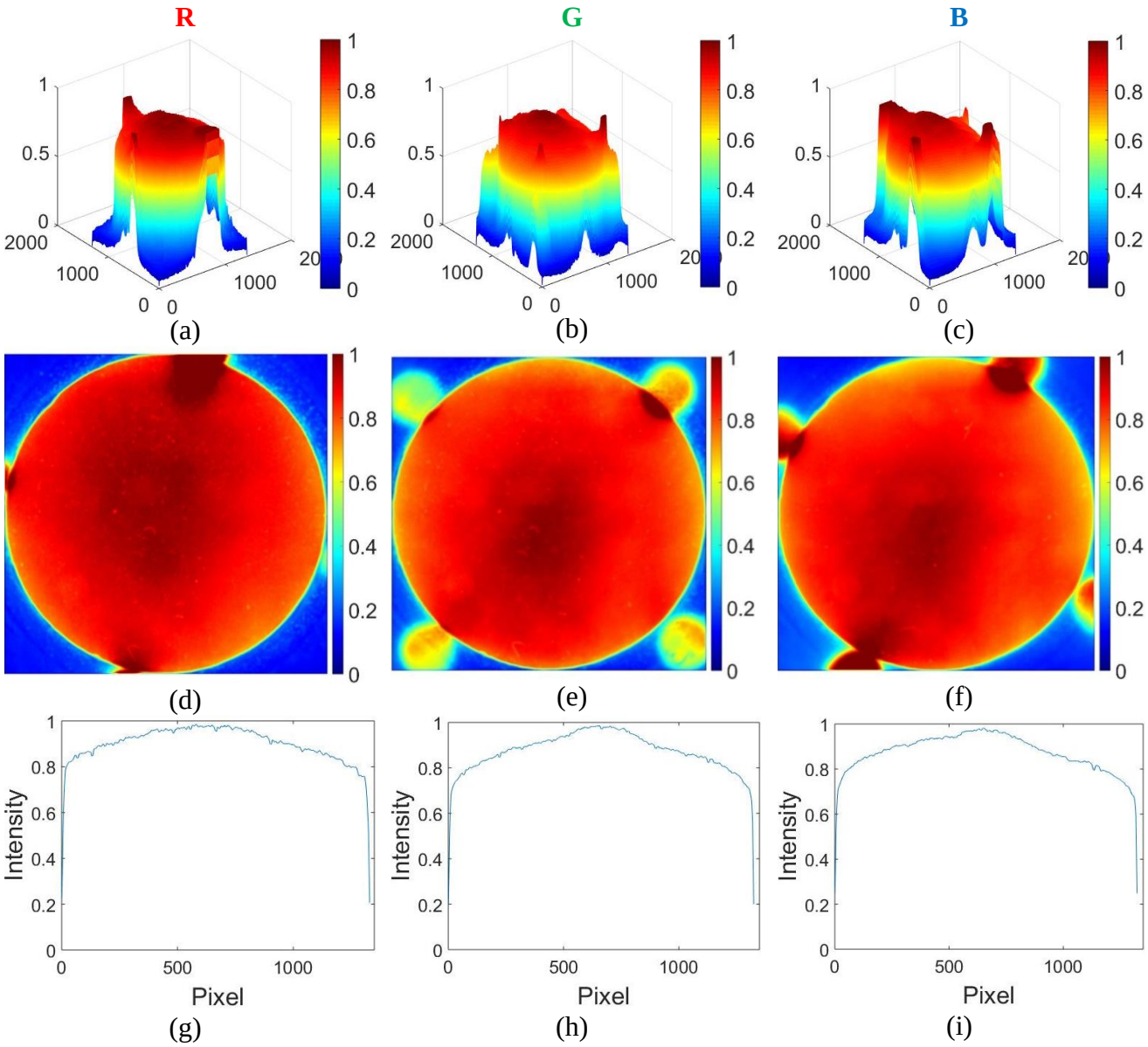

Fig.1-4. Intensity distribution (normalized) on the area of the SkImager prototype: 3D representation (a,b,c), x-y plane (d,e,f), intensity profile (g,h,i).

III. *Results of the colour checker imaging*

1. Three prototypes (smartphone LED and Laser, SkImager)

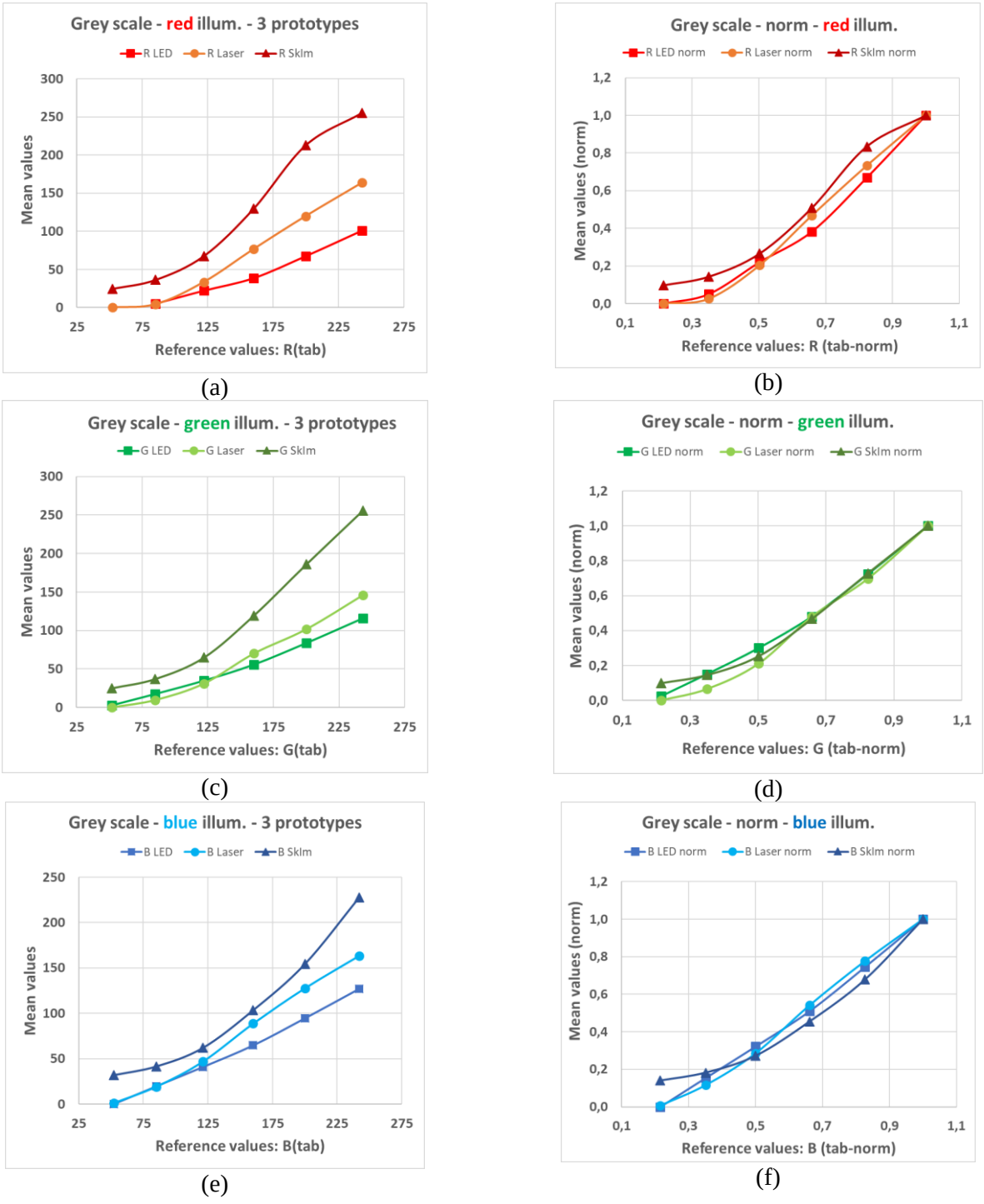

Fig.1-5. A comparison of the three prototypes. The dependence of the mean (a,c,e) and normalized values (b,d,f) on the reference values for grey scale squares of the color checker. **R, G, B** – red, green, blue channel; **LED** – LED illuminator; **Laser** – laser illuminator; **SkIm** – SkImager, **norm** – normalized data

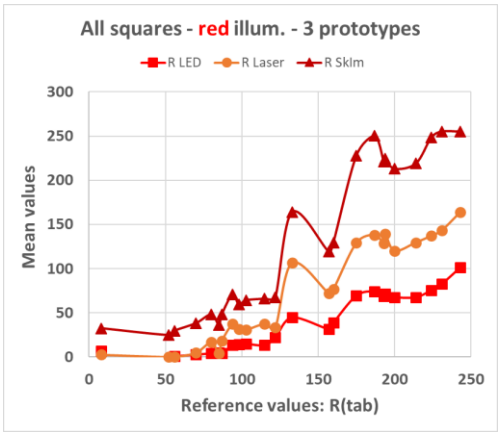

(a)

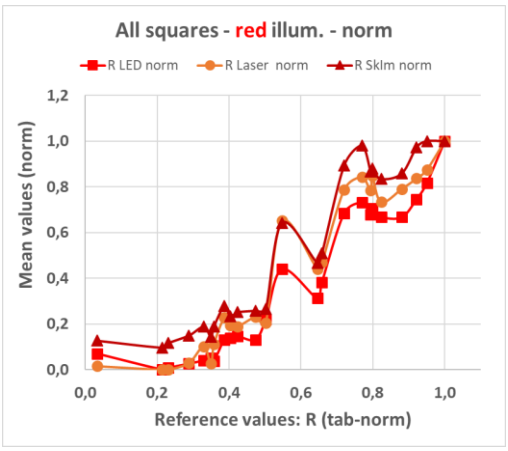

(b)

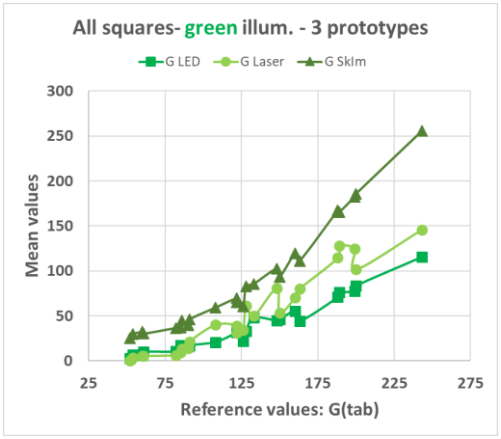

(d)

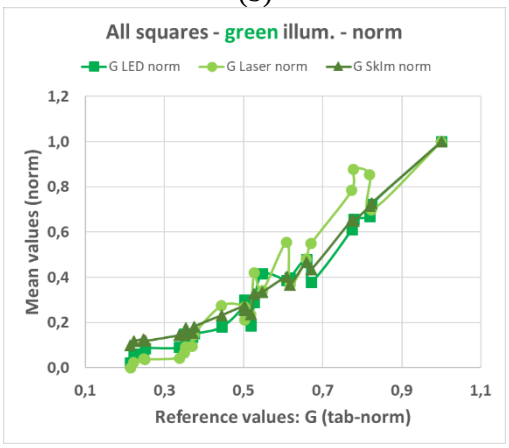

(e)

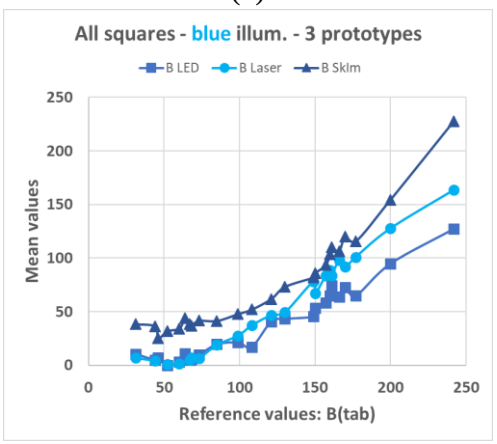

(g)

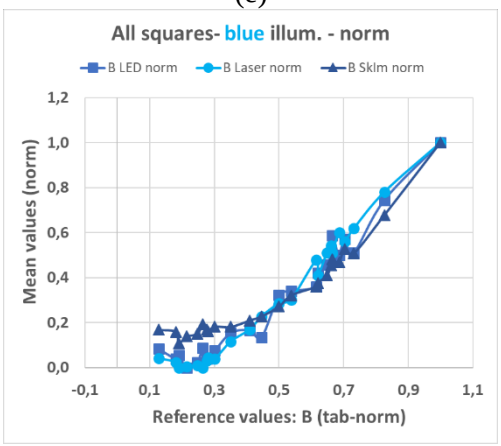

(h)

Fig.1-6. A comparison of the three prototypes. The dependence of the mean (a,c,e) and normalized values (b,d,f) on the reference values for all squares of the color checker. **R, G, B** – red, green, blue channel; **LED** – LED illuminator; **Laser** – laser illuminator; **SkIm** – SkImager, **norm** – normalized data

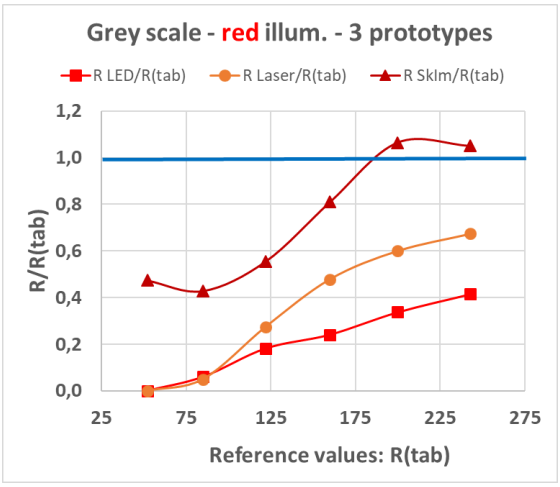

(a)

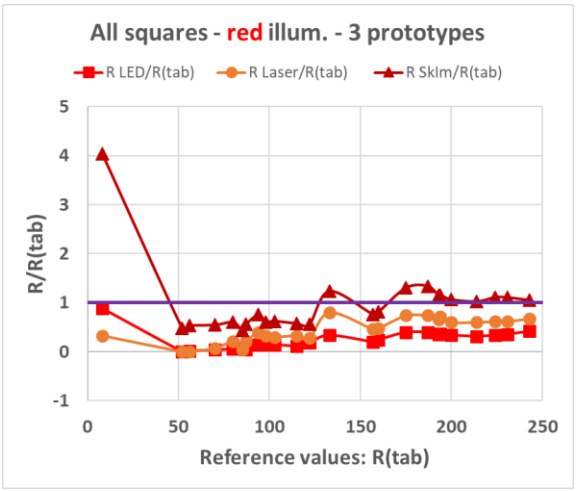

(b)

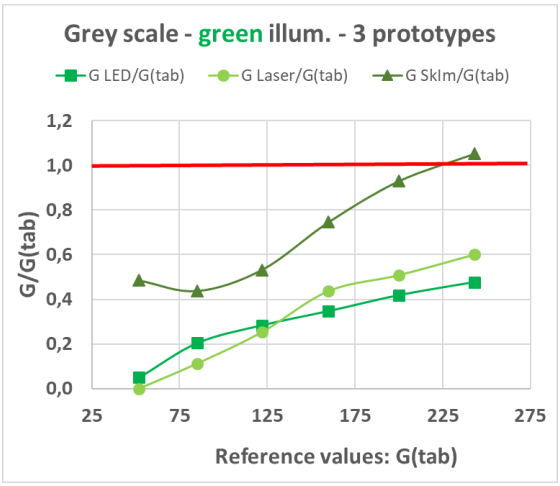

(c)

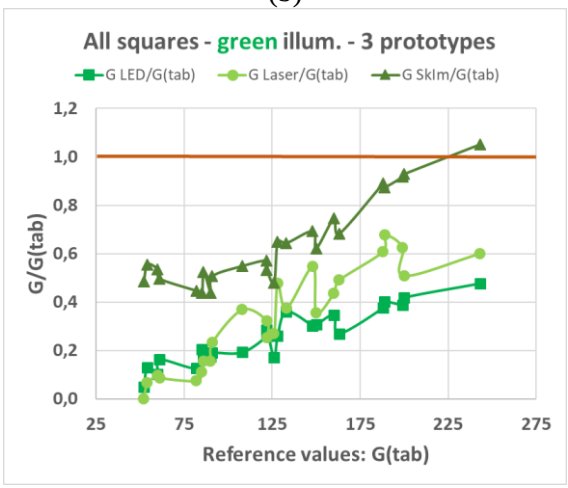

(d)

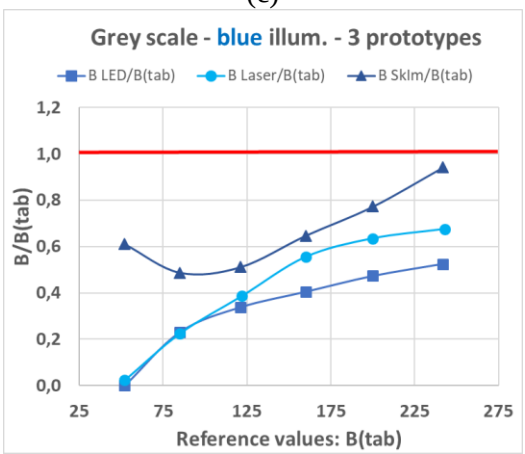

(e)

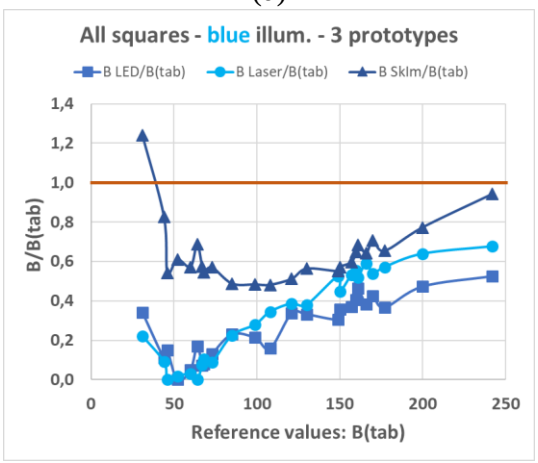

(f)

Fig.1-7. Comparison of the three prototypes: the diference of the mesured values from reference (tabulated) values for gray scale squares (a,c,e) and all squares (b,d,f) of the color checker. **R, G, B** – red, green, blue channel; **LED** – RGB LED illuminator; **Laser** – laser illuminator; **SkIm** – SkImager

2. Smartphone LED illuminator

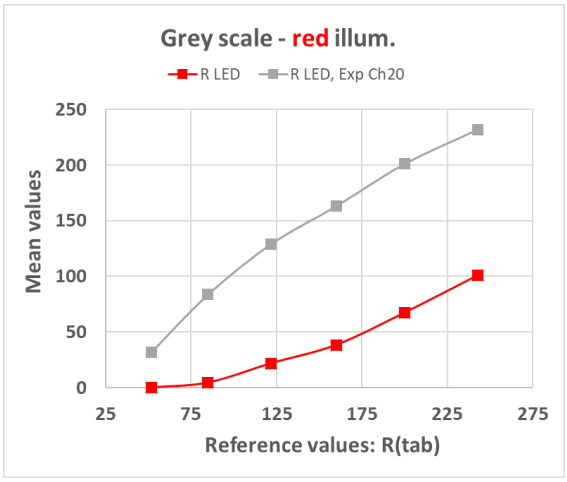

(a)

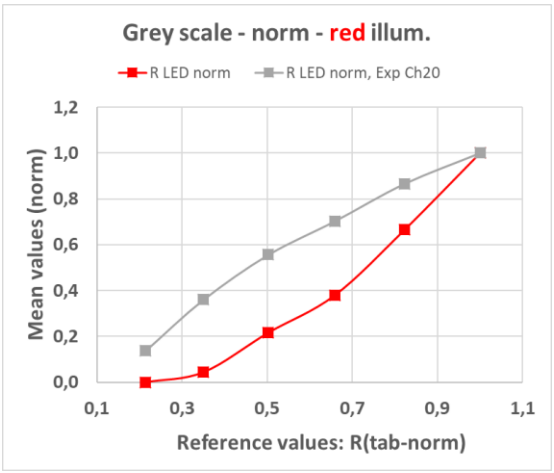

(b)

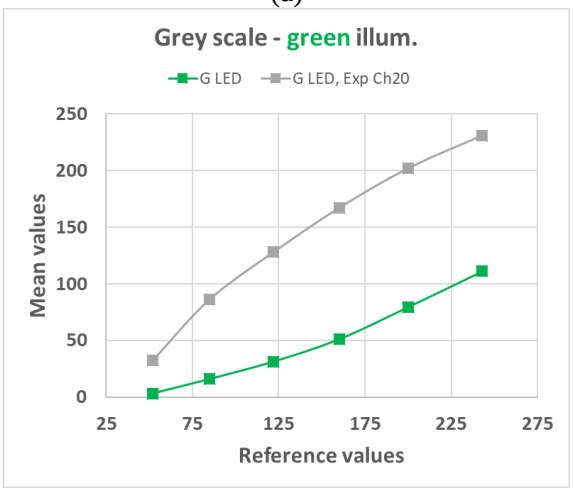

(c)

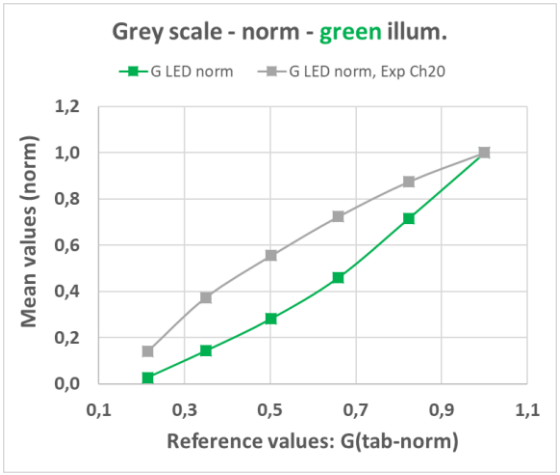

(d)

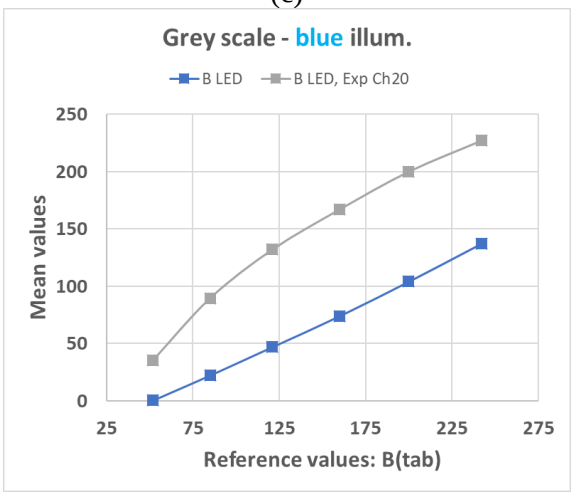

(e)

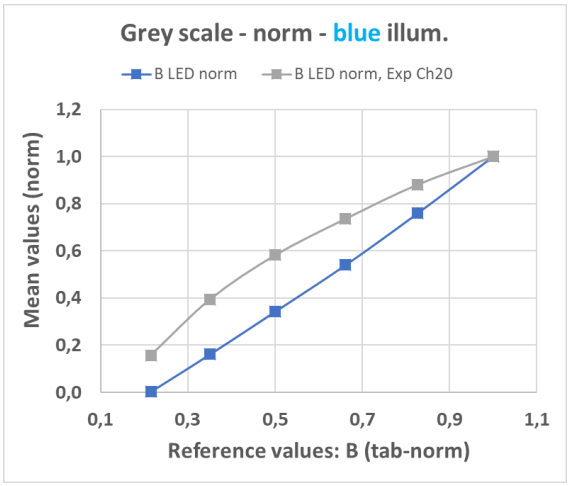

(f)

Fig.1-8. The influence of exposition on the mean (a,c,e) and normalized (b,d,f) values of RGB LED prototype. **R, G, B** – red, green, blue channel; **LED** – RGB LED illuminator; **Exp Ch20** – an exposition ajusted to the value of the square (Ch20) of the colour checker.

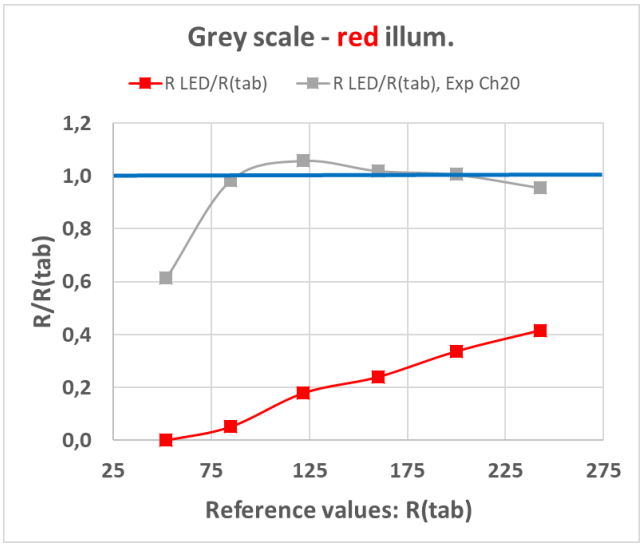

(a)

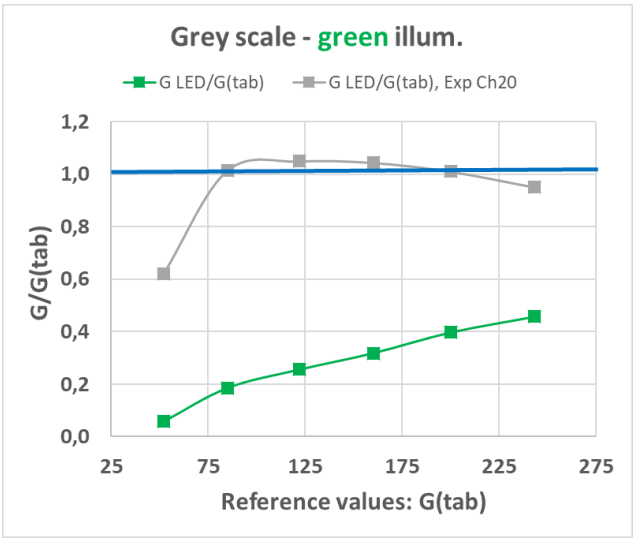

(b)

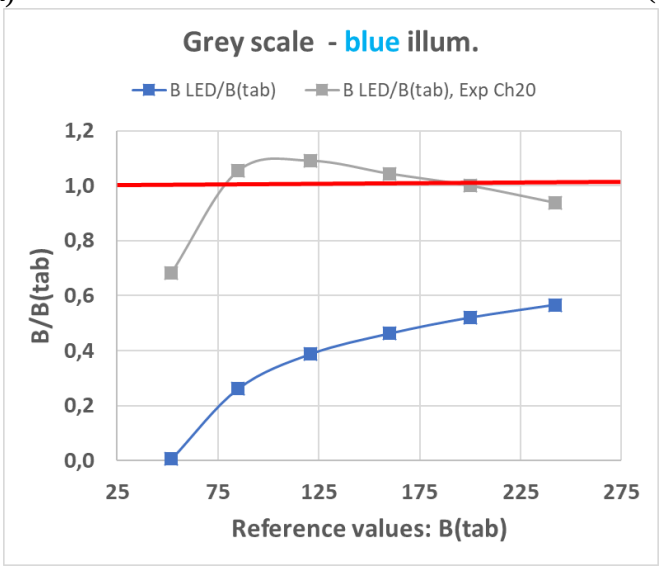

(c)

Fig.1-9. Comparison of two expositions. The diference of the mesured values from the reference (tabulated) values for the grey scale squares of the colour checker. **R, G, B** – red, green, blue channel; **LED** – RGB LED illuminator

3. Nuance EX compared to the laboratory prototypes

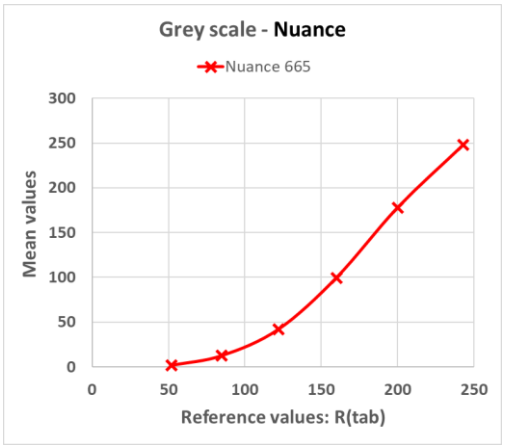

(a)

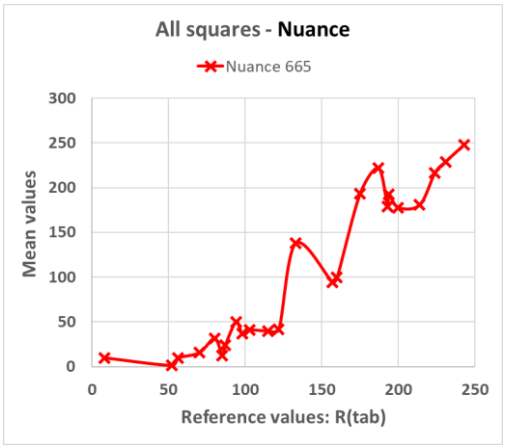

(b)

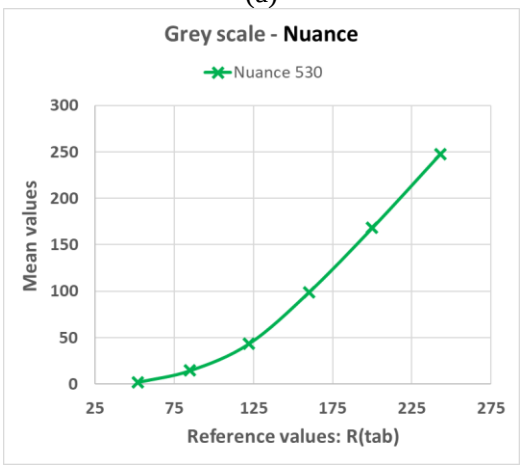

(c)

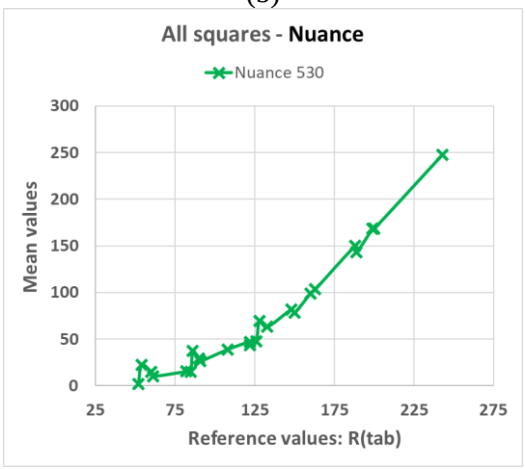

(d)

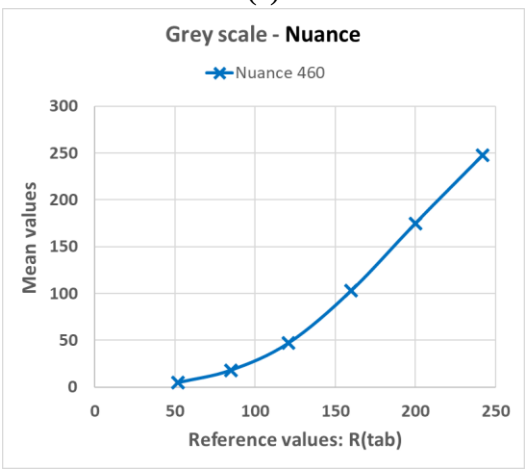

(e)

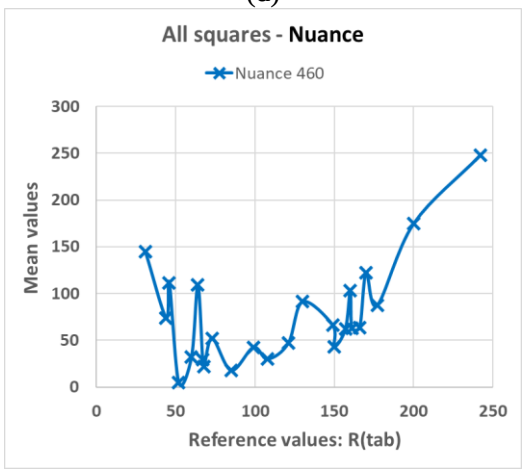

(f)

Fig.1-10. The dependence of the mean and normalized values measured at 665nm (Nuance 665), 530nm (Nuance 530) and 460nm (Nuance 460 by *Nuance EX* on the reference values for all and grey scale squares.

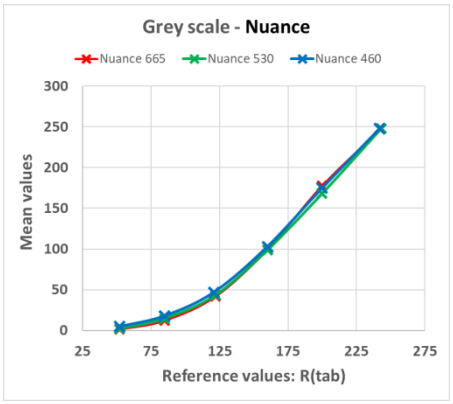

(a)

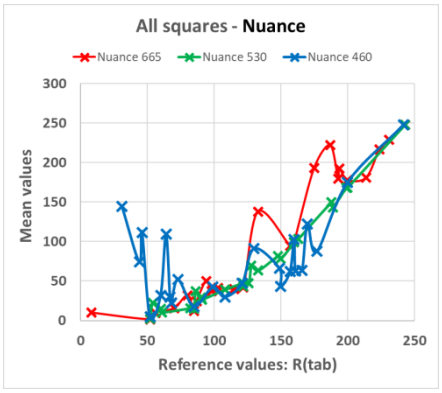

(b)

Fig.1-11. The dependence of the mean and normalized values measured at 665nm (Nuance 665), 530nm (Nuance 530) and 460nm (Nuance 460 by *Nuance EX* on the reference values for all and grey scale squares.

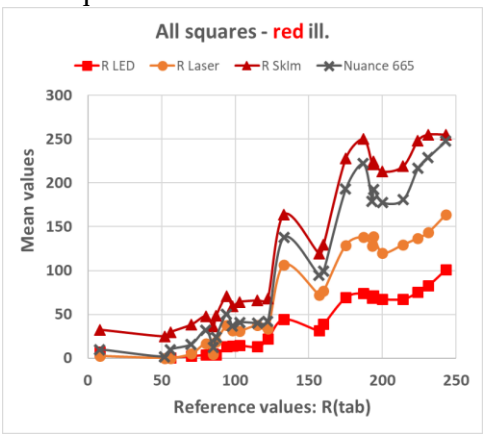

(a)

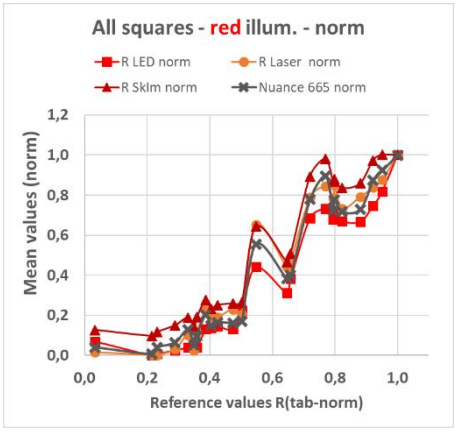

(b)

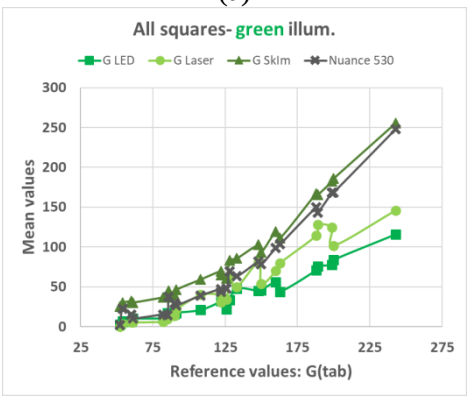

(c)

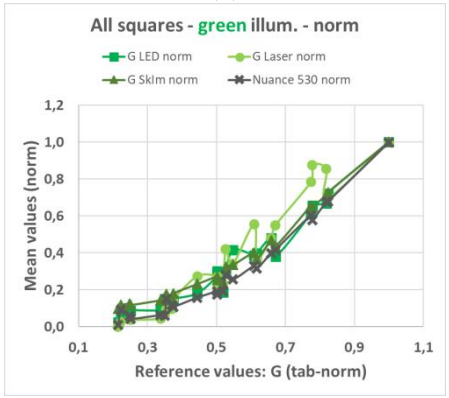

(d)

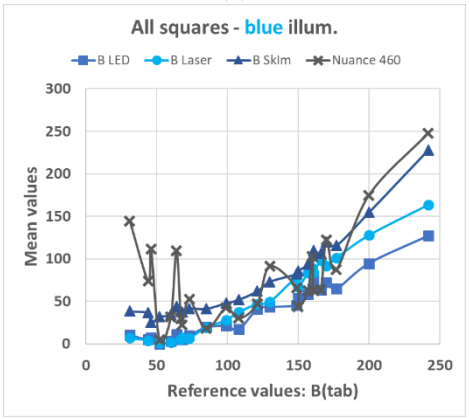

(e)

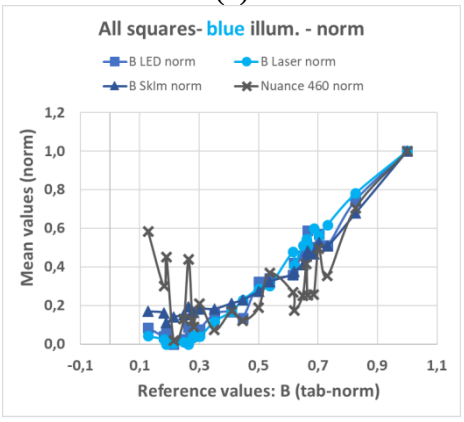

(f)

Fig.1-12. Comparison of the three prototypes with *Nuance EX* camera.The dependence of the measured mean and normalized values on the reference values for all squares.

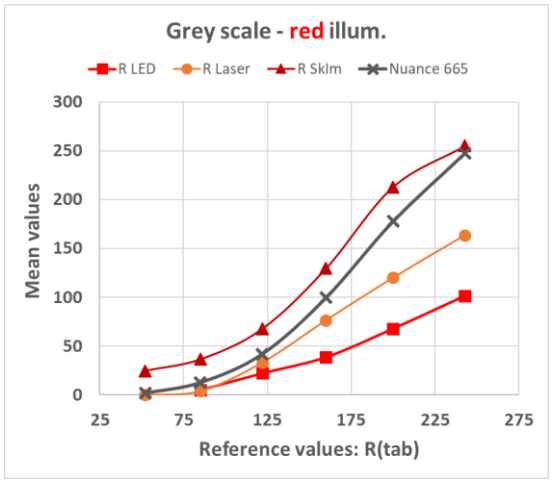

(a)

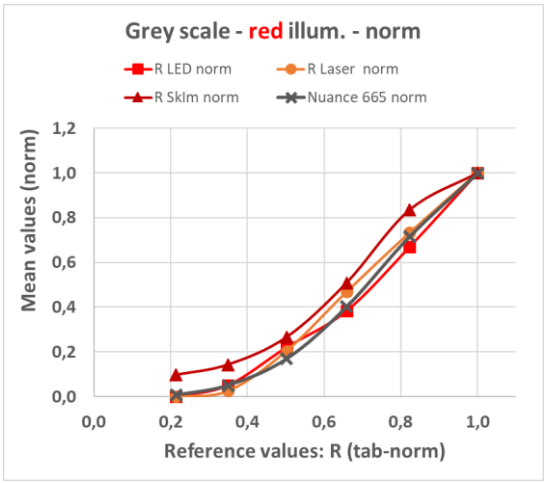

(b)

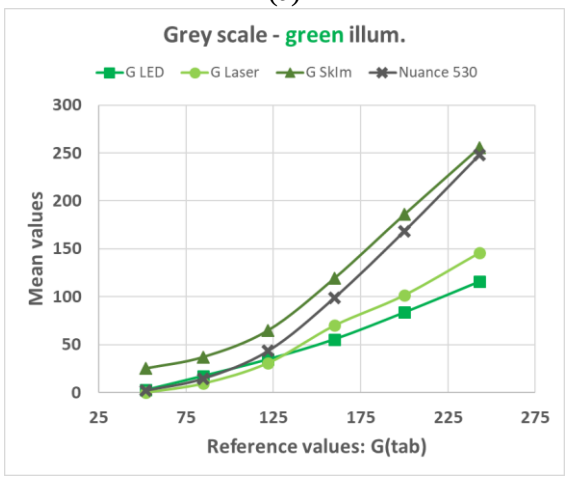

(c)

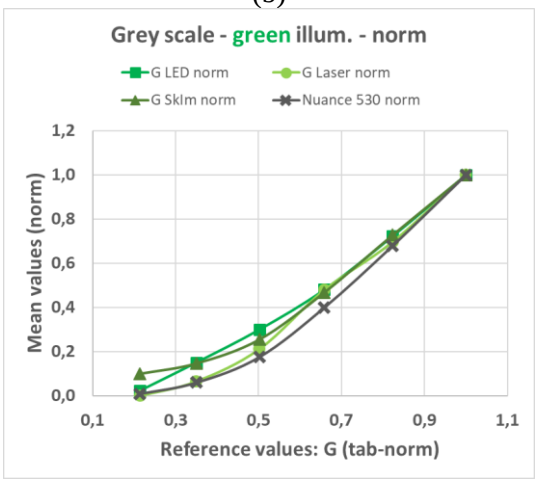

(d)

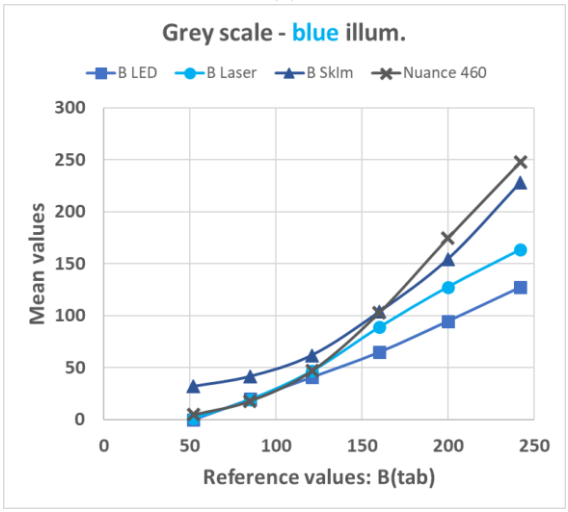

(e)

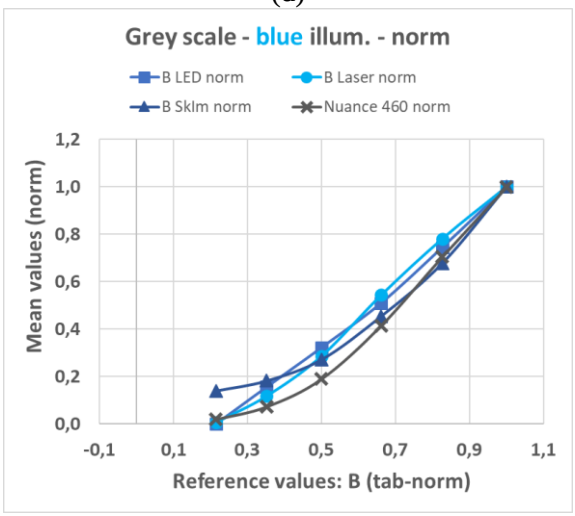

(f)

Fig.1-13. Comparison of the three prototypes with *Nuance EX* camera.The dependence of the measured mean and normalized values on the reference values for the grey scale squares.

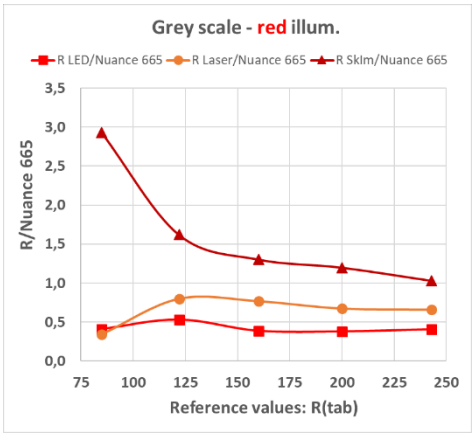

(a)

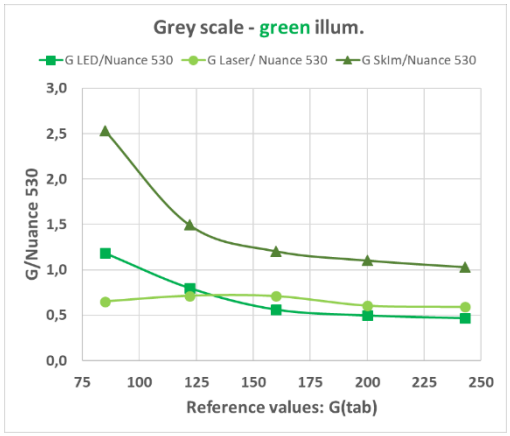

(b)

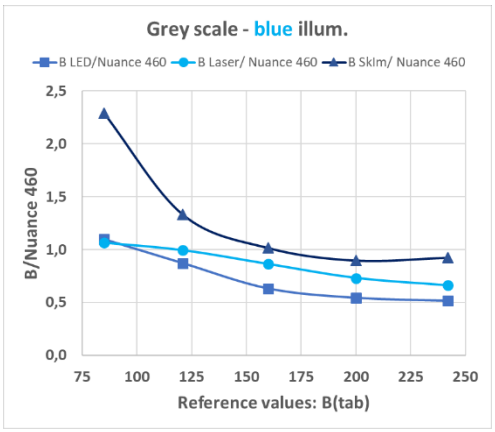

(c)

Fig.1-14. Comparison of the three prototypes with *Nuance EX* camera.The dependence of the measured mean and normalized values on the reference values for the grey scale squares.

Summary and conclusions

1. Smartphone-based devices show very similar mean intensity values for each square of the grey scale while the *SkImager* gives higher intensity values compared to the smartphone-based devices (fig.A1-5 (a, c, e)). After normalization to the maximal value all three curves overlap (fig.A1-5 (b, d, f)).
2. The *SkImager* also gives higher values for all 24 squares compared to smartphone-based devices (fig.A1-6), however the shapes of curves are similar. The dependence of measured values on the reference values is more linear for G and B camera channel (fig.A1-6(d, g)).
3. Intensity measured by the LED prototype corresponds to the reference values (ratio G/G(tab) value is close to "1") at exposition adjusted to the value of the grey square (Ch20) (fig.A1-9), but experimentally selected settings give lower intensity values compared to the reference and linear dependence for the grey scale squares.
4. Intensity values measured at 665nm and 530nm by the *Nuance EX* are very close but lower compared to the values of the *SkImager* (fig.A1-12,13). After normalization to the maximal value curves obtained by all devices from the squares of the grey scale overlap.
5. The difference of the intensity values obtained by smartphone-based prototypes and *Nuance EX* is almost constant for the most squares of the grey scale while the difference of the *SkImager* and *Nuance EX* values increases for squares with lower reference values (fig.A1-14).
6. Both smartphone-based devices are selected for further clinical measurements using MSDRI technique.

Publicity

A1.1 results were **reported** at the SPIE/BIOS conference "Multimodal Biomedical Imaging" in San Francisco, USA (February, 2020) and at the 78th International conference of University of Latvia in Riga (February, 2020), and **published** in a SCOPUS-cited paper:

- J.Spigulis, I.Kuzmina, V.Lukinsone et.al, "Towards combined multispectral, FLIM and Raman imaging for skin diagnostics", *Proc.SPIE* **11232**, 112320N-1 (2020).

A1.2. *Determination of the remitted photon path length distributions at particular wavelengths by picosecond kinetic measurements on tissue phantoms*

May 2019 – April 2020

The main contributors: Dr.phys. Vanesa Lukinsone, MSc student Anna Maslobojeva, Dr.phys. Ilona Kuzmina, Dr.phys. Uldis Rubins, BSc student Laura Dambite

Report on the methodology and test measurement results

Tissue phantoms

One-layered agar-based optical phantoms were made of Agar (powder, 05040, Sigma-Aldrich), Intralipid (emulsion 20%, I141, Sigma-Aldrich), Hemoglobin (water soluble, 198285, Sigma-Aldrich), Nigrosin (water soluble, Sigma-Aldrich). Intralipid (IL) was used for scattering simulation, nigrosine (Ni) and hemoglobin (Hb) – for absorption simulation. Agar hydrogel was prepared by mixing agar powder with tap water and by heating the solvent. Concentrations of components are listed in the table 2-1. The substances were filled in cylindrical plastic forms with a diameter of ~6 cm and a height of ~3 cm. Examples of the tissue phantoms are shown in the fig.2-1.

Table 2-1. Concentrations of the phantom components (IL – intralipid, Hb – hemoglobin, Ni – nigrozin).

Phantom composition	**Concentration**				
	C_{IL}	**C_{Hb}**		**C_{Ni}**	
	%	***%***	***μM***	***%***	***μM***
Agar, IL	0.5	-	-	-	-
	1.5	-	-	-	-
Agar, Hb	-	1	3	-	-
	-	2	6	-	-
	-	3	9	-	-
Agar, Hb, IL	1	1	6	-	-
Agar, Ni	-	-	-	0.05	24.5
	-	-	-	0.1	49

(a) (b) (c) (d) (e)

Fig.2-1. Examples skin optical phantoms: a) C_{IL}=1%, b) C_{Hb}=1%, c) C_{Hb}=3%, d) C_{Ni}=0.05%, e) C_{Ni}=0.1%.

Picosecond kinetic measurements

The time-correlated single photon counting method was used for optical pulse shape measurements. A broadband picosecond laser (*Whitelaser micro supercontinuum lasers, Fianium, NKT PHOTONICS, DK*, 400-2000 nm, pulse full width at half maximum 6 ps, repetition rate 20 MHz) was used as initial light source. Time resolution of the system was 9.7 ps which ensured minimum detectable photon path length ~2 mm. Specific narrow spectral bands were selected by couples of identical interference filters. One of them was filtering the input light while the other was placed in front of the photo-detector (photomultiplier HPM-100-07 combined with the detector controller DCC-100 and data processing card SPC-150, all *Becker&Hickl GmbH*, DE). Our measured FWHM values of IRFs at all exploited wavelengths were in-between 50+/-2 ps, indicating that temporal response of the photodetector determined the measured shapes of both input and output pulses. The examined spectral range was 480-800 nm; the spectral bands were centered at 480 nm, 520 nm, 560 nm, 600nm, 680 nm, 720 nm, 760 nm snd 800 nm. using 10 nm half-

bandwidth interference filters (*Andover Corporation, USA* - part numbers 480FS10-12,5; 520FS10-12,5; 560FS10-12,5; 600FS10-12,5; 680FS10-12,5; 720FS10-12,5; 760FS10-12,5; 800FS10-12,5).

Stable recording of optical signals via the input and output fibers (WF-400, *Light Guide Optics International*, LV, silica core diameter 200 microns, length 1,05 m) was ensured by means of a custom-made fiber holding probe with inter-fiber distances 1 mm, 8 mm, 12 mm, 16 mm and 20 mm. To provide equal pressure on the phantom/skin surface at all measurements, the probe was designed as a lift where the inside sliding part with the couple of fibers lied on the surface, providing a pressure determined by its weight ~ 35 g/cm^2. The outside part of the probe was fixed on phantom/skin during the measurements.

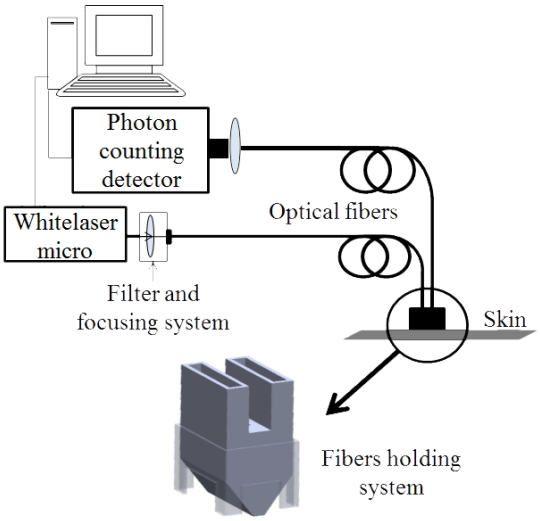

Fig. 2-2. The measurement set-up scheme.

Processing of the measured data involved comparing the shapes of the phantom/skin input and output pulses - *a(t)* and *b(t)*, respectively. The temporal distribution function *f(t*) of photon arrivals following infinitely narrow δ-pulse input were found by de-convolution of the integral

$$b(t) = \int_0^t a(t-\tau)f(\tau)d\tau \qquad (1).$$

This inverse problem was solved using a built-in deconvolution algorithm of *Matlab*. As the de-convolved function was more noisy than *b(t)*, original scripts were developed for data smoothing using the *Log-normal* function, as well as for semi-automatic calculations of the temporal distribution functions and the mean arrival times of skin-scattered photons. In particular, the output signal *b(t)* was fitted by *Log-normal* distribution function using non-linear fitting Matlab *lsqcurvefit* algorithm. This function was selected due to its similarity to the measured data. Next, the input pulse was shifted in time towards output pulse until the rising fronts of pulses coincided at the 5% level. The path length of the first detected photons was obtained as: *Min path length = dt · c/n* , where *dt* is the time shift towards output pulse. Then the inverse problem (1) was solved using a built-in Matlab deconvolution algorithm *deconv* and *f(t)* was calculated. Finally, the mean arrival time of skin-scattered photons was calculated as the time moment when the area under curve *f(t)* equals from left and right side. After restoring *f(t),* the corresponding distribution of back-scattered photon path lengths in skin was calculated as

$$\phi(s) = f(t) \cdot c/n \qquad (2),$$

where *c* is the speed of light in vacuum and *n* is the mean refraction index of superficial skin tissues (n ~ 1.4). The photon mean path lengths (PMPL) in phantom/skin were found as the mean values of integrated path length distribution functions. Eventual error due to different slopes of both rising fronts (after the time-shifting) did not exceed 2 mm.

Measurements were taken from the following phantoms:

- Agar 4.2 g
- Intralipid 0,5% and 1,5%
- Nigrozin 0,05% and 0.1%
- Hemoglobin 1%, 2% and 3%

Mean values averaged over 9 measurements from each phantom (with standard deviation) are presented.

Along with skin phantoms, also ***in-vivo* skin measurements** were performed in order to validate the phantom data. Ten volunteers with skin photo-type II or III (Fitzpatrick classification), aged between 25 and 68, were examined with their written consent under permission of the local Ethics Committee. The measurements were taken from healthy skin of the forearm, avoiding contact with large superficial blood vessels. The average spectral power density on skin was ~ 10 mW/cm^2, i.e. well below the skin laser safety limit (200 mW/cm^2). Besides, measurement series of several skin malformations were taken [3].

Results

The main results of PMPL measurements in phantoms are presented in figures 2-3 – 2-6.

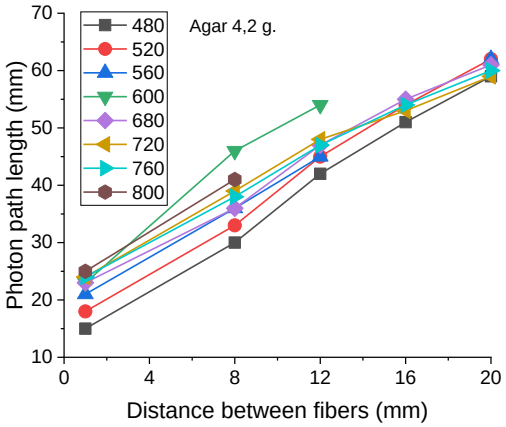

Fig.2-3. The mean photon path lengths in pure Agar 4.2 g (base of all phantoms).

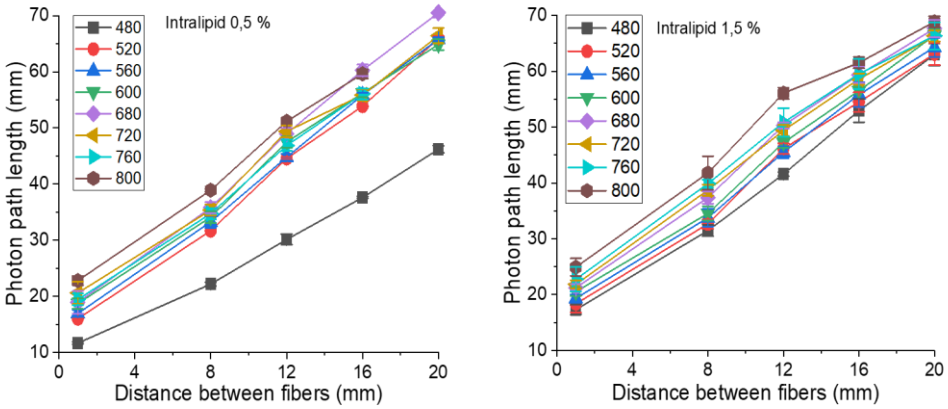

Fig.2-4. The mean photon path lengths in phantoms with Intralipid at concentrations 0,5% and 1,5%.

Generally, all PMPL values increased with growing distance between the input and output fibers and with growing wavelengths, as initially expected. Various additives to the Agar matrix induced changes in the PMLP values. In particular, adding of Intralipid promoted photon scattering which resulted in increased PMPL. The PMPL-distance relations at various wavelengths lied close to each other, with exception of 480 nm at smaller (0.5%) concentration – this phenomenon needs further studies to be explained. Adding of nigrozin, in opposite, reduced the PMPL values which obviously was caused by stronger absorption at all wavelengths. Unexpectedly, at smaller concentration of nigrozin (0.05%) the remitted photon path lengths appeared notably shorter that at twice higher concentration (0.1%); again, this needs more studies to be explained. Somewhat similar trend was observed in hemoglobin phantoms where PMPL values at 2%

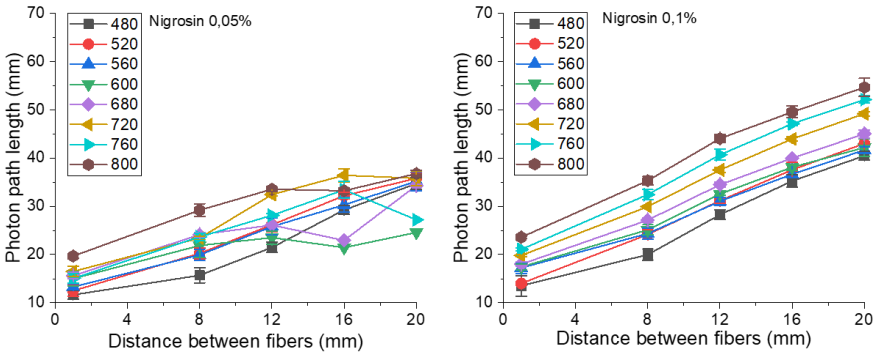

Fig.2-5. Photon mean path length in phantoms containing nigrozin at concentrations 0,05 % and 0.1 %.

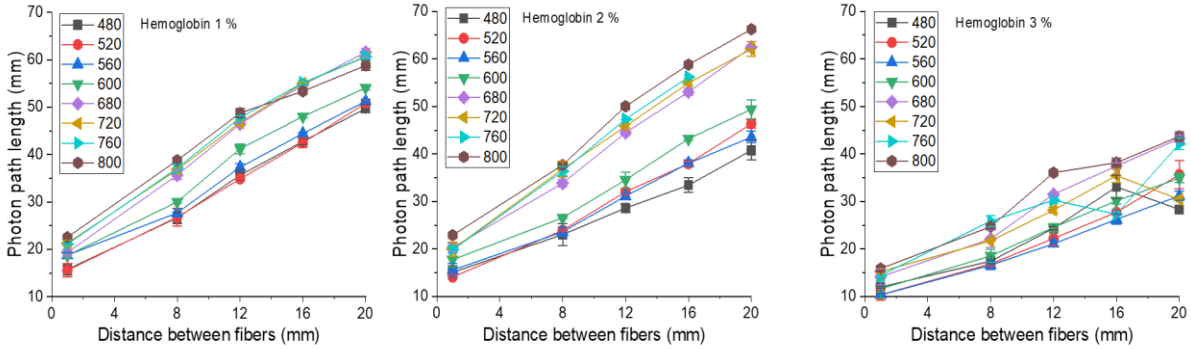

Fig.2-6. Photon mean path length in phantoms containing hemoglobin at concentrations 1%. 2% and 3%. concentration for some wavelengths were higher than those at 1% concentration. However, at 3% of hemoglobin the PMPL values decreased approximately twice so confirming increased role of absorption.

Also ***in-vivo*** **skin measurements** resulted in some unexpected data, especially concerning the numerical values of the mean path lengths of skin-remitted photons which appeared notably higher than those calculated in frame of the Monte-Carlo model. Fig.2-7 illustrates the measured shapes of input laser pulse (IRF) and the skin-remitted pulses at two wavelength bands and several inter-fiber distances. The signal-to-noise ratio considerably decreased at shorter wavelengths (560 nm, 600 nm) and at longer distances between fibers (16 mm, 20 mm); these spectral-spatial combinations could be recorded only for two volunteers.

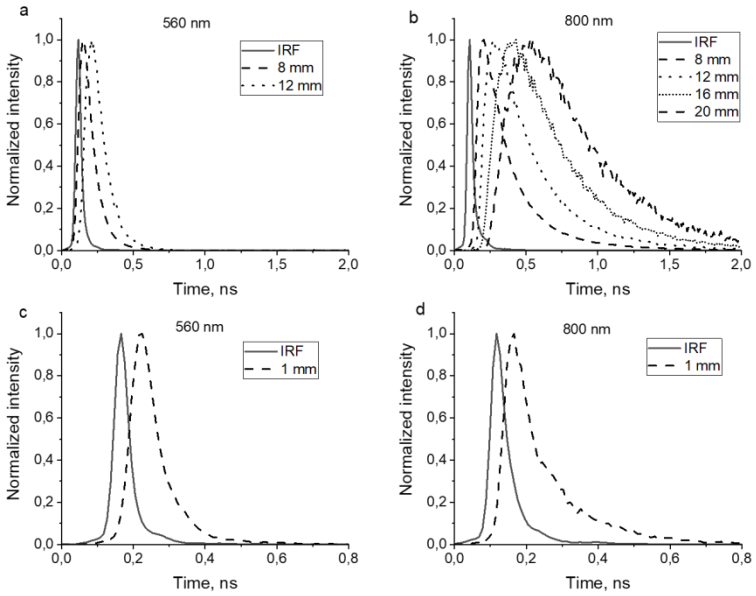

Fig.2-7. The 560 nm (a, c) and 800 nm (b, d) input and output pulse shapes at various inter-fiber distances (single volunteer data).

Results of deconvolution (1) are illustrated on Fig.2-8 for the case of 760 nm wavelength band and two inter-fiber distances - 8 mm and 20 mm. As expected, the δ-response functions *f(t)* are bell-shaped, with some initial time delay that corresponds to travel time of the first detected skin-scattered photons. The obtained photon arrival time distributions were further used to calculate the related mean values of photon travel times and the corresponding mean photon path lengths (2) for all 35 spectral-spatial combinations; the results are summarized in Table 2-2. The initial time delay of *f(t)* converted into path lengths of the first detected photons varied depending on the wavelength and the inter-fiber distances; all spectral-spatial combinations are illustrated in Table 2-3.

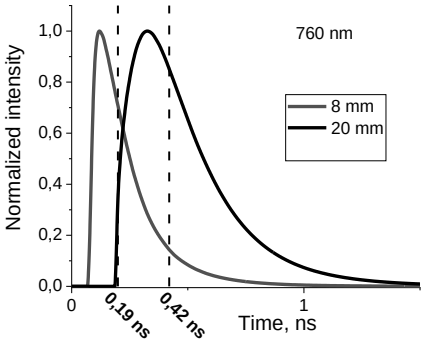

Fig.2-8. The smoothed skin-remitted photon arrival time distributions *f(t)* and their mean values for the 760 nm band at two inter-fiber distances (a single volunteer).

Dependences of the photon mean path length on the distance between fibers at all exploited wavelength bands are presented on Fig.2-9. The differences are significant for the 560 nm, 600 nm and 640 nm bands (a), whereas in the spectral range 680-800 nm the photon mean path lengths appear to be similar within the error ranges (b). As for the 560 nm spectral band, only two volunteers measurements were successful which explains the relatively small dispersion of data (signal-to-noise ratio was close to one and the measurement error could not be properly evaluated).

Table 2-2. The mean skin-remitted photon path lengths (in mm, with standard deviation) for all available spectral-spatial combinations. The upper raw represents inter-fiber distances.

Central wavelegth,nm	1 mm	8 mm	12 mm	16 mm	20 mm
560	16 ± 3	27 ± 3	41 ± 2	53 ± 5*	62 ± 1*
600	19 ± 3	37 ± 3	53 ± 4	68 ± 5	84 ± 8
640	21 ± 3	40 ± 3	59 ± 5	75 ± 4	94 ± 6
680	23 ± 4	41 ± 4	64 ± 6	86 ± 10	110 ± 16
720	22 ± 2	41 ± 4	63 ± 4	85 ± 8	106 ± 12
760	22 ± 2	41 ± 3	60 ± 3	78 ± 5	96 ± 5
800	26 ± 3	42 ± 3	63 ± 4	84 ± 8	105 ± 10

*) data of a single volunteer

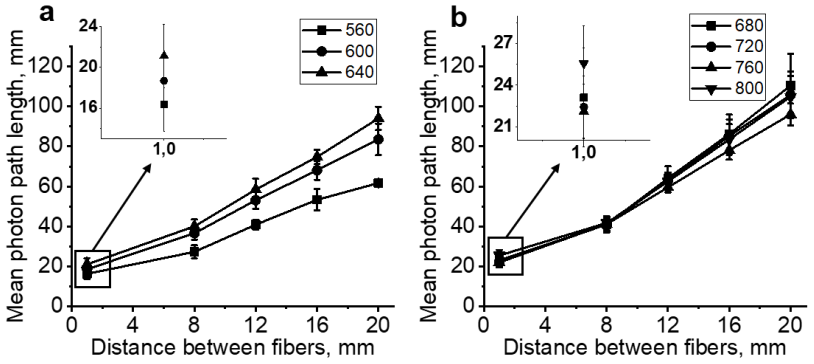

Fig.2-9. The remitted photon mean path length as function of distance between the input and output fibers.

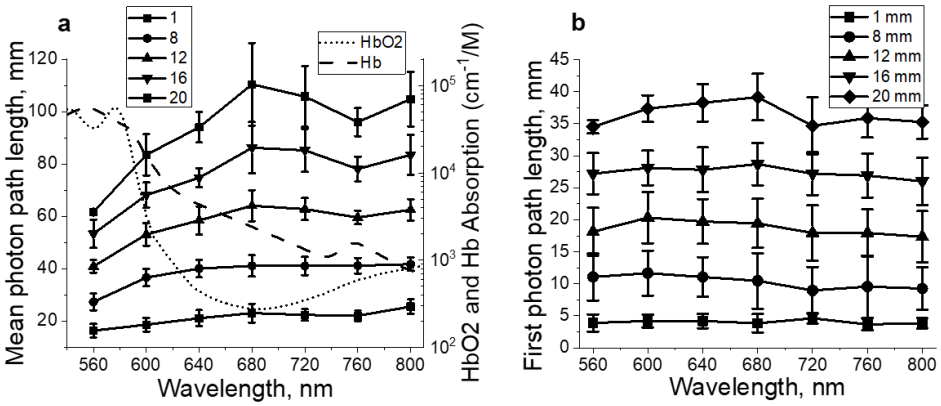

Fig. 2-10. a - spectral dependencies of the mean pathlength of skin-remitted photons at various interfiber distances, b – spectral dependencies of the path lengths calculated for the first detected photons. The dotted curves represent oxy- and deoxy-hemoglobin absorption.

Table 2-3. The shortest path lengths in skin of the first detected photons (in mm).

Inter-fiber distance (mm) / central wavelength, nm	560	600	640	680	720	760	800
1	7 ± 3	5 ± 2	7 ± 3	8 ± 4	8 ± 4	7 ± 4	7 ± 4
8	15 ± 13	23 ± 17	26 ± 21	27 ± 24	24 ± 20	23 ± 19	22 ± 18
12	24 ± 15	35 ± 24	40 ± 32	40 ± 30	37 ± 30	36 ± 28	35 ± 28
16	30 ± 18	44 ± 28	52 ± 38	49 ± 37	48 ± 36	47 ± 34	48 ± 35
20	24 ± 17	55 ± 34	62 ± 43	67 ± 47	61 ± 44	58 ± 39	59 ± 42

Table 2-4. Linear correlation coefficients R^2 and slope coefficients k for data illustrated in Fig.2-9.

Wavelength, nm	R^2	k
560	0,98	2,39
600	0,99	3,41
640	0,99	3,84
680	0,97	4,60
720	0,98	4,39
760	0,99	3,89
800	0,97	4,17

As follows from Fig.2-9, the photon mean path length dependencies on inter-fiber distance at all examined wavelength bands appear to be nearly linear, with the corresponding Pearson correlation coefficients in the range 0.97…0.99 (Table A2-4). However, it is not the case for the spectral dependencies (Fig.2-10,a) - at all inter-fiber distances (except for 1 mm) a pronounced maximum around 680-720 nm exhibits, with a following dip at 760 nm. Spectral dependences of the path lengths completed by the first detected photons (Fig. 2-10,b and Table 2-3) show a similar trend. Correlation with absorption spectrum of the dermal hemoglobin (marked by the dotted curves) can explain this non-linearity.

Publicity of the A1.2 results

Conference reports:

- ***European Conferences on Biomedical Optics***, June 2019, Munich: **V.Lukinsone** (oral), "Towards direct measurements of remitted photon path lengths in skin: kinetic studies in the range 520-800 nm"
- ***Advanced Laser Technologies, ALT-2019,*** September 2019, Praha: **J.Spigulis** (invited, oral), "Lasers for skin diagnostics - chromophore mapping and photon pathlength estimation"
- ***SPIE Photonics Europe***, March 2020, Strasbourg; **V.Lukinsone** (remote, audio-presentation), "Remitted photon path length in human skin, skin phantoms and cell cultures"
- ***OSA-Biomed***, April 2020, Ft.Lauderdale: **J.Spigulis** (remote, poster with audio-presentation), "Skin-remitted photon path lengths: experimental study".
- ***Biophotonics – Riga 2020,*** August 2020, Riga; **J.Spigulis** (remote): "Biophotonics research in Riga: recent projects and results".
- ***Saratov Fall Meeting***, September 2020, Saratov; **J.Spigulis** (invited, remote): "Skin reflectance: how long the photons travel until remission".

Published papers:

1. V.Lukinsone, A.Maslobojeva, U.Rubins, M.Kuzminskis, M.Osis, J.Spigulis, "Remitted photon path lengths in human skin: *in-vivo* measurement data", *Biomed.Opt.Expr*. **11**(5), 2866-2873 (2020). https://doi.org/10.1364/BOE.388349.
2. V. Lukinsone, I. Kuzmina, M. Tamosiunas, A. Maslobojeva, M. Kuzminskis, U. Rubins, J. Spigulis, "Remitted photon path length in human skin, skin phantoms and cell cultures," *Proc. SPIE* **11363**, 1136320 (2020); doi: 10.1117/12.2555822.
3. J. Spigulis, V. Lukinsone, U. Rubins, A. Maslobojeva, M. Kuzminskis, "Skin-remitted photon path lengths: experimental study," in *Biophotonics Congress: Biomedical Optics 2020*, *OSA Technical Digest*, JW3A.1 (2020). https://www.osapublishing.org/abstract.cfm?uri=translational-2020-JW3A.1&Site=osac.
4. J.Spigulis, I.Kuzmina, I.Lihacova, V.Lukinsone, B.Cugmas, A.Grabovskis, E.Kviesis-Kipge, A.Lihachev, "Biophotonics research in Riga: recent projects and results", *Proc.SPIE* **11585,** 1158502 (2020).
5. V. Lukinsone, M. Osis, J. Latvels, I. Kuzmina, U. Rubins, N. Zorina, A. Maslobojeva, J. Spigulis, "Towards direct measurements of remitted photon path lengths in skin: kinetic studies in the range 520-800 nm," *Proc. SPIE* **11075**, 1107505 (2019); doi: 10.1117/12.2526663.

A1.3. *Elaboration of algorithms for mapping of particular skin chromophores and chromophore concentration calculation*

August 2019 – April 2020

The main contributors: PhD student Ilze Oshina, Dr.phys. Uldis Rubins

Skin chromophore mapping algorithms developed in previous projects for chromophore mapping by smartphones are supplemented with information about the remitted photon path length distributions, light loss due to absorption of other chromophores, epidermis thickness and light penetration depth in the skin. Here the improved algorithms for melanin, oxyhemoglobin and deoxyhemoglobin concentration calculation from images taken with laser device and LED device are described. The superscripted numbers in Fig.3-1 are specified below.

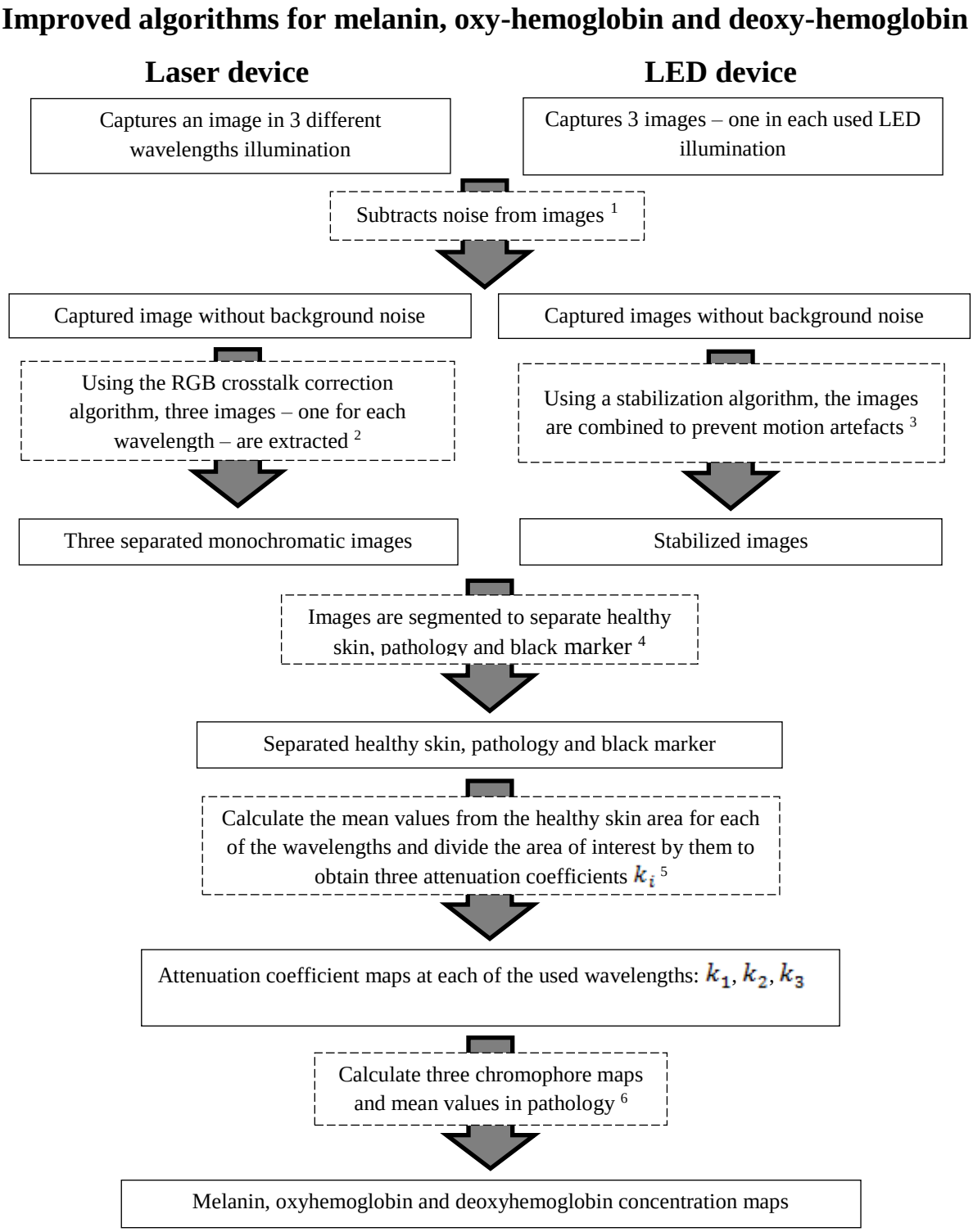

Fig. 3-1. The chromophore-mapping algorithm scheme.

1. Subtracts noise from images

	Laser device	LED device		
With noise	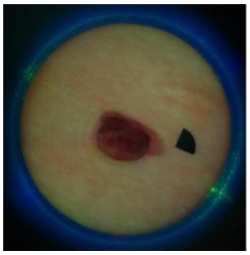		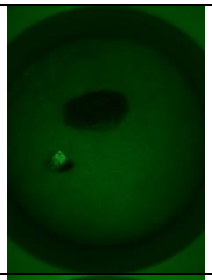	
Without noise	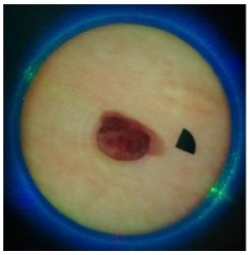		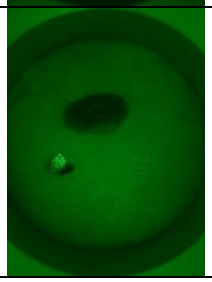	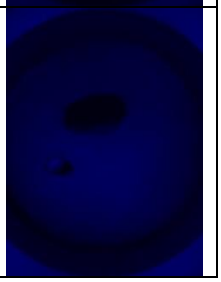

2. Using the RGB crosstalk correction algorithm, three images – one for each wavelength – are extracted in laser device case [1]

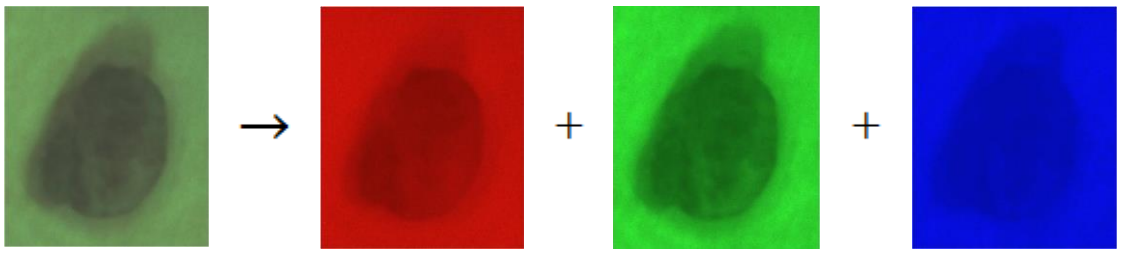

3. Using a stabilization algorithm and black marker, the images are combined to prevent motion artefacts in LED device case. The adjustment is made using the green LED image as the basis, as this is the second of the three captured images. A black marker is used for stabilization.

Green LED	Red LED	Stabilized red LED
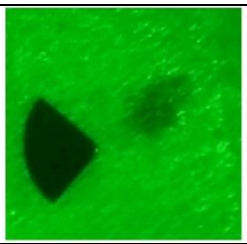	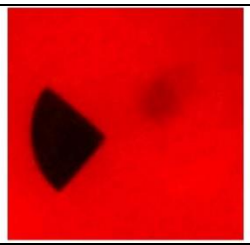	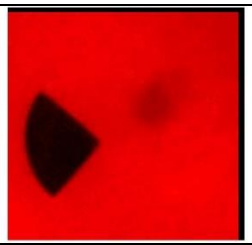
Green LED	**Blue LED**	**Stabilized blue LED**
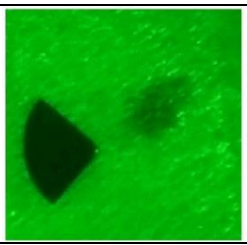	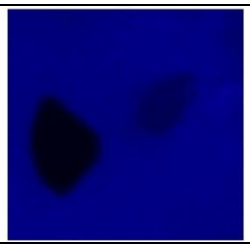	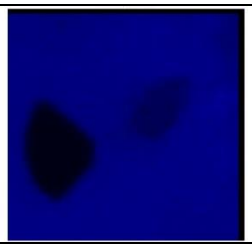

4. Images are segmented to separate healthy skin, pathology and black marker for LED device case, and healthy skin and pathology for laser device case. The green image is used for segmentation.

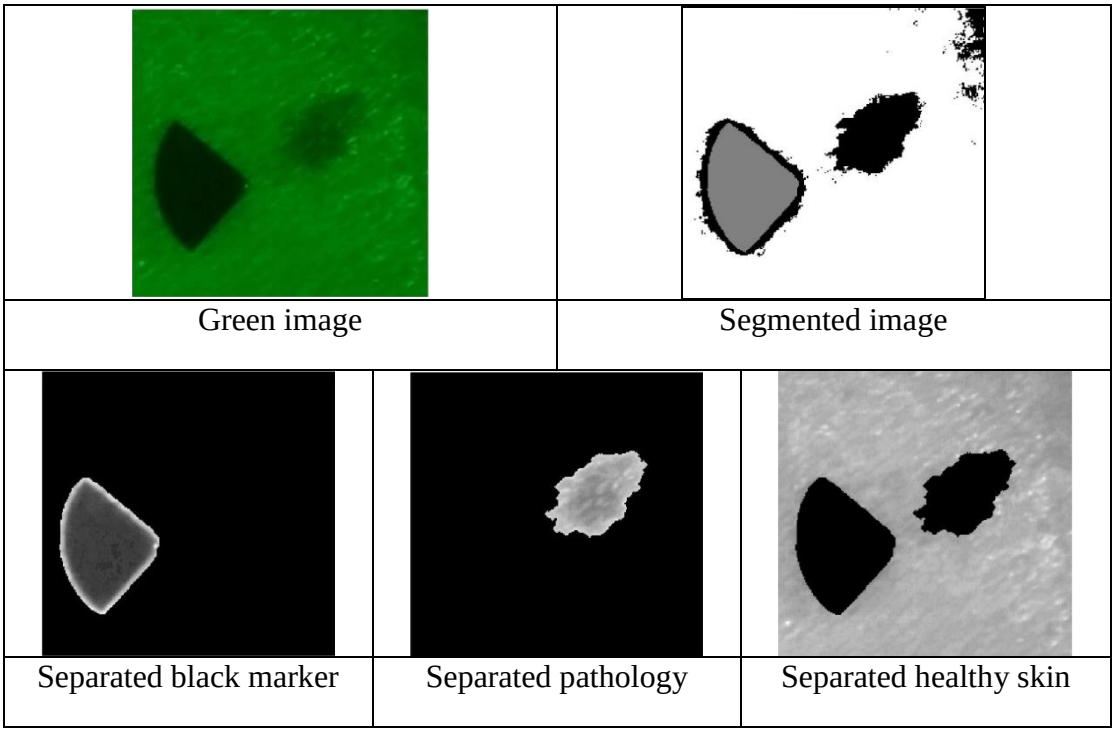

5. Calculate the mean values from the healthy skin area for each of the wavelengths and divide the area of interest by them to obtain three attenuation coefficients k_i.

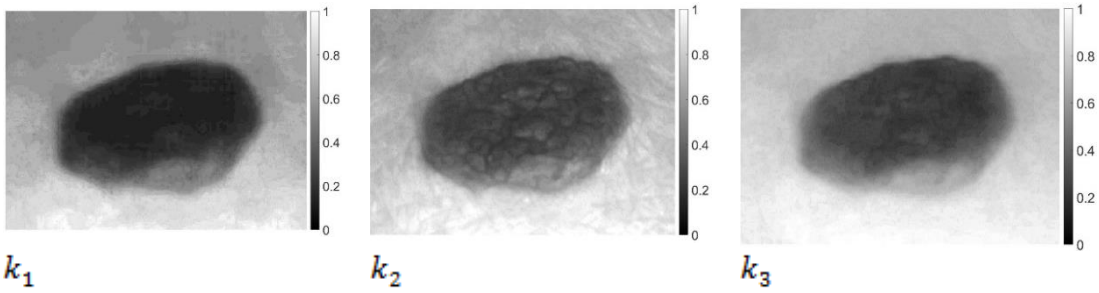

6. Calculate three chromophore distribution maps and the mean concentration values in the pathology. Healthy skin is used as a reference. Skin optical properties are approximately the same in all regions of interest. Scattering coefficient is assumed to be the same in the healthy skin and in the pathology. Scattering is taken into account when photon mean path length in the skin is calculated.

Beer-Lambert-Bouguer law adapted for skin reflectance is used:

$$I = I_0 e^{-\mu_a \cdot l} \qquad (1),$$

where μ_a – absorption coefficient, I – intensity of diffused reflected light from the skin pathology, I_0 – intensity of diffused reflected light from the healthy skin, l – photon mean path length in the skin. This can be expressed for the three exploited wavelengths and the three considered chromophores (melanin, oxy-hemoglobin, deoxy-hemoglobin) as follows:

$$\begin{cases} c_{\text{Mel}} \cdot \varepsilon_{\text{Mel}}(\lambda_1) \cdot \mathrm{d}_1 + (c_{\text{Ox}} \cdot \varepsilon_{\text{Ox}}(\lambda_1) + c_{\text{Deox}} \cdot \varepsilon_{\text{Deox}}(\lambda_1)) \cdot (1 - \mathrm{d}_1) + z_1 = \dfrac{ln\frac{I_0(\lambda_1)}{I(\lambda_1)}}{2{,}303 \cdot l(\lambda_1)} \\ c_{\text{Mel}} \cdot \varepsilon_{\text{Mel}}(\lambda_2) \cdot \mathrm{d}_2 + (c_{\text{Ox}} \cdot \varepsilon_{\text{Ox}}(\lambda_2) + c_{\text{Deox}} \cdot \varepsilon_{\text{Deox}}(\lambda_2)) \cdot (1 - \mathrm{d}_2) + z_2 = \dfrac{ln\frac{I_0(\lambda_2)}{I(\lambda_2)}}{2{,}303 \cdot l(\lambda_2)} \\ c_{\text{Mel}} \cdot \varepsilon_{\text{Mel}}(\lambda_3) \cdot \mathrm{d}_3 + (c_{\text{Ox}} \cdot \varepsilon_{\text{Ox}}(\lambda_3) + c_{\text{Deox}} \cdot \varepsilon_{\text{Deox}}(\lambda_3)) \cdot (1 - \mathrm{d}_3) + z_3 = \dfrac{ln\frac{I_0(\lambda_3)}{I(\lambda_3)}}{2{,}303 \cdot l(\lambda_3)} \end{cases}$$

$z_i = 0{,}01 \cdot (1 - k_i)$, $k_i = \frac{I_i}{I_{0_i}}$,

Mel – melanin, Oks – oxyhemoglobin, $Deoks$ – deoxyhemoglobin,

ε – extinction coefficient, c – chromophore concentration, $\mathrm{k_i}$ – attenuation coefficient,

$\mathrm{d_i}$ – part of the light that is absorbed in the epidermis at the wavelength λ_i,

$\mathrm{z_i}$ – loss coefficient – describes the part of the light absorbed by other chromophores.

Assume that: $A_1 = \frac{ln\frac{I_0(\lambda_1)}{I(\lambda_1)}}{2{,}303 \cdot l(\lambda_1)}$, $A_2 = \frac{ln\frac{I_0(\lambda_2)}{I(\lambda_2)}}{2{,}303 \cdot l(\lambda_2)}$, $A_3 = \frac{ln\frac{I_0(\lambda_3)}{I(\lambda_3)}}{2{,}303 \cdot l(\lambda_3)}$

$\varepsilon_{11} = \varepsilon_{\text{Mel}}(\lambda_1)$, $\varepsilon_{12} = \varepsilon_{\text{Ox}}(\lambda_1)$, $\varepsilon_{13} = \varepsilon_{\text{Deox}}(\lambda_1)$

$\varepsilon_{21} = \varepsilon_{\text{Mel}}(\lambda_2)$, $\varepsilon_{22} = \varepsilon_{\text{Ox}}(\lambda_2)$, $\varepsilon_{23} = \varepsilon_{\text{Deox}}(\lambda_2)$

$\varepsilon_{31} = \varepsilon_{\text{Mel}}(\lambda_3)$, $\varepsilon_{32} = \varepsilon_{\text{Ox}}(\lambda_3)$, $\varepsilon_{33} = \varepsilon_{\text{Deox}}(\lambda_3)$

Melanin concentration:

$$c_{Mel} = \frac{B_1}{B_2}$$

$$B_1 = (1 - \mathrm{d}_1)(1 - \mathrm{d}_3)(\varepsilon_{13}\varepsilon_{32} - \varepsilon_{12}\varepsilon_{33})\big((1 - \mathrm{d}_1)\varepsilon_{13}(-\mathrm{A}_2 + \mathrm{z}_2) - (1 - \mathrm{d}_2)\varepsilon_{23}(-\mathrm{A}_1 + \mathrm{z}_1)\big) - (1 - \mathrm{d}_1)(1 - \mathrm{d}_2)(\varepsilon_{13}\varepsilon_{22} - \varepsilon_{12}\varepsilon_{23})((1 - \mathrm{d}_1)\varepsilon_{13}(-\mathrm{A}_3 + \mathrm{z}_3) - (1 - \mathrm{d}_3)\varepsilon_{33}(-\mathrm{A}_1 + \mathrm{z}_1))$$

$$B_2 = (1 - \mathrm{d}_1)(1 - \mathrm{d}_2)(\varepsilon_{13}\varepsilon_{22} - \varepsilon_{12}\varepsilon_{23})\big((1 - \mathrm{d}_1)\mathrm{c}_3\varepsilon_{13}\varepsilon_{31} - \mathrm{d}_1(1 - \mathrm{d}_3)\varepsilon_{11}\varepsilon_{33}\big) - \big((1 - \mathrm{d}_1)\mathrm{d}_2\varepsilon_{13}\varepsilon_{21} - \mathrm{d}_1(1 - \mathrm{d}_2)\varepsilon_{11}\varepsilon_{23}\big)\big((1 - \mathrm{d}_1)(1 - \mathrm{d}_3)(\varepsilon_{13}\varepsilon_{32} - \varepsilon_{12}\varepsilon_{33})\big)$$

Oxyhemoglobin concentration:

$$c_{Ox} = \frac{B_3}{B_4}$$

$$B_3 = (\mathrm{A}_1 - \mathrm{z}_1)(\mathrm{d}_2(1 - \mathrm{d}_3)\varepsilon_{21}\varepsilon_{33} - (1 - \mathrm{d}_2)\mathrm{d}_3\varepsilon_{23}\varepsilon_{31}) + (\mathrm{A}_2 - \mathrm{z}_2)((1 - \mathrm{d}_1)\mathrm{c}_3\varepsilon_{13}\varepsilon_{31} - \mathrm{d}_1(1 - \mathrm{d}_3)\varepsilon_{11}\varepsilon_{33}) + (\mathrm{A}_3 - \mathrm{z}_3)(\mathrm{d}_1(1 - \mathrm{d}_2)\varepsilon_{11}\varepsilon_{23} - (1 - \mathrm{d}_1)\mathrm{d}_2\varepsilon_{13}\varepsilon_{21})$$

$$B_4 = (1 - \mathrm{d}_1)\,(1 - \mathrm{d}_2)\mathrm{d}_3\varepsilon_{31}(\varepsilon_{13}\varepsilon_{22} - \varepsilon_{12}\varepsilon_{23}) + (1 - \mathrm{d}_1)\mathrm{d}_2(1 - \mathrm{d}_3)\varepsilon_{21}(\varepsilon_{12}\varepsilon_{33} - \varepsilon_{13}\varepsilon_{32}) + \mathrm{d}_1(1 - \mathrm{d}_2)(1 - \mathrm{d}_3)\varepsilon_{11}(\varepsilon_{23}\varepsilon_{32} - \varepsilon_{22}\varepsilon_{33})$$

Deoxyhemoglobin concentration:

$$c_{Deox} = \frac{B_5}{B_4}$$

$$B_5 = (\mathrm{A}_1 - \mathrm{z}_1)\big((1 - \mathrm{d}_2)\mathrm{d}_3\varepsilon_{22}\varepsilon_{31} - \mathrm{d}_2(1 - \mathrm{d}_3)\varepsilon_{21}\varepsilon_{32}\big) + (\mathrm{A}_2 - \mathrm{z}_2)(\mathrm{d}_1(1 - \mathrm{d}_3)\varepsilon_{11}\varepsilon_{32} - (1 - \mathrm{d}_1)\mathrm{d}_3\varepsilon_{12}\varepsilon_{31}) + (\mathrm{A}_3 - \mathrm{z}_3)\big((1 - \mathrm{d}_1)\mathrm{d}_2\varepsilon_{12}\varepsilon_{21} - \mathrm{d}_1(1 - \mathrm{d}_2)\varepsilon_{11}\varepsilon_{22}\big)$$

$$B_4 = (1 - \mathrm{d}_1)\,(1 - \mathrm{d}_2)\mathrm{d}_3\varepsilon_{31}(\varepsilon_{13}\varepsilon_{22} - \varepsilon_{12}\varepsilon_{23}) + (1 - \mathrm{d}_1)\mathrm{d}_2(1 - \mathrm{d}_3)\varepsilon_{21}(\varepsilon_{12}\varepsilon_{33} - \varepsilon_{13}\varepsilon_{32}) + \mathrm{d}_1(1 - \mathrm{d}_2)(1 - \mathrm{d}_3)\varepsilon_{11}(\varepsilon_{23}\varepsilon_{32} - \varepsilon_{22}\varepsilon_{33})$$

Validation of the algorithm - spectral images and the related chromophore maps:

White light	663 nm	535 nm	460 nm
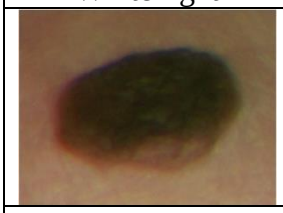	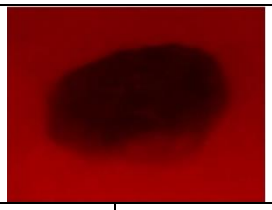	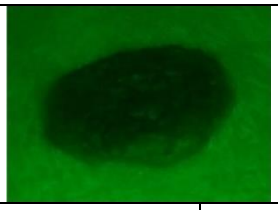	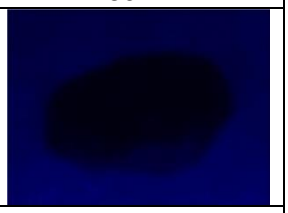
Melanin concentration increase, mM	Oxyhemoglobin concentration decrease, mM	Deoxyhemoglobin concentration increase, mM	
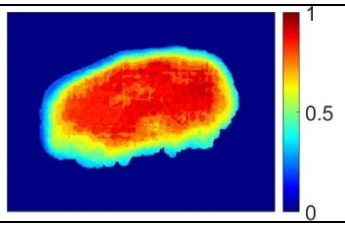	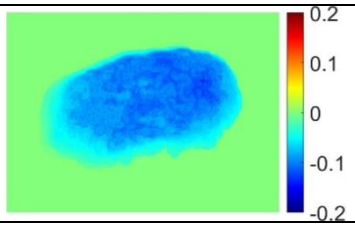	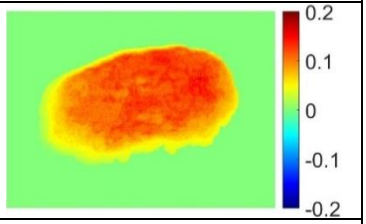	
$\overline{c_{Mel}} = 0{,}68\ mM$	$\overline{c_{Ox}} = -0{,}08\ mM$	$\overline{c_{Deox}} = 0{,}09\ mM$	

Reference:

[1] J.Spigulis, L.Elste. *Single-snapshot RGB multispectral imaging at fixed wavelengths: proof of concept*, Proc.SPIE, 8937, 89370L (2014)

A1.4. *Clinical validation of the updated imaging technology: volunteer measurements*

November 2019 – October 2020

The main contributors: Res.assist. Anna Berzina, Dr.phys. Ilona Kuzmina, Dr.phys. Vanesa Lukinsone, PhD student Ilze Oshina, res.assist. Anna Maslobojeva, lab.assist. Laura Dambite.

1. Statistics of the measured skin neoplasms

Clinical validation was performed in the Science Building of University of Latvia from January to October 2020; preparations started in November 2019. Overall, **164 volunteers** have been involved. Volunteers with skin photo-types I, II or III (Fitzpatrick classification), aged between 12 and 88, were examined with their written consent under permission of the local Ethics Committee. The images of **292 different skin neoplasms** have been captured and **photon-time-of-flight (PTOF)** signals have been measured on **94 of these neoplasms**. **Table 4-1** provides detailed description of measured skin neoplasms. The measurements were taken accordingly to the protocols described below.

The general procedure for measurements

1. A doctor explains to a patient the measurement procedure, an impact of the diagnostic device, as well as information in the patient consent form and patient rights.
2. The volunteer signs the patient consent form if he/she agrees to the procedure.
3. The doctor captures images of neoplasm(s) by a dermatoscope, puts markers near the neoplasm(s) that is (are) going to be captured with the devices and writes down the clinical diagnoses to each lesion.
4. RGB images are being captured by LED and Laser prototypes according to the measurement protocol (see below).

5. Picosecond kinetic measurements are being performed according to the measurement protocol (see below).

Table 4-1. Statistics of the measured skin neoplasms from January to October 2020

Diagnosis	Number		
	RGB+PTOF	RGB	Total
Benign	**92**	**194**	**286**
Junctional nevus	10	24	34
Combined nevus	25	59	84
Dermal nevus	28	50	78
Seborrheic keratosis	22	30	52
Hemangioma	4	24	28
Other	3	7	10
Malignant	**2**	**4**	**6**
Malignant melanoma	1	-	1
Basal Cell Carcinoma	1	2	3
Other	-	2	2
Total	**94**	**198**	**292**

2. Picosecond kinetic measurements

The time-correlated single photon counting method was used for optical pulse shape measurements; the equipment used was described in the A1.2 section (Fig.2-2).

***In-vivo* skin measurements** were taken from healthy skin and skin neoplasms, avoiding contact with large superficial blood vessels. The average spectral power density on skin was ~ 10 mW/cm^2, i.e. well below the skin laser safety limit (200 mW/cm^2). During clinical measurements, the spectral bands were centered at 520nm, 560nm, 680nm and 760nm by couples of identical interference filters; 480nm band was not exploited due to high tissue absorption.

The protocol for picosecond kinetic measurements

1. Measurements by PTOF system are taken as follows:
    a. Switch on the computer
    b. Open software SPCM (Becker&Hickl GmbH)
    c. Switch on White laser
    d. Locate probe on patient neoplasm or skin
    e. Measure neoplasm and clear skin next to it under illumination of following wavelengths 520, 560, 680, 760 nm
2. During the procedure, the patient is questioned if everything is all right and whether the patient feels comfortable.
3. After the measurement, the patient gets dressed, and, if patient has any additional questions, they are addressed accordingly.
4. The measurement is finished, the probe is being cleaned with a disinfectant wipe.

Results

Skin measurements were performed on different body locations. Due to high noise levels, the measurements at longer distances between fibres (16, 20 mm) and shorter wavelengths (520, 560 nm) failed. **Figure 4-1** shows the dependence of mean photon path length of skin on distance between fibres at wavelengths: 520nm, 560nm, 680nm and 760nm. The results were obtained from 104 volunteers aged from 20 to 86 years.

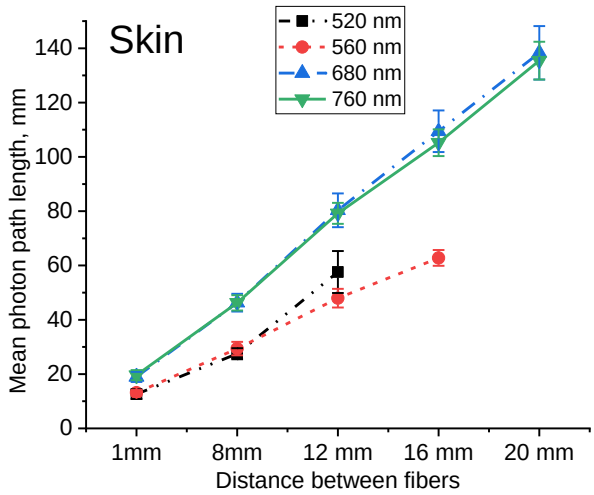

Fig.4-1. The averaged mean photon path lengths in healthy skin.

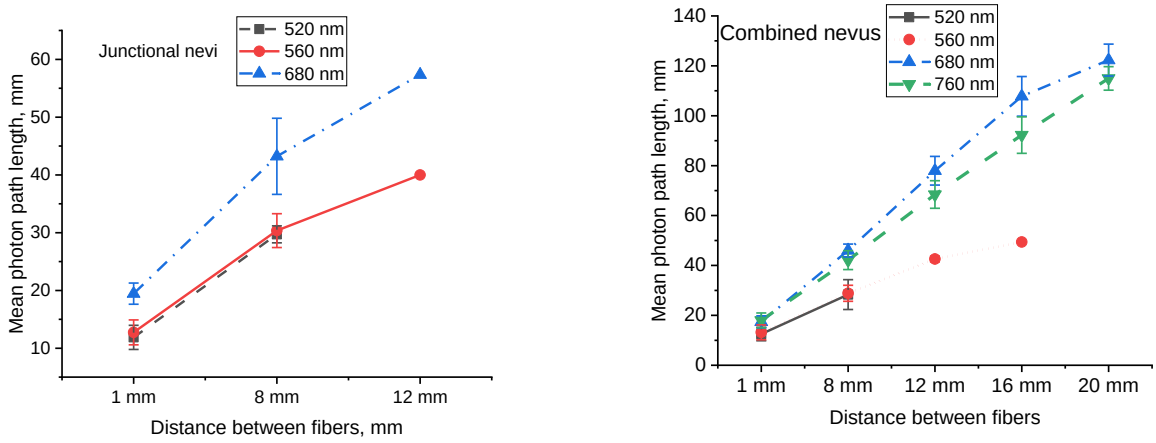

(a)

(b)

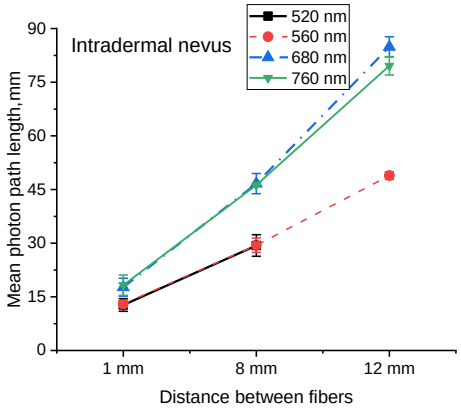

(c)

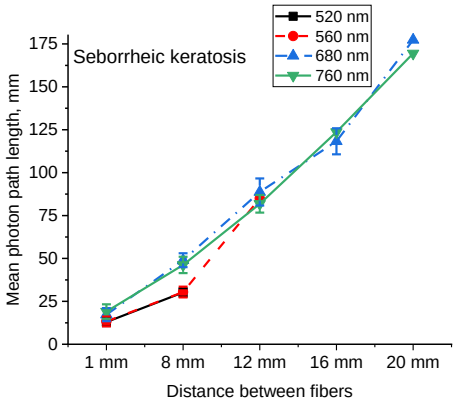

(d)

Fig.4-2. Dependences of the mean photon path length on the distance between fibres for seborrheic keratosis, dermal, combined, and junctional nevus at wavelengths of 520nm, 560nm, 680nm and 760nm.

Figure 4-2 shows the results for three types of nevi and seborrheic keratosis. The figure presents results of 12 junctional nevi (Fig.4-2(a)), 23 combined nevi (Fig.4-2(b)), 31 dermal (intradermal) nevi (Fig.4-2(c)) and 25 seborrheic keratosis (Fig.4-2(d)). It was difficult or impossible to measure the signals at shorter wavelength (520nm, 560nm) and longer distances between the fibres due to small size of some types of nevi (junctional and dermal) and low signal/noise ratio (observed in combined nevi and seborrheic keratosis). We assume that low signal-to-noise ratio was caused by high concentration of melanin in combined nevi and high level of keratinization in seborrheic keratosis.

Figure 4-3 presents the measured signals of 4 haemangiomas in two ways: (a) how mean photon path length is changing on different wavelengths, (b)how absorption of haemoglobin effects the mean photon path length. Although 24 haemangiomas were diagnosed among volunteers, only 4 haemangiomas were large enough to be measured.

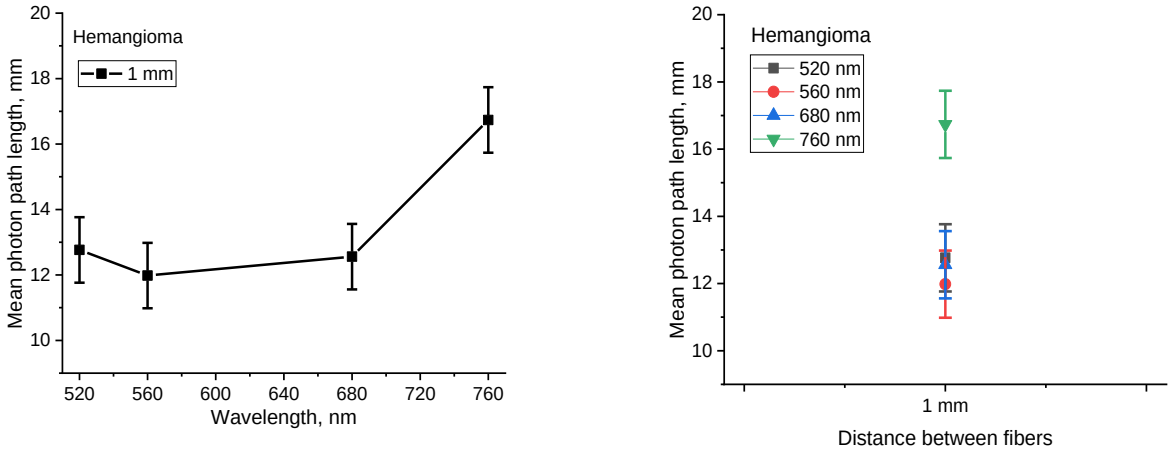

(a) (b)

Fig.4-3. The mean photon path length determined in a haemangioma.

3. RGB imaging

Smartphone devices and the measurement protocol

RGB images of neoplasms were captured by two smartphone devices: RGB LED illuminator (***LED prototype***) and triple-wavelength laser illuminator (***Laser prototype***) with *Nexus5* smartphones. **Fig. 4-4** shows outlooks of the prototypes. Two smartphone apps were used for image capturing: SkinViewer - by ***LED prototype*** and AZ Camera – by ***Laser prototype***. The settings of smartphone devices are listed in the Table 4-2**.**

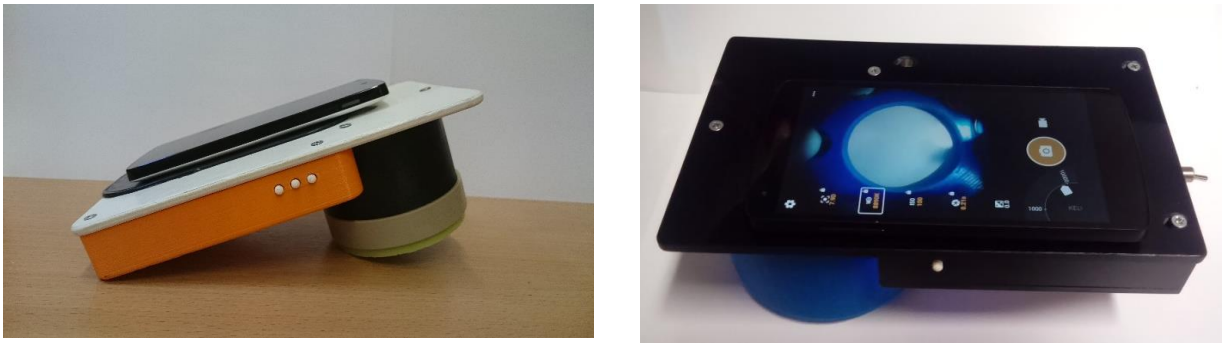

(a) (b)

Fig. 4-4. Smartphone devices used in validation measurements: (a) RGB LED illuminator (***LED prototype***), (b) triple-wavelength laser illuminator (***Laser prototype***)

Table 4-2. Settings of the smartphone devices.

Device	**Nexus5+RGB LED**	**Nexus5+Laser**
Smartphone App	***SkinViewer***	***AZ Camera***
White balance	-	~6000K
ISO	100	100
Wavelength (nm)		
R	663	659
G	535	532
B	460	448
Exposition time (s)		
t_R	0.02	0.87
t_G	0.02	0.87
t_B	0.02	0.87

The protocol for measurements by the LED and Laser prototypes

1. Measurements by ***LED prototype*** are taken as follows:
    - Switch on the device and the smartphone
    - Open the software *Skinviewer*
    - Switch on White LEDs
    - Locate the neoplasm and place the device in the best capture position.
    - Switch off white LEDs
    - Capture the neoplasm by *Skinviewer* under illumination at the following wavelengths: 460nm, 535nm, 663nm.
    - After images have been captured at all wavelengths for one lesion, the next neoplasm(s) are imaged.
2. Measurements by ***Laser prototype*** are taken as follows:
    - Switch on the device and the smartphone
    - Open the software *AZ Camera*
    - Switch on White LEDs
    - Locate the neoplasm and place the device in the best capture position.
    - Switch off white LEDs
    - Capture the neoplasm by *AZ Camera* under illumination at the following wavelengths: 448nm, 532nm, 659nm.
    - After images have been captured for one lesion, the next neoplasm(s) are imaged.
3. During the procedure, the patient is questioned if everything is all right and whether the patient feels comfortable.
4. After the measurement, the patient gets dressed, and, if patient has any additional questions, they are addressed accordingly.
5. The measurement is finished. The devices are being cleaned with a disinfectant wipe.

Results

Figure 4-6 shows examples of captured images of three types of nevi, seborrheic keratosis, and hemangioma. The figure illustrates dermatoscopic image of the neoplasm, images in red (R), green (G) and

blue (B) illumination captured by ***LED*** prototype and image captured under three wavelengths illumination by ***Laser*** prototype.

Mean values of chromophores' concentration were calculated from the area of each neoplasm using the algorithm described in the section A1.3. Two versions of this algorithm were analysed without correction coefficients (1v) and with correction coefficients (2v) related to absorption in the epidermis (d_i) and by other chromophores (z_i)

The photon mean path lengths used for concentration calculation from images of ***LED*** prototype are listed in the table 4-3. The mean pathlengths at 560nm and 680nm that were experimentally obtained at source-detector distance (between fibres) 1mm were used for green and red channel. The mean photon path length for blue channel was obtained using linear approximation of the experimental data such as shown the Fig.4-5. The equation of the linear approximation was used for the path length determination at wavelength of interest - 460nm (x – wavelength of interest, y – photon path length).

The photon mean path lengths used for concentration calculation from images of ***Laser*** prototype are listed in the table 4-4. The mean pathlengths for each channel were obtained from the linear approximation of the experimental data (obtained at source-detector distance 1mm) at laser wavelengths 448nm, 532nm, 659nm, as described above.

Figures 4-7, 4-8, 4-9, 4-10, and 4-11 illustrate chromophore and segmented chromophore maps of melanin, oxy- and deoxy-haemoglobin obtained from images of ***LED*** and ***Laser*** prototypes for each type of neoplasm.

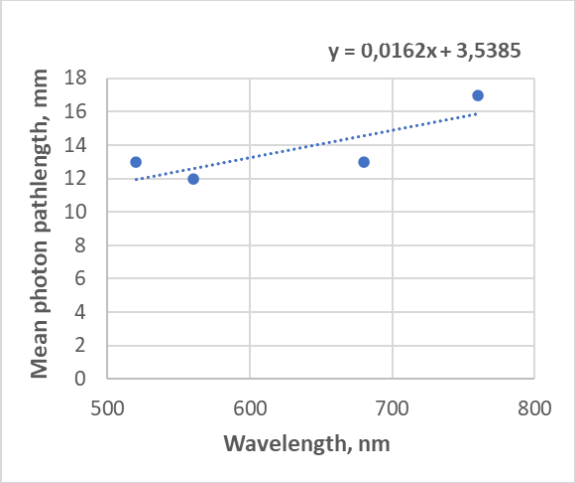

Fig. 4-5. An example of linear approximation of the experimentally obtained mean photon path length.

Table 4-3. Mean photon path lengths used for concentration calculations (***LED*** prototype).

RGB channel	**Mean photon path length, cm**				
	Hemangioma	Junctional nevus	Combined nevus	Dermal nevus	Seborrheic keratosis
Blue	1,1	0,9	1,1	1,1	1,1
Green	1,2	1,3	1,3	1,3	1,3
Red	1,3	1,9	1,7	1,8	1,7

Table 4-4. Mean photon path lengths used for concentration calculations (***Laser*** prototype).

RGB channel	**Mean photon path length, cm**				
	Hemangioma	Junctional nevus	Combined nevus	Dermal nevus	Seborrheic keratosis
Blue	1,1	0,8	1,1	1,1	1,1
Green	1,2	1,2	1,3	1,3	1,3
Red	1,4	1,8	1,6	1,6	1,6

Junctional nevus

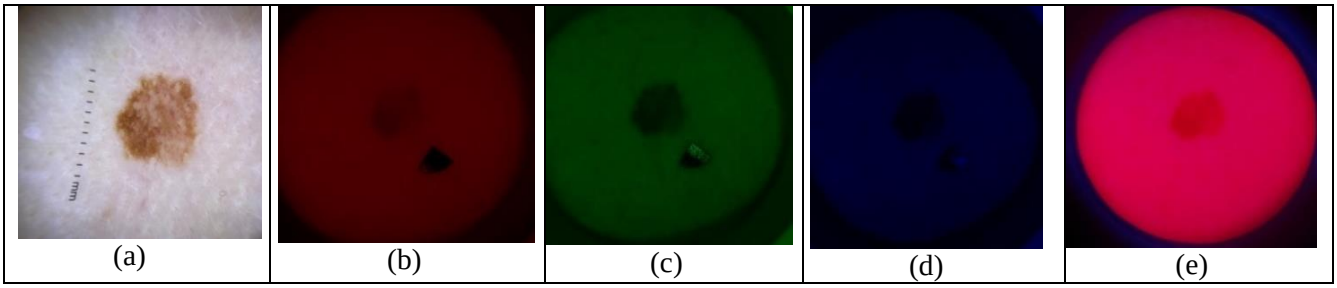

(a) (b) (c) (d) (e)

Combined nevus

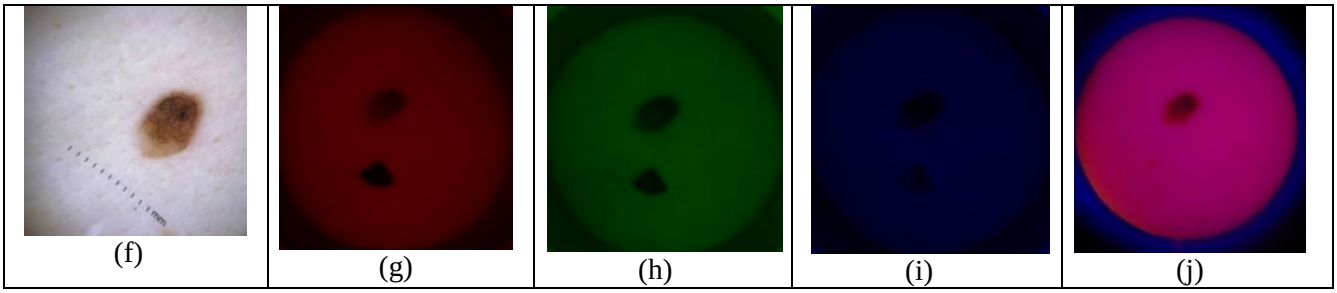

(f) (g) (h) (i) (j)

Dermal nevus

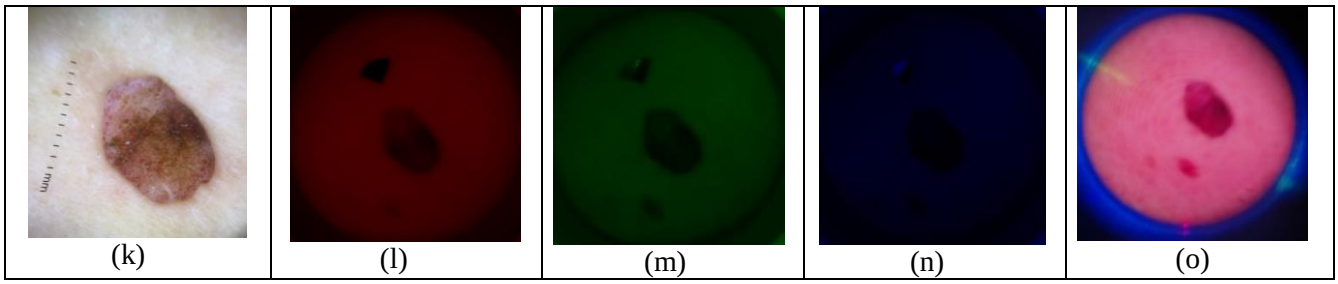

(k) (l) (m) (n) (o)

Seborrheic keratosis

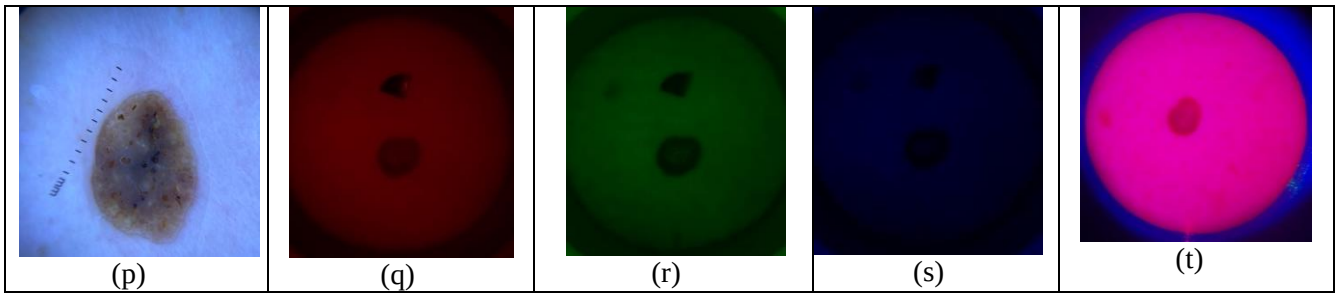

(p) (q) (r) (s) (t)

Hemangioma

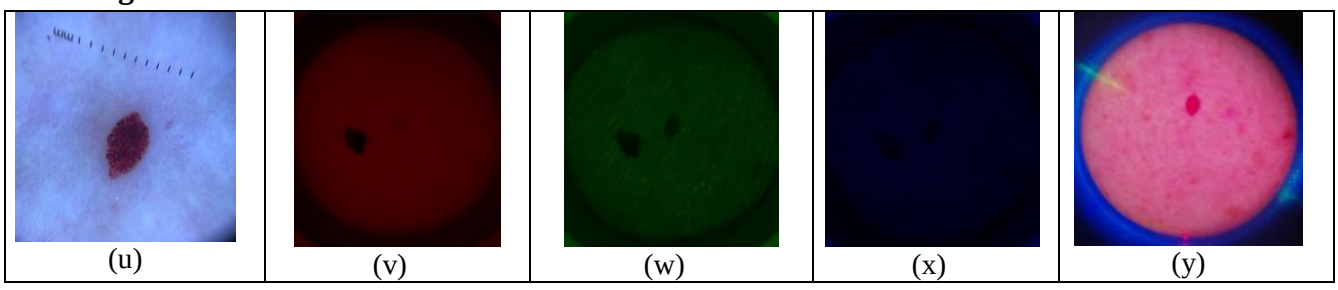

(u) (v) (w) (x) (y)

Fig. 4-6. Images of junctional, combined, and dermal nevi, seborrheic keratosis, and hemangioma: dermatoscopic image of the neoplasm (a, f, k, p, u), images in red (b, g, l, q, v), green (c, h, m, r, w), and blue (d, i, n, s, x) illumination captured by ***LED*** prototype and images captured under three wavelengths illumination (e, j, o, t, y) by ***Laser*** prototype.

LED prototype

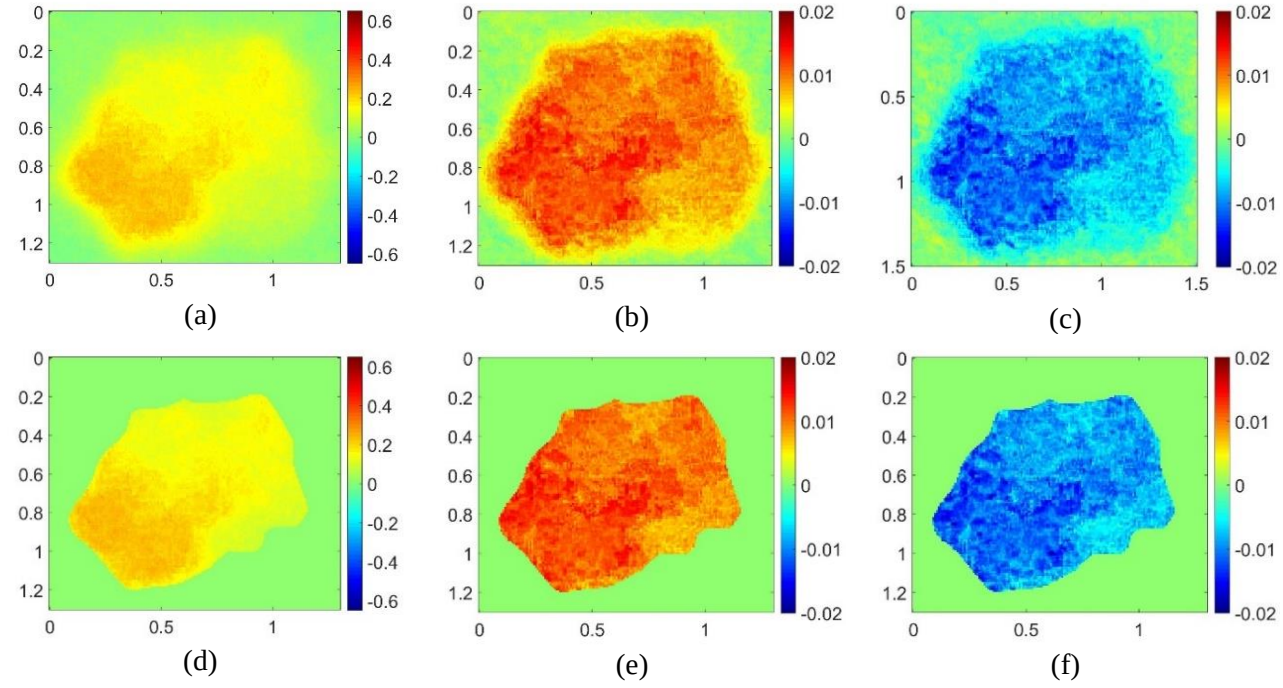

Laser prototype

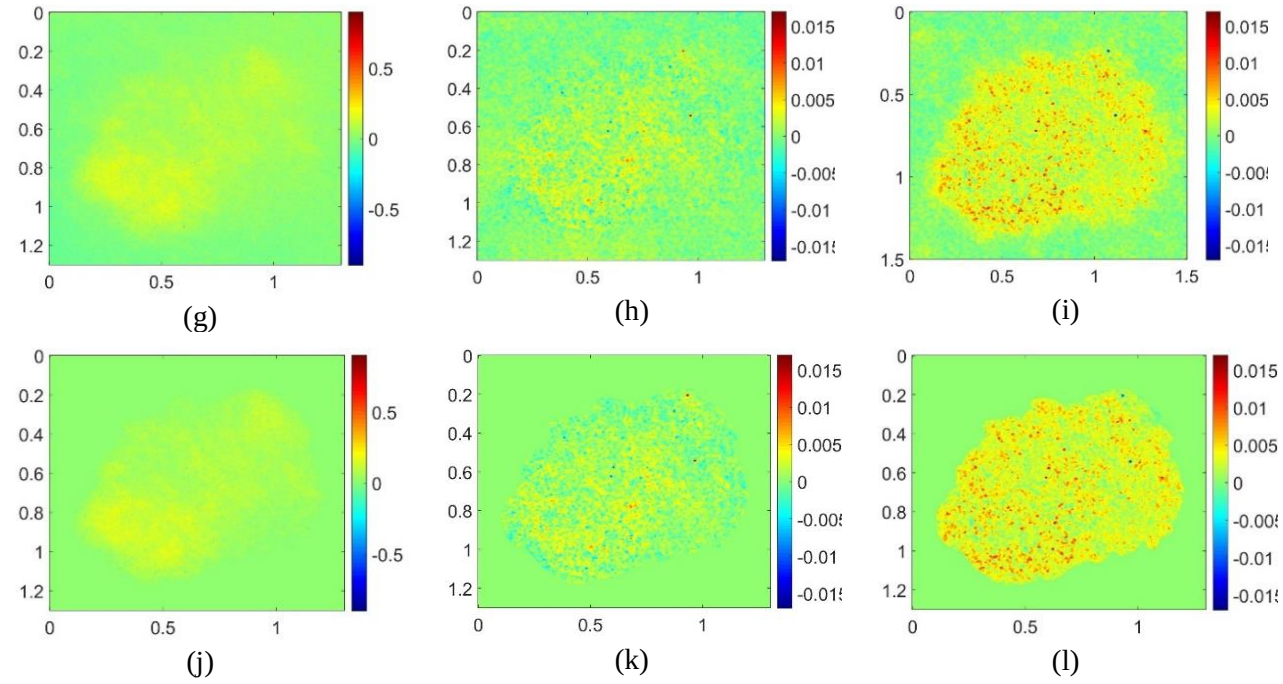

Fig. 4-7. Chromophore (a, b, c, g, h, i) and segmented chromophore(d, e, f, j, k, l) maps of melanin (a, d, g, j), oxy- (b, e, h, k) and deoxy-hemoglobin (c, f, i, l) for **junctional nevus** obtained from images of ***LED*** and ***Laser*** prototypes.

LED

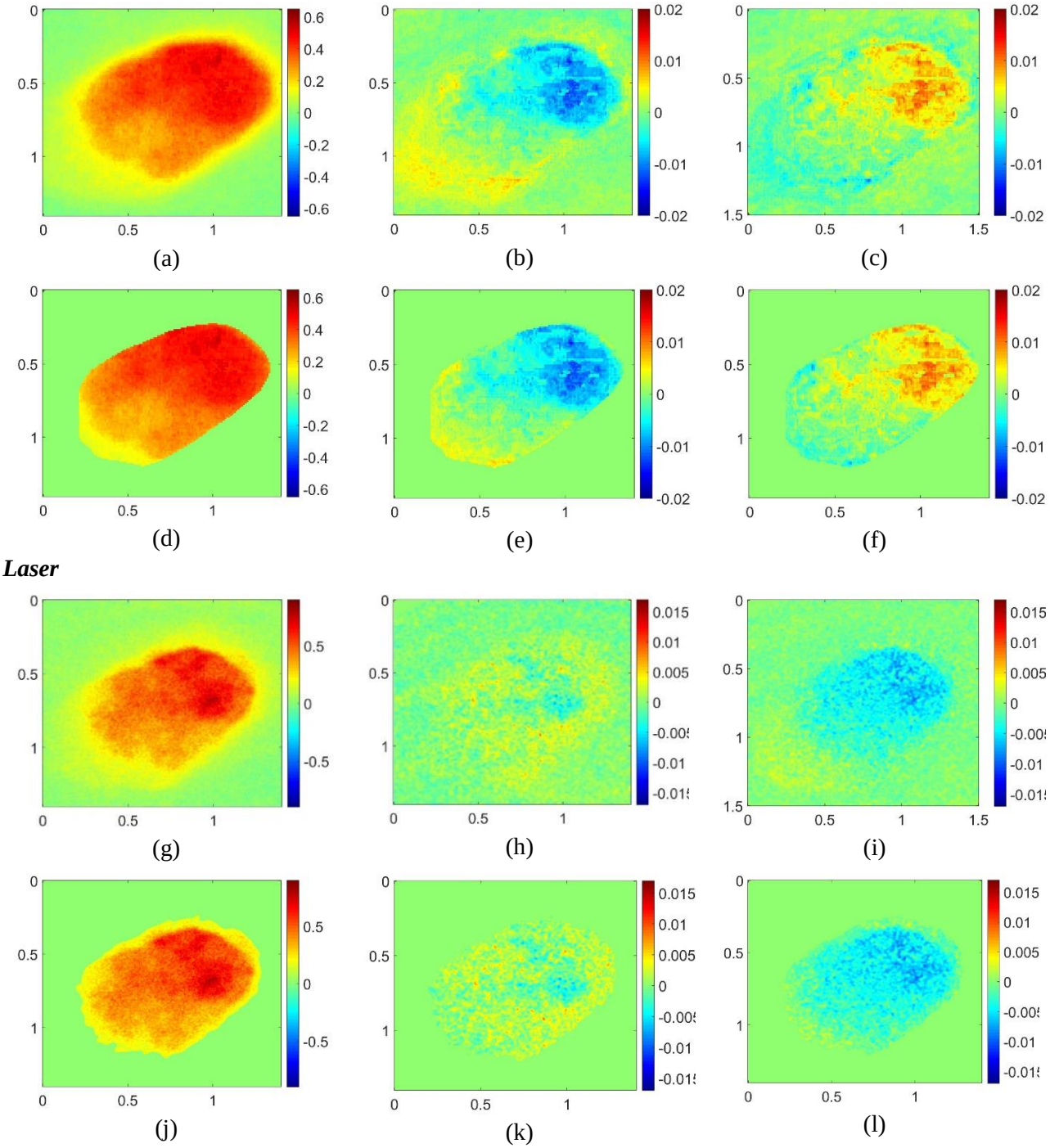

Laser

Fig. 4-8. Chromophore (a, b, c, g, h, i) and segmented chromophore(d, e, f, j, k, l) maps of melanin (a, d, g, j), oxy- (b, e, h, k) and deoxy-hemoglobin (c, f, i, l) for **combined nevus** from images of ***LED*** and ***Laser*** prototypes.

LED

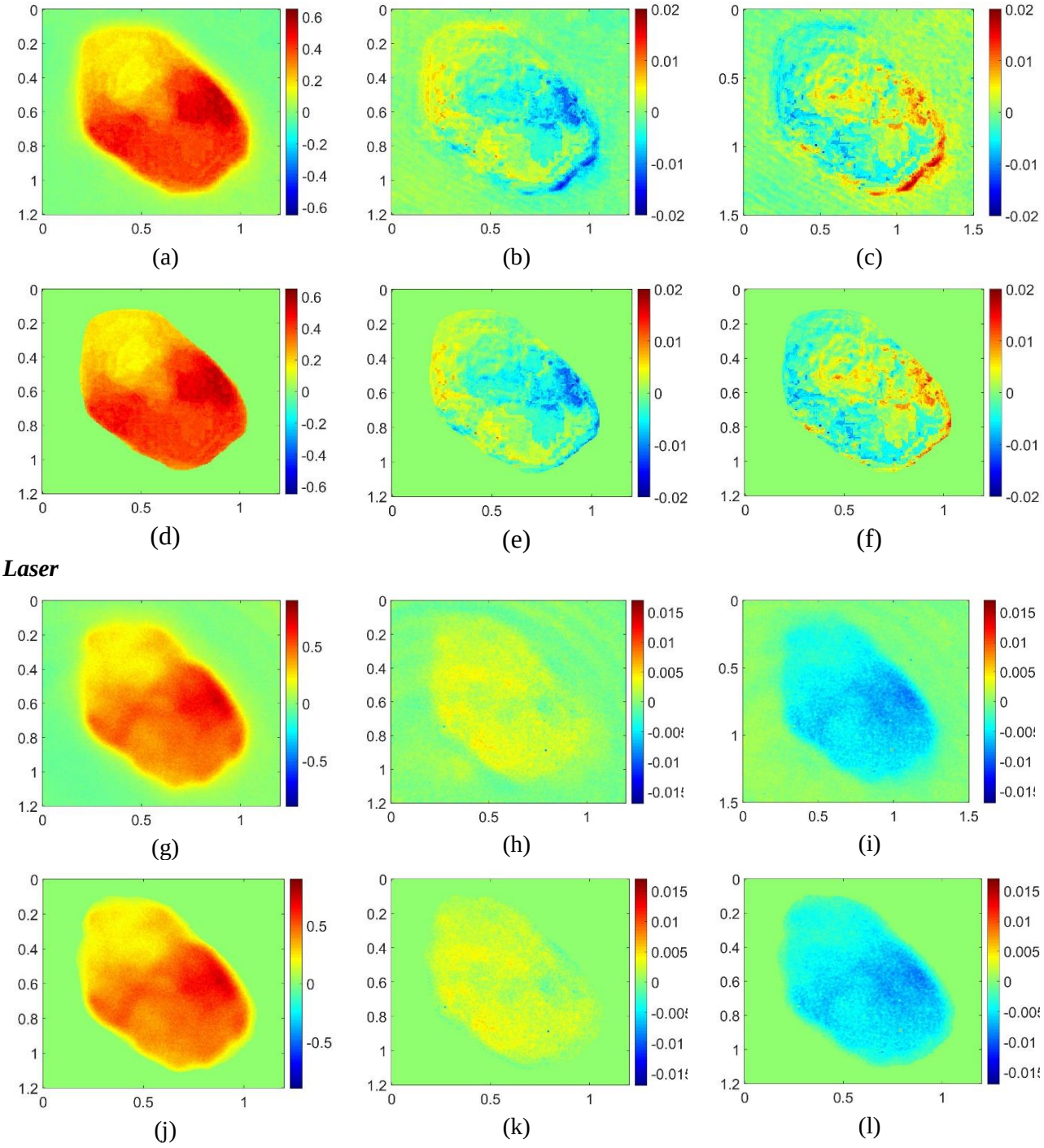

Laser

Fig. 4-9. Chromophore (a, b, c, g, h, i) and segmented chromophore (d, e, f, j, k, l) maps of melanin (a, d, g, j), oxy- (b, e, h, k) and deoxy-hemoglobin (c, f, i, l) for **dermal nevus** from images of ***LED*** and ***Laser*** prototypes.

LED

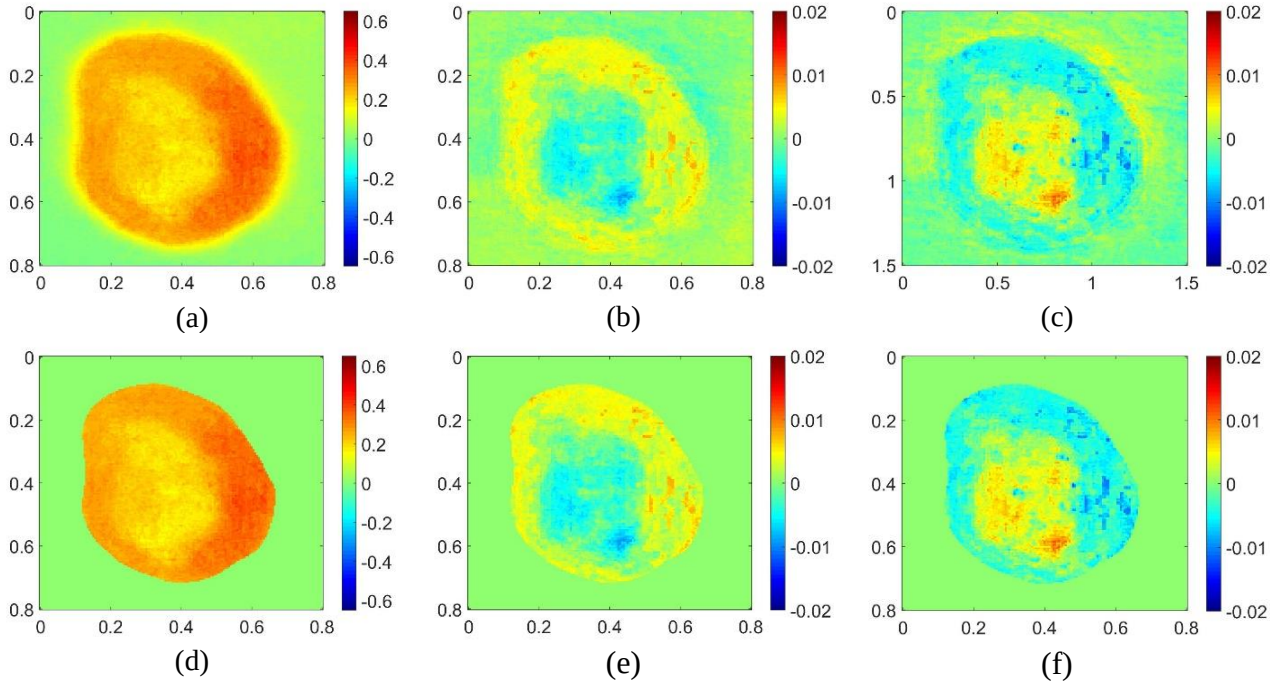

Laser

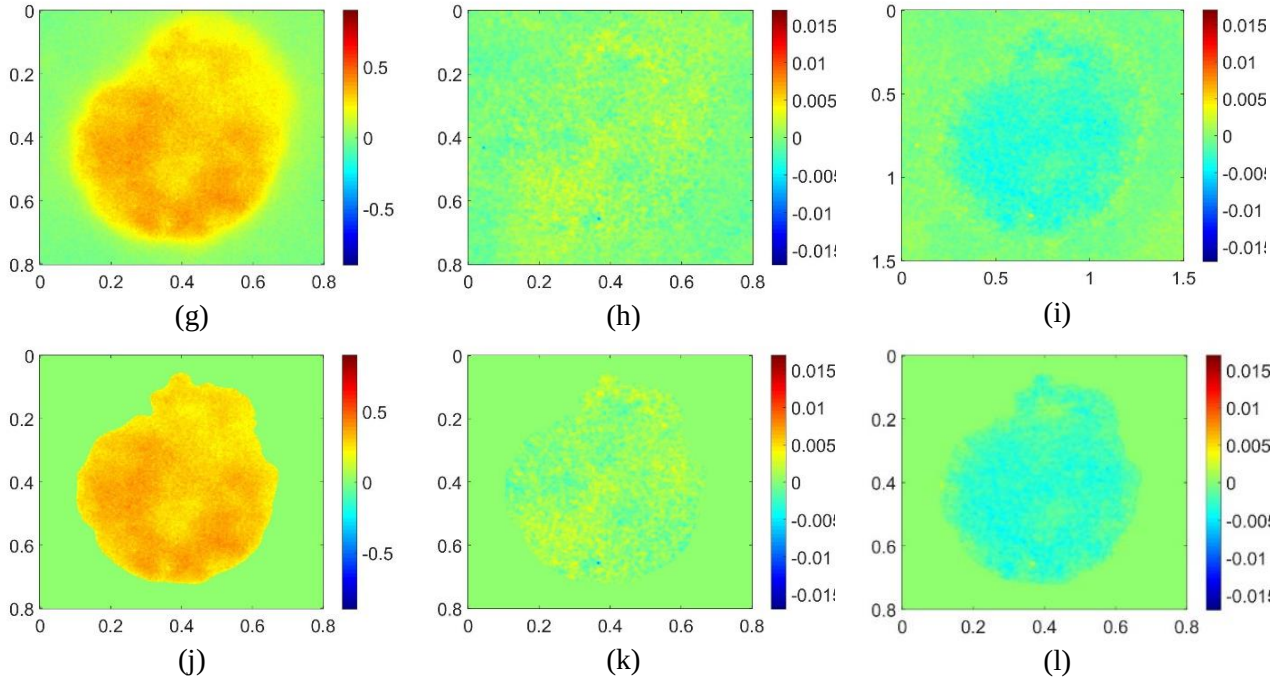

Fig. 4-10. Chromophore (a, b, c, g, h, i) and segmented chromophore (d, e, f, j, k, l) maps of melanin (a, d, g, j), oxy- (b, e, h, k) and deoxy-hemoglobin (c, f, i, l) for **seborrheic keratosis** from images of ***LED*** and ***Laser*** prototypes.

LED

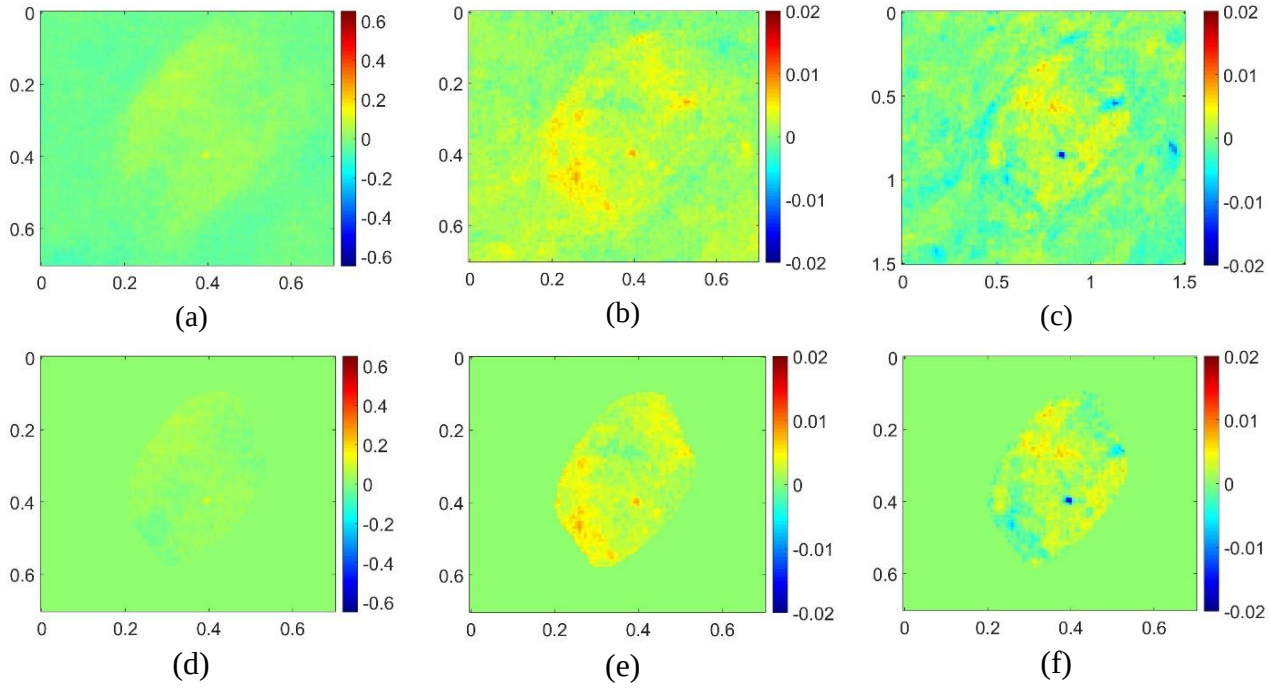

Laser

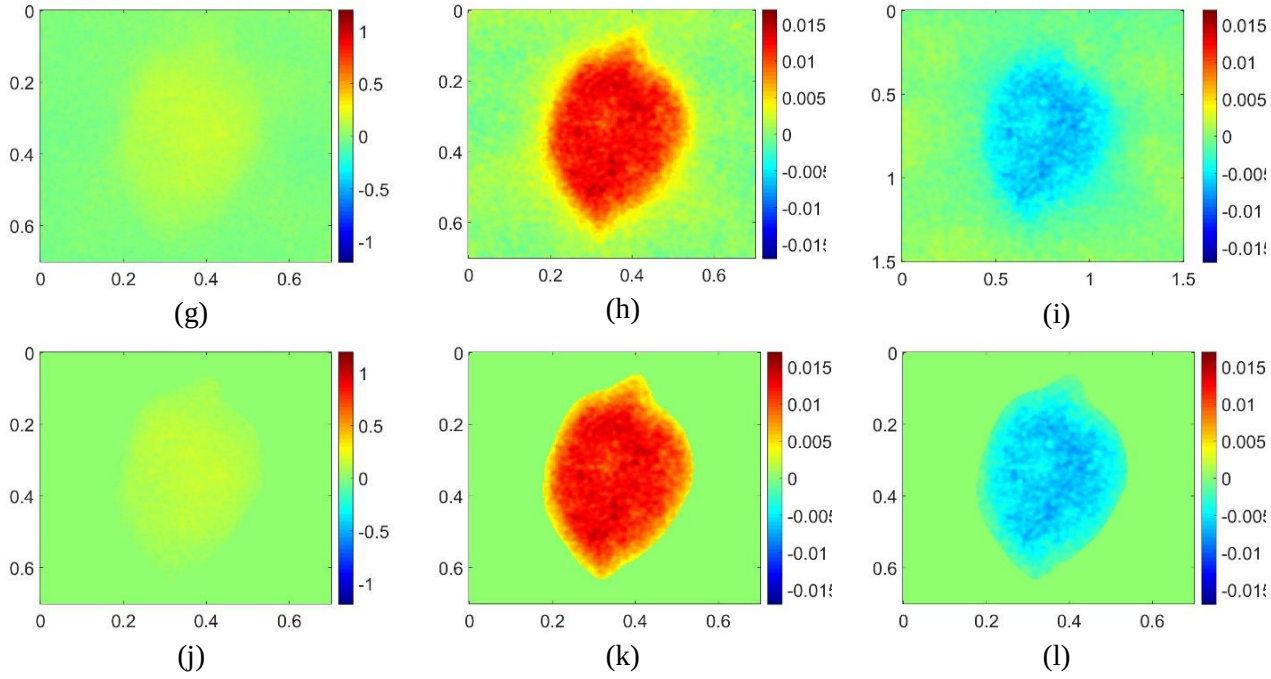

Fig. 4-11. Chromophore (a, b, c, g, h, i) and segmented chromophore(d, e, f, j, k, l) maps of melanin (a, d, g, j), oxy- (b, e, h, k) and deoxy-hemoglobin (c, f, i, l) for **hemangioma** from images of ***LED*** and ***Laser*** prototypes.

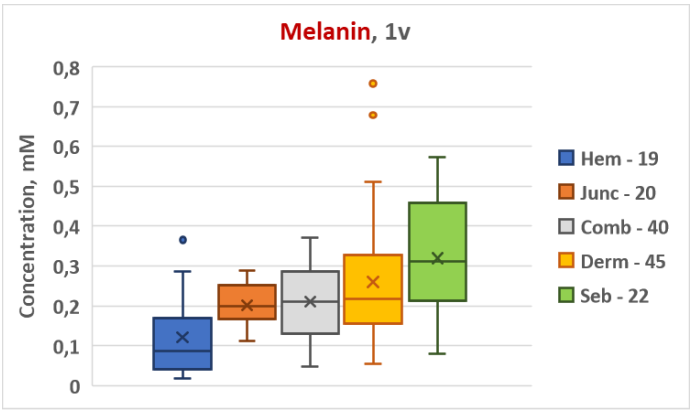

(a)

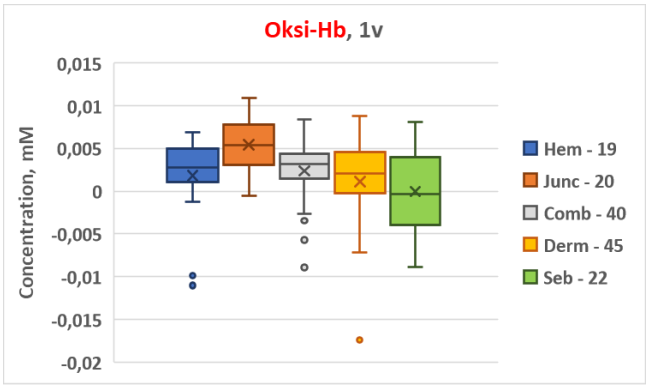

(b)

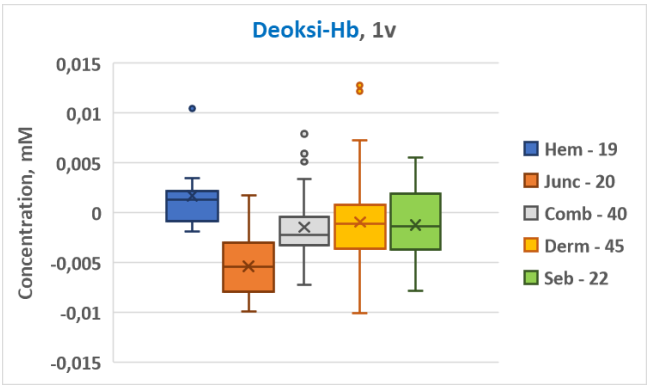

(c)

Fig. 4-12. Concentration (mean values) of melanin, oxy- and deoxy-hemoglobin for junctional (Junc), combined (Comb), and dermal (Derm) nevi, seborrheic keratosis (Seb) and hemangioma (Hem) obtained from images of ***LED*** prototype. **1v** – the algorithm without correction coefficients.

Figures 4-12 and 4-13 show statistical distribution of melanin, oxy- and deoxy-haemoglobin concentration (mean values) for junctional, combined, and dermal nevi, seborrheic keratosis and haemangioma obtained from images of ***LED*** prototype. The number of analysed neoplasms for each type is in the range from 20 to 35 indicated in the figures next to the neoplasm's name. The cross (x) inside each box indicates the mean value, the line inside the box – the median. Figure 4-12 shows the results obtained using calculation algorithm without correction coefficients (1v), Figure 4-13 – with correction coefficients considering absorption of epidermis and other skin chromophores (2v).

The algorithm without correction coefficients shows the lowest melanin concentration for haemangiomas (vascular neoplasms) compared to other pigmented neoplasms. The values of oxyhaemoglobin are similar among the neoplasms with a slightly higher value for junctional nevi. The mean values of deoxyhaemoglobin are positive and higher for haemangiomas compared to pigmented neoplasms with negative mean values.

The algorithm with correction coefficients shows positive values of melanin and deoxyhaemoglobin for all groups with the lowest mean value for haemangiomas and the highest for seborrheic keratosis. The mean values of oxyhaemoglobin are negative for all types of neoplasms with the less negative for haemangiomas.

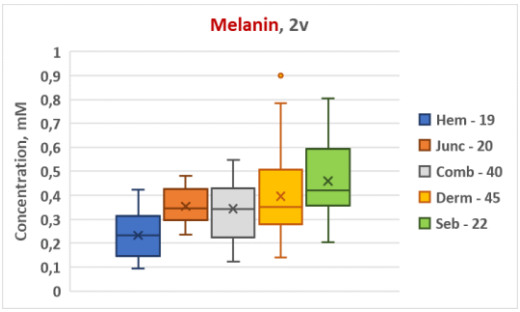

(a)

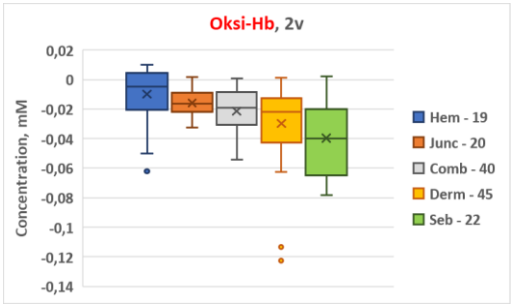

(b)

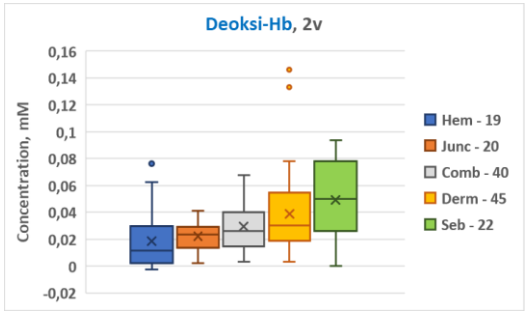

(c)

Fig. 4-13. Concentration (mean values) of melanin, oxy- and deoxy-hemoglobin for junctional (Junc), combined (Comb), and dermal (Derm) nevi, seborrheic keratosis (Seb) and hemangioma (Hem) obtained from images of ***LED*** prototype. **2v** – the algorithm with correction coefficients considering absorption of epidermis and other skin chromophores.

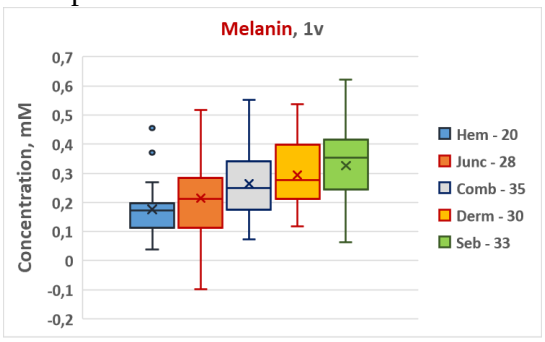

(a)

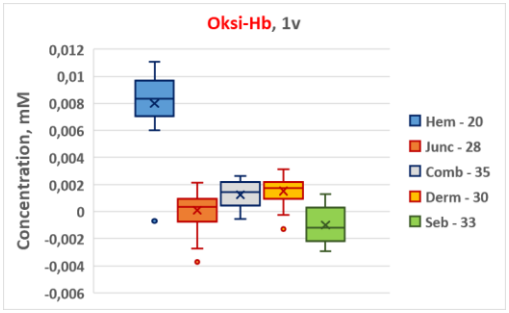

(b)

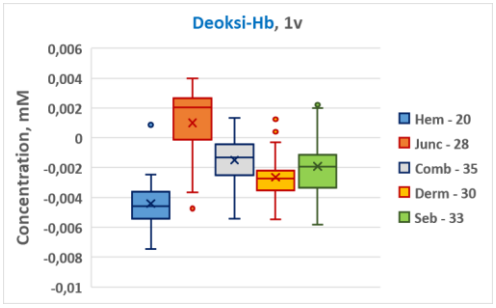

(c)

Fig. 4-14. Concentration (mean values) of melanin, oxy- and deoxy-hemoglobin for junctional (Junc), combined (Comb), and dermal (Derm) nevi, seborrheic keratosis (Seb) and hemangioma (Hem) obtained from ***Laser*** prototype. **1v** – the algorithm without correction coefficients.

Figures 4-14 and 4-15 show statistical distribution of melanin, oxy- and deoxy-haemoglobin concentration for junctional, combined, and dermal nevi, seborrheic keratosis and haemangioma obtained from ***Laser*** prototype. Figure 4-14 shows the results obtained using calculation algorithm without correction coefficients (1v), Figure 4-15 – with the correction coefficients considering absorption of epidermis and other skin chromophores (2v).

The algorithm without correction coefficients shows the best separation of the groups for each chromophore. The values of melanin are positive for all groups; the haemangiomas have the lowest values compared to other pigmented neoplasms. The values of oxyhaemoglobin are positive and the highest for the haemangiomas, nevi have the positive values much closer to zero, seborrheic keratosis – negative values. The mean values of the deoxyhaemoglobin are negative for all groups except the junctional nevi; the lowest values were observed for haemangiomas.

The algorithm with correction coefficients shows negative oxyhaemoglobin and melanin mean values for all groups, with highest (less negative) values for haemangiomas and junctional nevi. The values of deoxyhaemoglobin are positive for all groups with the lowest - for haemangiomas and the highest – for seborrheic keratosis.

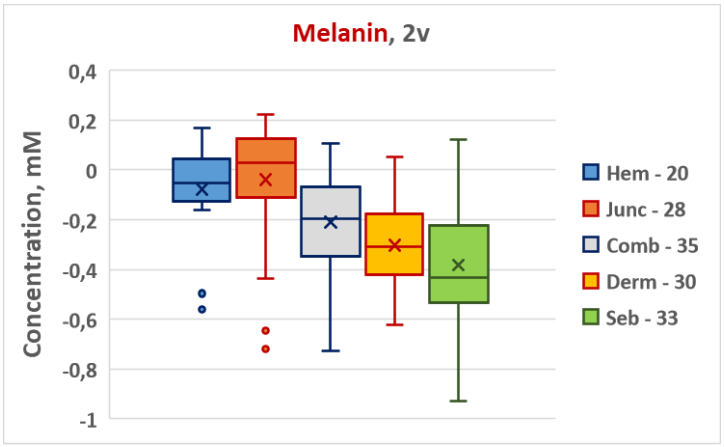

(a)

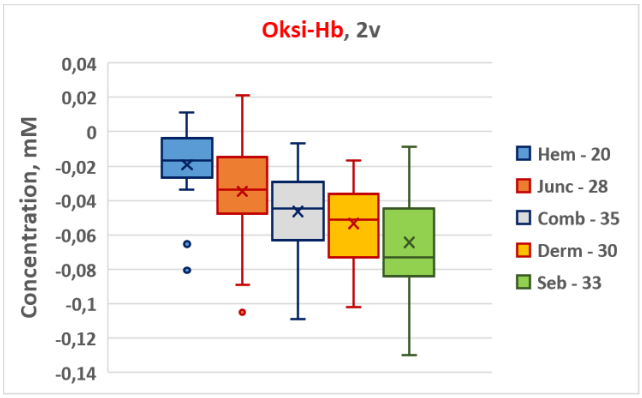

(b)

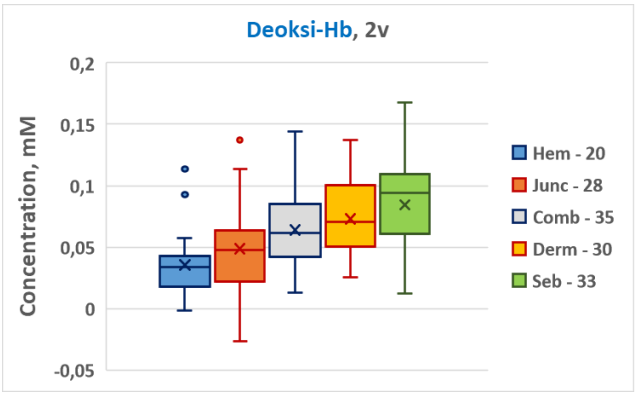

(c)

Fig. 4-15. Concentration (mean values) of melanin, oxy- and deoxy-hemoglobin for junctional (Junc), combined (Comb), and dermal (Derm) nevi, seborrheic keratosis (Seb) and hemangioma (Hem) obtained from ***Laser*** prototype. **2v** – the algorithm with correction coefficients considering absorption of epidermis and other skin chromophores

Conclusions

1. The analysis of *in vivo* picosecond kinetic measurements shows that the mean photon path length:
   - is different for skin and neoplasms, especially at large distances between fibres (starting from 12 mm)

- depends on the type of neoplasm (intradermal nevus, combined nevus, and junctional nevi) at larger distances between optical fibres (12 mm).
- is higher for the neoplasms with deeper anatomical location of pigments.

2. The analysis of *in vivo* RGB images shows that:
   - The algorithm without correction coefficients (1v) demonstrates more credible results, considering the melanin and haemoglobin concentration in vascular and pigmented neoplasms, compared to the algorithm with correction coefficients (2v).
   - The results obtained from the images of the ***Laser*** prototype demonstrate better separation of the vascular and pigmented neoplasms compared to ***LED*** prototype.

A2.1. *Assembling a compact prototype for single-point fluorescence lifetime measurements*

May – October 2019

The main contributors: Dr.phys. Vanesa Lukinsone and MSc student Maris Kuzminskis

Prototype of a portable FLT measurement unit

Compact fluorescence lifetime (FLT) prototype able to measure time-varying fluorescence kinetics of objects (e.g. skin, phantoms) with picosecond range resolution has been developed. It includes a set of picosecond pulse lasers (broadband 0.4-2.0 micron WhiteLase Micro and 3 lasers with fixed wavelengths of 405 nm, 470 nm and 510 nm), HPM-100-07 high speed photo detector, optical narrowband filter set and optical fiber drive systems, as well as a computerized system for recording and processing results (Fig. 5-1). The initially used monochromator has been replaced by an interference filter kit that takes up less space. The prototype gauge does not exceed 80x60x40 cm, is easily wheeled and can be used for both laboratory and clinical fluorescence pulse measurements from a fixed point area. The planned laptop was replaced with a desktop and monitor, which makes the device ergonomic. The desktop and monitor are removable as needed. By attaching a dual-mirror, digitally controlled laser beam scanner to the device, it can also be used to obtain fluorescence lifetime distribution images. In addition, the prototype device is capable of measuring photon time-of-flight (PTOF) distribution in various environments, incl. skin and skin models.

The laser with the controller, the data processing system, the power supply unit and the communication cables are all enclosed in housing on wheels with mechanical brakes (Fig. 5-1, 5-2). The data processing monitor and control keypad with a touch panel are mounted on a telescopic stand with a work surface (Fig. 5-1). It is possible to change the height of the work surface, as well as to change the tilt and angle of rotation of the monitor. The HPM-100-07 detector and focusing system are positioned on the housing, providing easy access to filter replacement (Fig. 5-3 (a)). Depending on the configuration, the

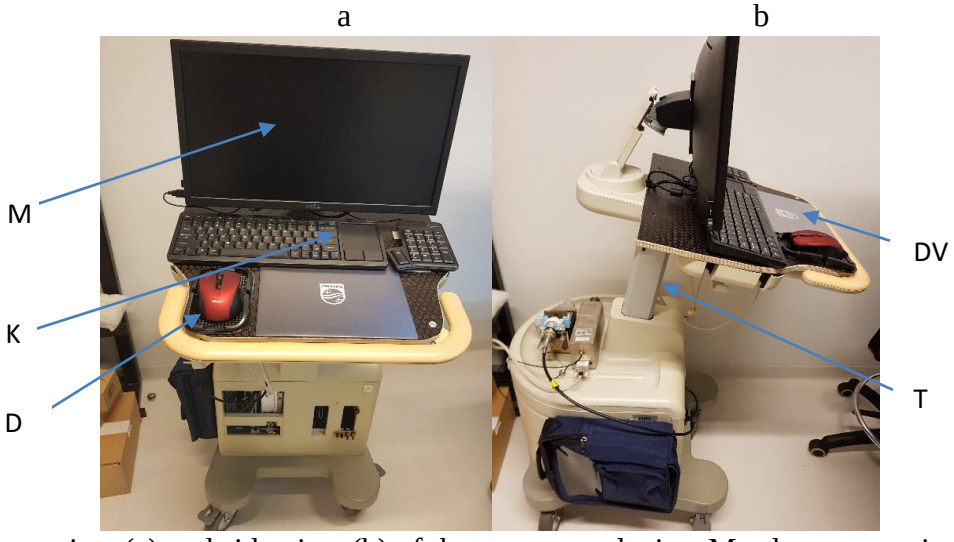

Fig. 5-1. Front view (a) and side view (b) of the prototype device. M - data processing system monitor, K - touch control keypad, DP - computer mouse, DV - work surface, T – height-adjustable telescopic stand.

detector and focusing system are connected to a fiber optic probe in one of the positions: 1, 8, 12, 16 or 20 mm (Fig. 5-3 (b)), 2D scanner or Y-type optical fiber assembly.

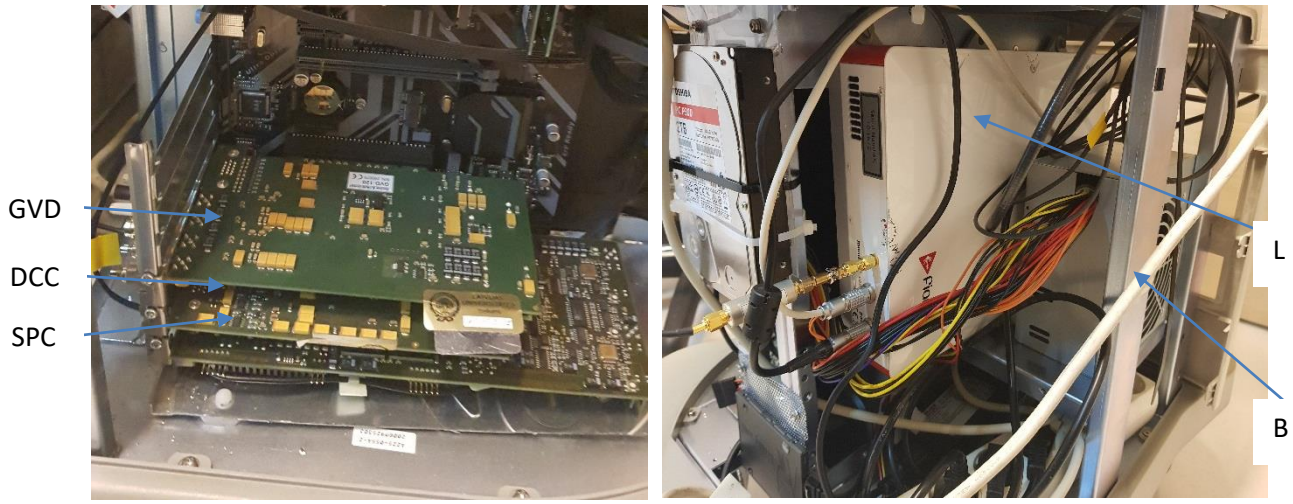

a b

Fig. 5-2. Side view of data processing system from right (a) and left (b). GVD - GVD120 scanner controller, DCC - DCC100 detector controller, SPC150 - TCSPC processing module, L - picosecond pulse laser, B - power supply.

a b

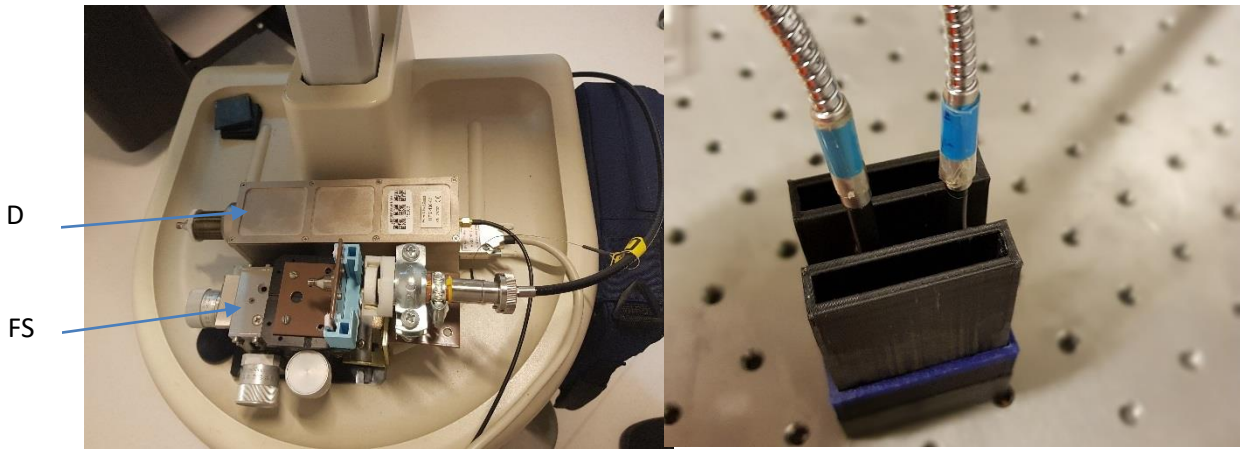

Fig. 5-3. HPM-100-07 Detector and Focusing System (a) and Optical Fiber Probe (b). D - High Speed Photo Detector, FS - Focusing System with Filter Holder.

Main components:

• Data Processing System - PCI Modules Integrated in HP Workstation:
  - o SPC -150 TCSPC Processing Module;
  - o GVD-120 scanner controller;
  - o DCC-100 detector controller;
• NKT Photonics picosecond pulse laser WhiteLase Micro with 400 - 2000 nm spectral frequency, 20 MHz;
• 3 picosecond lasers with fixed wavelengths of 405, 470 and 510 nm, PicoQuant PDL 800-D.
• Becker & Hickl Detector HPM-100-07 with filters;
• Self-made focusing system with interference filter holders and interference filter kit;
• Multi-channel probe for optical fiber positioning – 1, 8, 12, 16, 20 mm;
• Collecting optical fiber - silica glass core diameter 200 µm;
• Lead fiber - silica glass core diameter 200 µm;
• Software for data collection and processing SPC Becker & Hickl, SPCImage Becker & Hickl;
• Compatible to a self-made laser scanner of two digitally controlled mirrors to the output.

Configuration of single point fluorescence lifetime measurement system

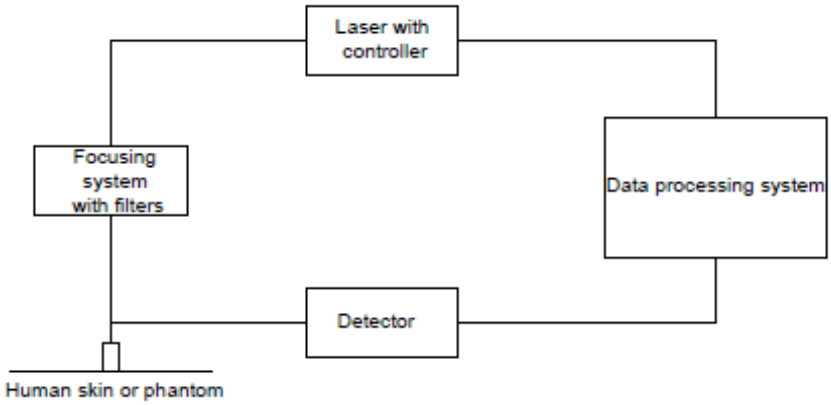

Fig. 5-4. Principle diagram of a single-point fluorescence lifetime measurement configuration.

One of the picosecond pulse lasers (for example, WhiteLase Micro or PicoQuant) is synchronized with the TPSPC SPC-150 data processing module and is connected to a Y-shaped optical fiber with a 200 µm quartz glass core diameter. The fiber optic outlets are positioned on the skin or phantom so that the target surface forms an angle of 90 degrees with it. The collecting optical fiber is connected to the HPM-100-07 detector with an interference filter appropriate for the spectrum to be measured. The detector is connected to the control module DCC-100 and TCSCP control board. The data processing system is controlled through a graphical user interface, where the measurement settings are changed and the measurement data is displayed. Figure 5-4 shows a schematic diagram of the measuring device.

Configuration of photon time-of-flight measurement system

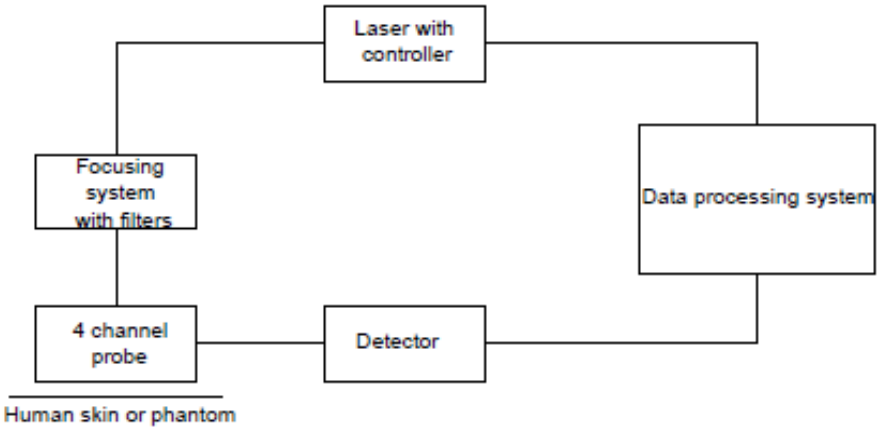

Fig. 5-5. Principal diagram of a photon time-of-flight measurement configuration.

One of the picosecond pulse lasers (such as WhiteLase Micro or PicoQuant) is synchronized with the TCSPC SPC-150 data processing module and is connected to a silica glass optical fibe with 200 µm core. The output end of the optical fiber is mounted in the housing of a self-made probe. The collecting optical fiber (silica glass core, 200 µm diameter) is mounted on the probe at one of the positions: 1, 8, 12, 16 or 20 mm parallel to the input laser fiber. The collecting optical fiber is connected to the detector HPM-100-07 with an input radiation appropriate interference filter. The detector is connected to the control module DCC-100 and TCSCP control board. The data processing system is controlled through a graphical user interface, where the measurement settings are changed and the measurement data is displayed. The probe is positioned on the skin or phantom so that the surface of the skin or phantom forms an angle of 90 degrees with optical fiber axis. Figure 5-5 shows a schematic diagram of a measuring device.

Fluorescence lifetime imaging (2D-distribution) measurement configuration

One of the picosecond pulse lasers (such as WhiteLase Micro or PicoQuant) is synchronized with the TCSPC SPC-150 data processing module and is connected to a 200 μm silica core optical fiber which is attached to a self-made 2D scanner with a maximum measurement area of 1 cm^2 and adjustable resolution from 8x8 to 1024x1024 pixels. The scanner is controlled by the GVD-120 scanner control module. The collecting optical fiber is connected to the HPM-100-07 detector with an interference filter appropriate for the wavelength to be measured. The detector is connected to the control module DCC-100 and TCSCP control board. The data processing system is controlled through a graphical user interface, where the measurement settings are changed and the measurement data is displayed. Figure 5-6 shows a schematic diagram of a measuring device.

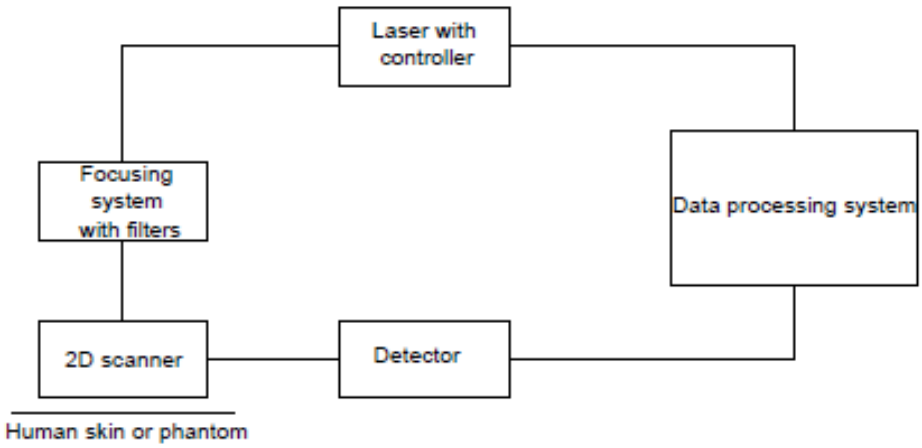

Fig. 5-6. Principle Schematic of Fluorescence Lifetime 2D Distribution Measuring Device Configuration.

Measurement application SPC settings

The configuration of the measurement settings in the SPC application is changed according to the type of measurement (PTOF, FLT) a guided by the manufacturer's instructions and specifications (Fig. 5-7).

Data processing

Data processing is performed by the Becker & Hickl SPC Image application according to the manufacturer's instructions (Fig. 5-8).

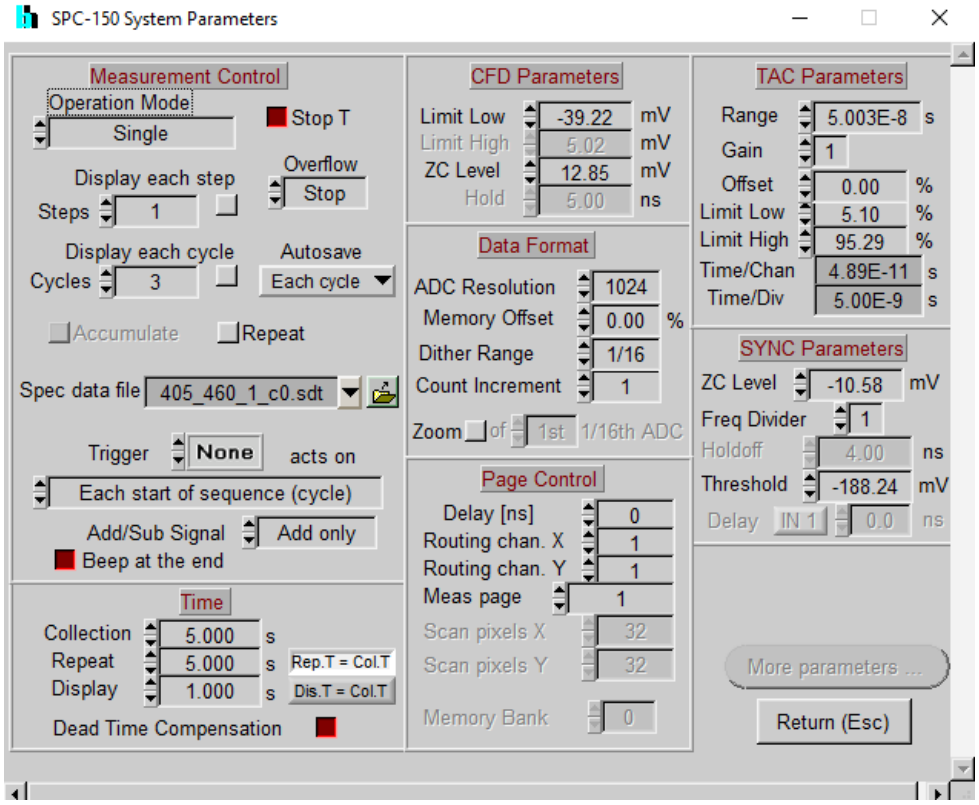

Fig. 5-7. Settings of SPC measurement application.

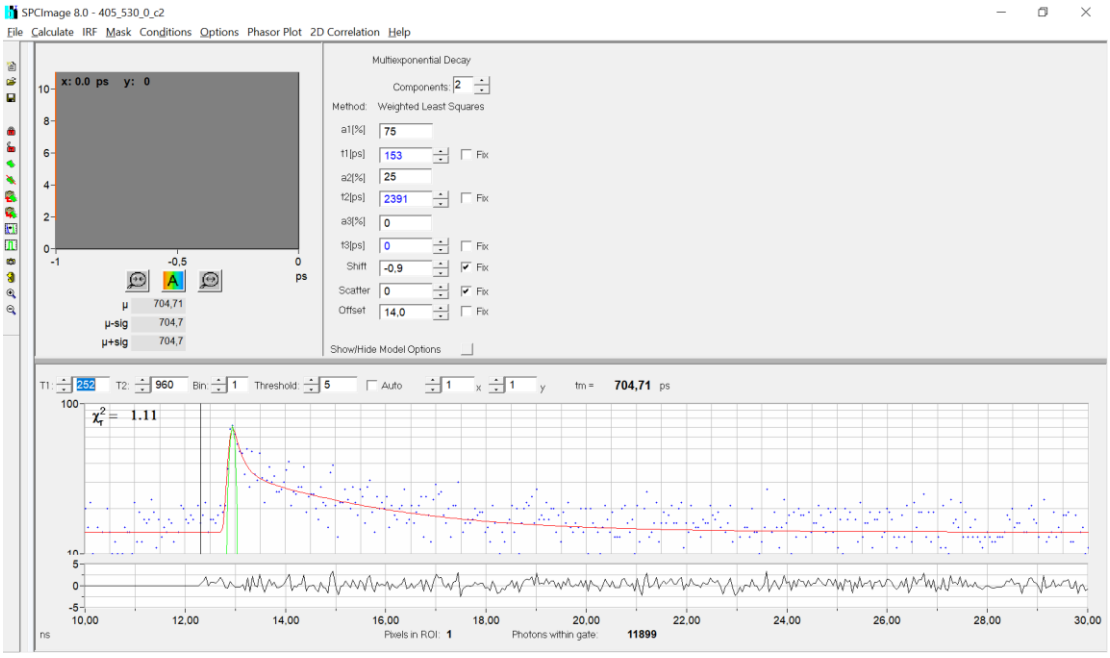

Fig. 5-8. Data processing of single point fluorescence lifetime (SPFLT) measurements.

Laboratory test results

Integration of the main measuring equipment components into one housing; collaboration functionality was tested in the laboratory by measuring on various phantoms corresponding to technology readiness level 4 (TRL = 4). Single-point fluorescence lifetime (SPFLT) measurements were taken, Fig. 5-9. shows the screen shot taken during the measurement.

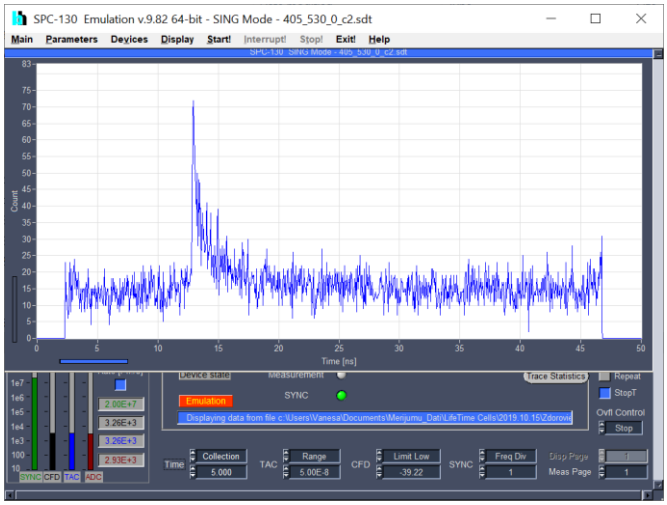

Fig. 5-9. Fluorescence pulse shape measured to determine SPFLT.

Measurements of the skin-scattered photon arrival time distribution were also taken. The photon propagation time varies with the distance between the input and the receiving optical fiber (Fig. 5-10).

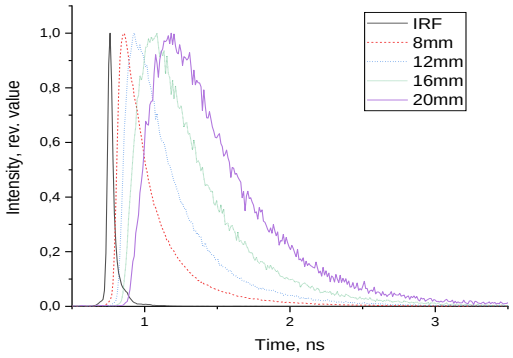

Fig. 5-10. Comparison of photon propagation time for measurements at different distances between input and capture optical fibers.

Summary

A compact, wheeled prototype for fluorescence lifetime measurements with picosecond resolution in the 400-800 nm spectral range was developed and experimentally tested. The design of the device additionally ensures determination of the back-scattered photon temporal distribution which allows experimental determining of the remitted photon path length distributions. Additionally, it is possible to connect a laser beam scanner to the prototype in order to display the fluorescence lifetime spatial (x-y) distribution. The device prototype in terms of dimensions, composition, parameters and functionality is fully in line with that planned in the project application.

A2.2. *Updates of the AFLTI system*

May 2019 – January 2020

The main contributors: Dr.phys. Vanesa Lukinsone, MSc student Maris Kuzminskis

Updated AFLTI system

The autofluorescence lifetime imaging (AFLTI) system was updated internally and externally (Figs. 6-1 and 6-2). The 2D mirror scanner components were mounted on ebonite plate, which reduces noise related to the fluorescence of the material. A focusing lens was added to the system, which improved the

efficiency of signal collection. 3D printed mounts for focusing lenses, optical fiber and galvanometer scanner were made with the possibility to adjust the distance between the elements. The monochromator can be removed or used in conjunction with a self-made focusing system comprising interference filter holders

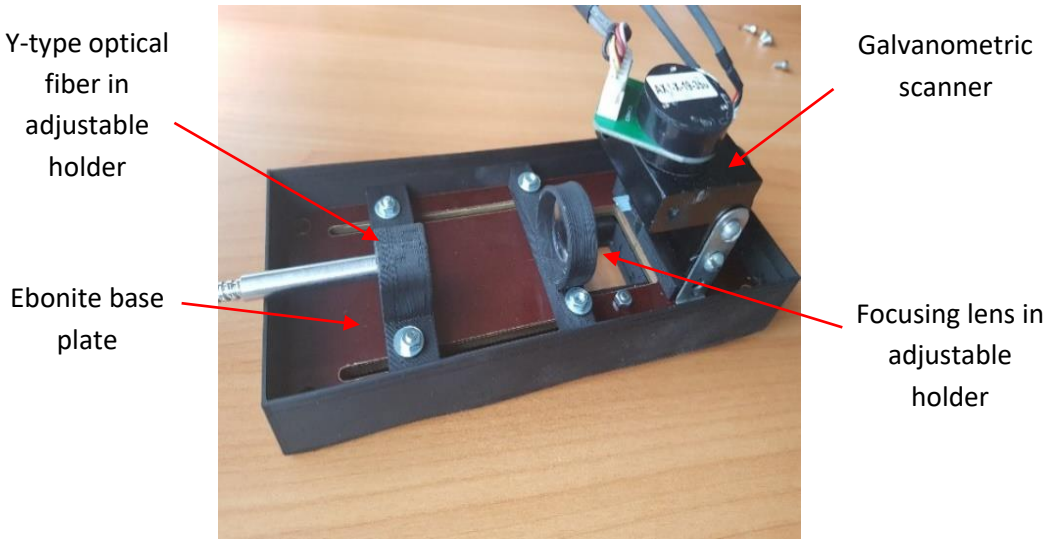

Fig. 6-1. Dual axis two mirror galvanometric scanner with focusing lens and Y-type optical fiber mounted to ebonite base plate.

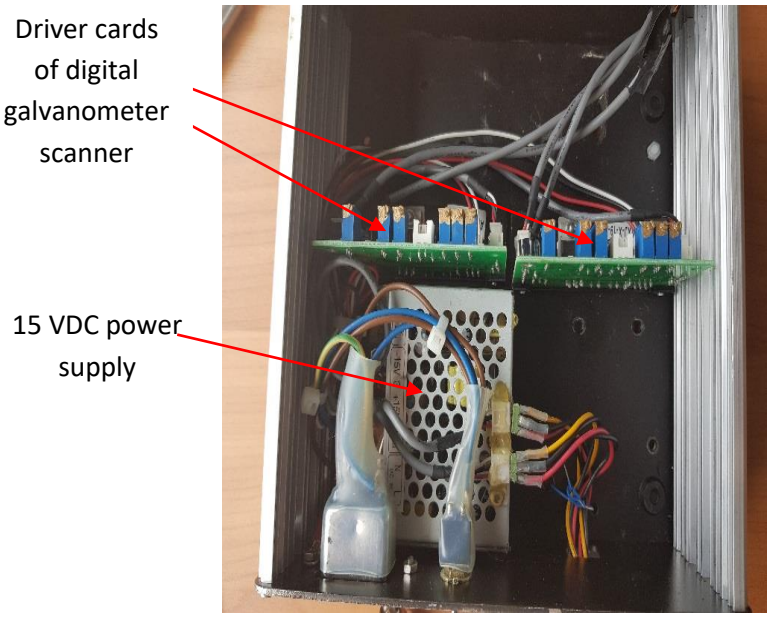

Fig. 6-2. Driver cards of galvanometer scanner and 15V DC power supply.

and an interference filter kit. A 3D printed holder with quartz glass plate is attached to the ebonite plate, which is in contact with the phantom or human skin surface during the measurements. A new 3D printed system body has been developed that makes the scanner easier and more ergonomic to use with one hand (Fig. 6-3). The scanner was connected and synchronized with the measurement system developed in the activity A2.1.

Main components:

• Data Processing System - PCI Modules Integrated in HP Workstation:

- SPC-150 TCSPC Processing Module;
- GVD-120 scanner controller;
- DCC-100 detector controller;

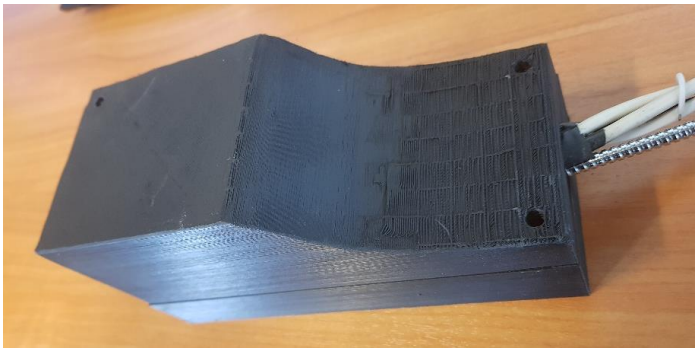

Fig. 6-3. Scanner in an ergonomic custom 3D-printed holder.

- NKT Photonics picosecond pulse laser WhiteLase Micro with 400 - 2000 nm spectral frequency, 20 MHz;
- 3 picosecond lasers with fixed wavelengths of 405 nm, 470 nm and 510 nm, PicoQuant PDL 800-D.
- Becker & Hickl Detector HPM-100-07 with filters;
- Self-made focusing system with interference filter holders and interference filter kit;
- Y-type lead and collecting optical fiber - quartz glass core diameter 200 µm;
- Software for data collection and processing SPC Becker & Hickl, SPCImage Becker & Hickl;
- Digital dual axis two mirror galvanometric scanner with servo driver cards and 15 VDC power supply in custom holder;
- Focusing lens.

One of the picosecond pulse lasers (such as WhiteLase Micro or PicoQuant) is synchronized with the TPSPC SPC-150 data processing module and is connected to a 200 µm quartz glass core optical fiber which is attached to a self-made 2D scanner with a maximum measurement area of 1 cm^2 and adjustable resolution from 8x8 to 1024x1024 pixels. The scanner is controlled by the GVD-120 scanner control module. The collecting optical fiber is connected to the HPM-100-07 detector with an interference filter or monochromator appropriate for the wavelength to be measured. The detector is connected to the control module DCC-100 and TCSPC control board. The data processing system is controlled through a graphical user interface, where the measurement settings are changed, and the measurement data is displayed. Figure 6-4 shows a schematic diagram of a measuring device. Figure 6-5 shows measurement example with the updated AFLTI system. Please refer to the A2.4 report for detailed measurement results description.

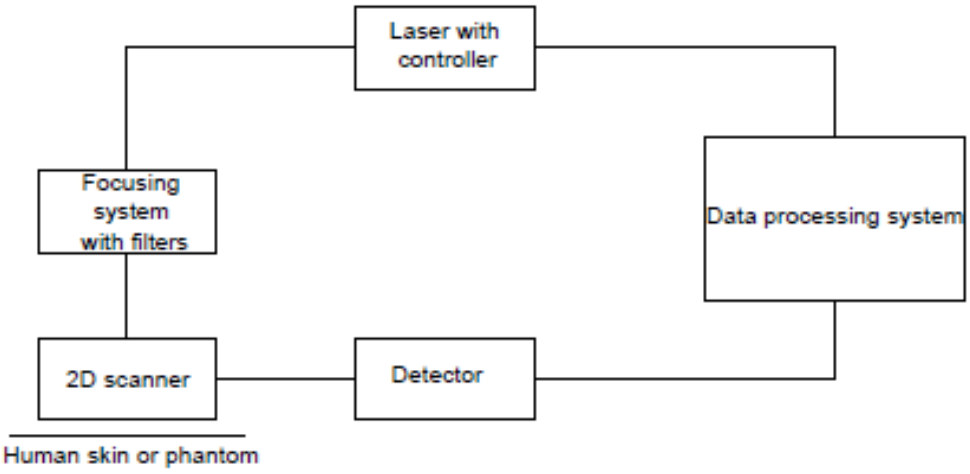

Fig. 6-4. Principle schematic of fluorescence lifetime 2D imaging device.

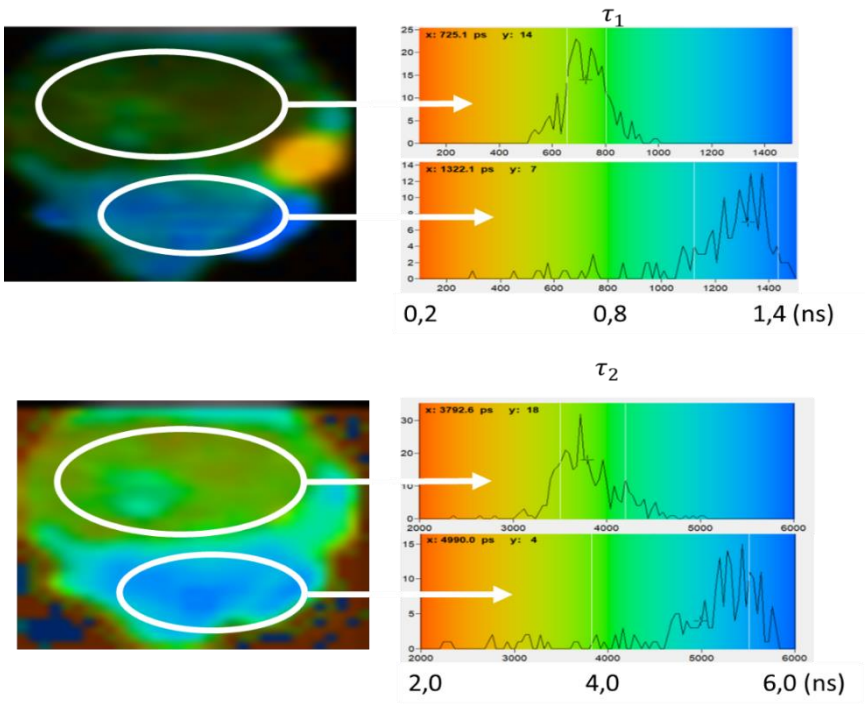

Fig. 6-5. FLTI measurement example: skin malformation and surrounding healthy skin are compared in terms of spatial distribution of two lifetime components.

A2.3. *Calibration measurements of autofluorescence lifetimes in cell cultures*

August 2019 – January 2020

The main contributors: Dr.phys. Vanesa Lukinsone, Dr.phys. Mindaugas Tamosiunas, MSc student Anna Maslobojeva

Measurement data set

Theoretical background: NAD(P)H and FAD

Much attention is paid to NAD(P)H (reduced form of NADH and NADPH) and FAD (oxidized form) endogenous fluorophore studies. NADH and FAD fluorophores participate in the cell metabolism by ensuring oxidation-reduction reactions in the cell membrane [1-3].

NAD(P)H fluoresces in the reduced form, but not in the oxidized form, whereas FAD fluoresces in the oxidized form but not in the reduced form (when reduced to $FADH_2$). Along with changes in the fluorescence intensity from NADH and FAD, the redox state in tissues also changes. Redox dependency ratio presents an oxidized or reduced state in tissues. The metabolism is more oxidative in healthy tissue cells, and more reductive in cancerous cells. NADH and FAD fluorescence is excited by near ultraviolet radiation (350 nm–375 nm) NAD(P)H fluorescence is observed in the blue spectral range of 450 nm– 475 nm, while fluorescence from FAD is observed in the green spectral range of 530 nm – 550 nm [4 – 10].

TRES

The TRES (time-resolved emission spectroscopy) analysis method investigates how the spectral form changes at the time of decay after the interruption of excitation, i.e., it investigates the time evolution of the emission spectrum. Depending on the number of fluorophores with different lifetimes and spectral forms that are involved in the process, the spectral form changes over time. The principle of TRES is shown in Figure 7-1, where the wavelength (λ) is depicted on the axis of the abscissa and intensity on the axis of ordinates (I) [11].

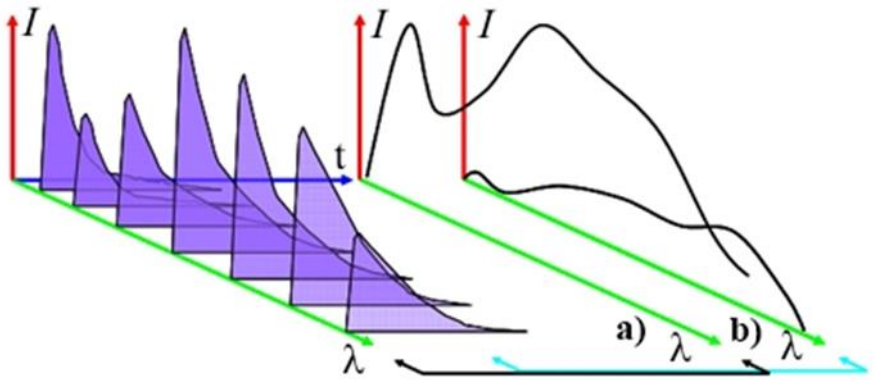

Fig. 7-1. TRES method schematic.

Measurement set-up

The impact of photobleaching on spectral parameters of cells was studied using time-resolved fluorescence spectroscopy with resolution of ~10^{-10}s in spectral range 460-540 nm. The measurements were registered using the TCSPC system and 405 nm laser for AF signal excitation. The AF photobleaching lasted 3 min with continuous 405 nm wavelength irradiation. Measurements of AF lifetime were performed using a single point system. An experimental set-up scheme is on fig.7-2.

The experimental set-up consists of:

- TCSPC (*Time-correlated single photon counting*): SPC – 150, Becker&Hickl;
- optical fiber Y-beam; the diameter of each optic fiber core is 200 μm;
- lasers: PicoQuant, LDH-D-C-405 (pulse half-width 59 ps);
- detector: hybrid photomultiplier HPM-100-7, Becker & Hickl;
- monochromator with spectral resolution 5 nm.

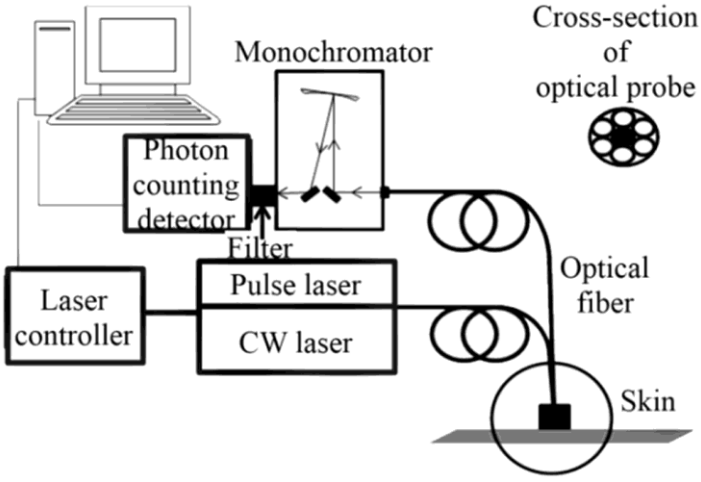

Fig. 7-2. Fluorescence lifetime single point measurement set-up scheme.

Measurement process

The cells cultures were provided form Biophysical Research Group at Vytautas Magnus University (Lithuania) and prepared for measurements. The laser beam was delivered to a cuvette with cell volume of 100 microliters via optical fiber. The measurements of AF lifetime were performed with 405 nm picosecond laser impulse irradiation in spectral range 460 – 520 nm, before and after photobleaching. With 405 nm continuing wavelength irradiation (~40 mW / cm^2), photobleaching was done 3 minutes.

The results of the measurements were registered with program *Spcm64 (Becker & Hickl GmbH)*. The results obtained were processed with the program *SPCImage (Becker & Hickl GmbH)* and *Origin 2019b*.

Data processing scheme:

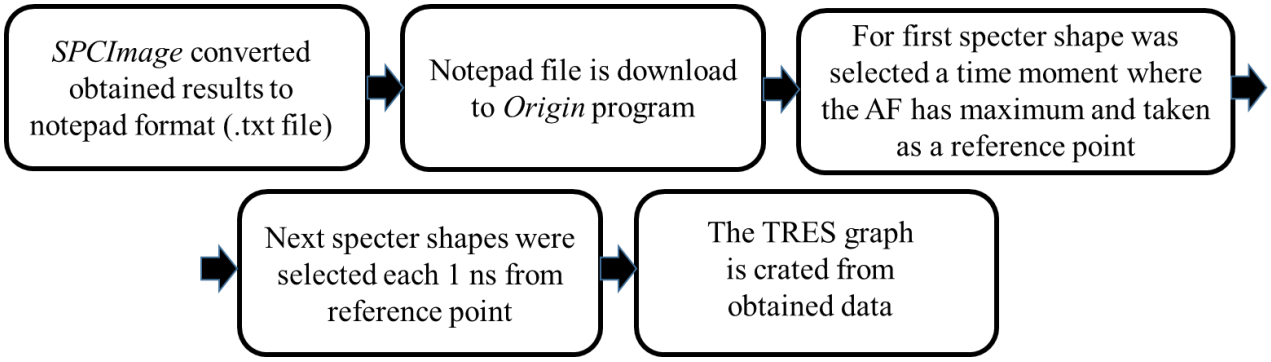

Results

1st trial

Before and after photobleaching the AF intensity kinetics was compared between healthy cells and melanoma cells. The concentration of the cells was 1mill/ mL. AF kinetic intensity was measured in spectral range 460 – 520 nm with 405 nm picosecond laser-impulse irradiation before and after photobleaching. Switching laser to continuous wavelength irradiation with power density ~ 40 mW/cm^2 resulted in photobleachong.

In spectral range 460-480 nm of healthy cells, corresponding to the spectral range of NADH emissions, AF intensity decrease was observed.

Table 7-1. Autofluorescence intensity decrease after photobleaching in percent (%) at each wavelength and emission kinetics at specific time moments. Healthy cells DC3F (He-68). N/O – not observed.

Time (ns) Wavelength (nm)	0	0,5	1	1,5	2	2,5
460	15±2	11±2	9±2	7±2	5±2	4±2
470	12±2	14±2	11±2	7±2	3±2	0±2
480	12±2	6±2	N/O	N/O	N/O	N/O
490	N/O	N/O	N/O	N/O	N/O	N/O
500	N/O	N/O	N/O	N/O	N/O	N/O
510	N/O	N/O	N/O	N/O	N/O	N/O
520	N/O	N/O	N/O	N/O	N/O	N/O

The total decrease in intensity after photobleaching is shown in Table 7-2.

Table 7-2. AF total intensity decrease after photobleaching at each wavelength. Healthy DC3F (He–68) cells.

Wavelength (nm)	%
460	10
470	9
480	2
490	0
500	0
510	0
520	0

Decreasing AF intensity of melanoma cells after photobleaching occurs within the standard deviation error (0±2%).

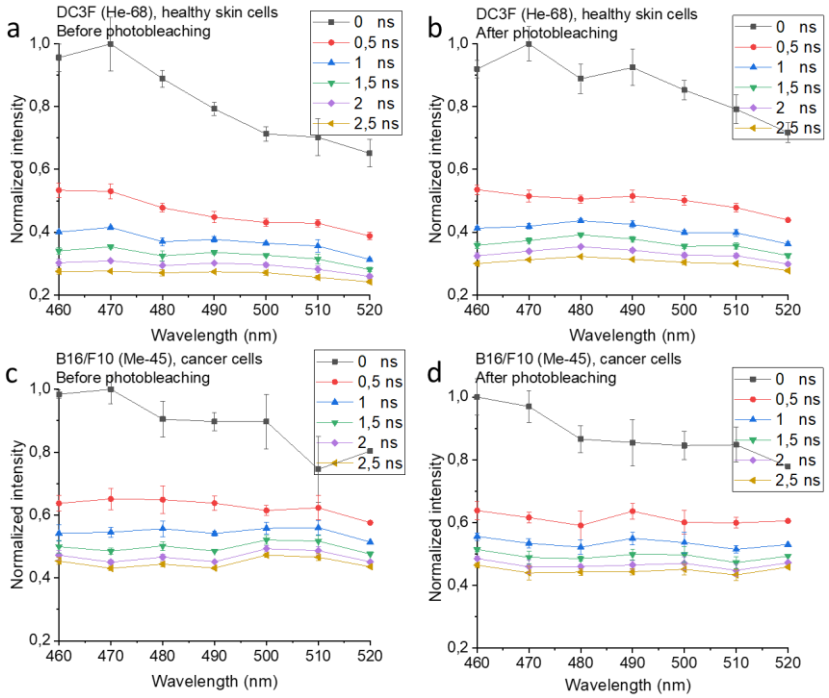

Fig.7-3. Time resolved emission spectra (TRES) of AF of healthy cells (a,b) and melanoma cells (c,d) before and after photobleaching. TRES of healthy cells before photobleaching (a), and after (b). TRES of melanoma cells before photobleaching (c), and after (d).

The spectroscopy graph with the time resolution is shown on fig. 7-3. Changes in the shapes of the spectra are within the error borders. The TRES analysis did not show the spectral changes after photobleaching (did not observe spectral maximum shift).

2nd trial

The aim: to compere TRES of healthy (DC3F (He-68)) and melanoma (B16/F10 (Me-45)) cells in spectral range 450 – 560 nm.

The second part of the measurements was performed in the 450 – 560 nm spectral range. Concentration of the cells increased to 6 mill / mL. The time resolution of the measurements was reduced in setup settings (from 0,05 ns till 0,19 ns). The measurement objective was to determine the distribution of fluorophores in cell cultures to determine to which fluorophores during measurements and data approximation should be focused.

The distribution of the AF intensity in time from 0 ns till 5 ns is shown on Fig. 7-4 (a, b). At the 1 ns, where NAD(P)H (450 – 490 nm) dominated, no changes were observed between two culture of cells.

Fig 7-4 (c, d) focuses attention on fluorescence kinetics in the time range of 0,5-5 ns. The fluorophores with longer duration of life are dominant in this time range. Figure 7-4(d) shows the spectral peak starting from 0,5 ns at 510 -520 nm, which demonstrates the dominance of the FAD fluorophore with a longer life, corresponding to literature sources [1,4]

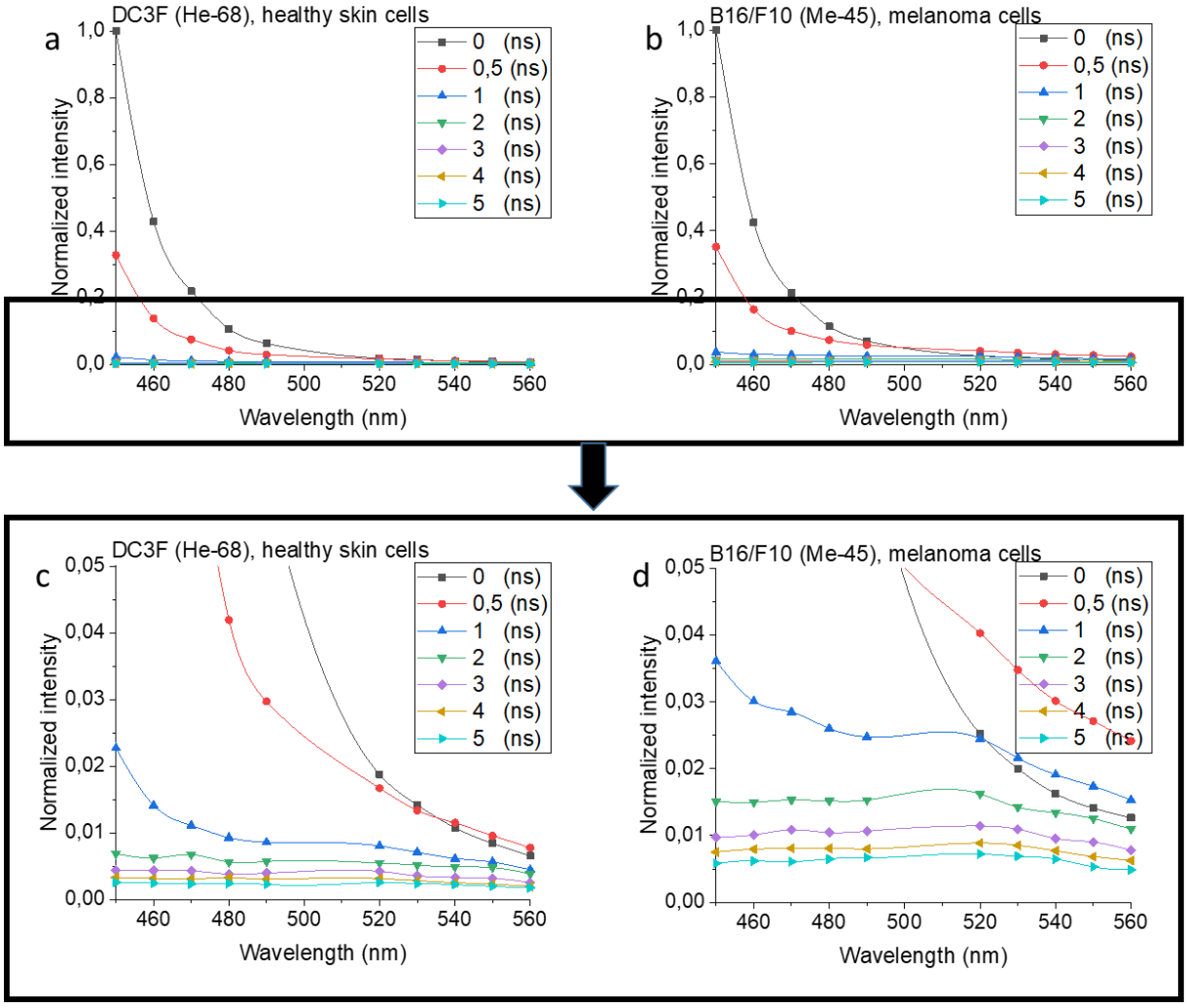

Fig.7-4. TRES of DC3F (He-68) and B16/F10 (Me-45) cells.

Conclusions

The first part of the measurements illustrated that in healthy cells, photobleaching influenced NAD(P)H fluorophores, but did not change the distribution of fluorophores.

The second part of measurements, the TRES analysis shows that after 5 ns, the kinetic fluorescence approaches 0 intensity value. The melanoma cell TRES analysis shows the peak in spectral range 510 – 520 nm in time range 0,5 – 5 ns (corresponding to the maximum FAD emission). From this it can be concluded that fluorophores with longer lifetimes of autofluorescence predominate in melanoma cell cultures.

During approximation, attention should be paid to the fluorophore of the FAD, which is longer life time of fluorescence.

References

[1] L. Marcu, P. M. W. French, D. S. Elson, Fluorescence lifitime spectroscopy and imaging, CRC Precc, 2015, pp. 47-85, 333.

[2] Cortassa, Aon, Marban, Winslow, O'Rourke, The CellML Project, [Online], https://models.cellml.org/exposure/e5ba9ba5ee28a2b107c2dd0f8343cea2/view.

[3] H.Stanley, J.Botas, V.Malhotra, "The mechanism of Golgi segregation during mitosis is cell type-specific," in Proc. Natl. Acad. Sci. U.S.A., 1997.

[4] B. Chance, B. Thorell, "Localization and kinetics of reduced pyridine nucleotide in living cells by microfluorometry," J Biol Chem., vol. Nov;234, pp. 3044-50, 1959.

[5] B. Chance, H. Sies, A. Boveris, "Hydroperoxide metabolism in mammalian organs," Physiol Rev, vol. Jul;59(3), pp. 527-605, 1979.

[6] K. Nakayama, T. Nakamura, M. Taniguchi, T. Tanaka, "Irreversible deacylation of plasma membrane phospholipids by the combined action of Mg2+ and a long-chain

acyl-CoA synthetase inhibitor in Saccharomyces cerevisiae," J Biosci Bioeng, vol. 94(3), pp. 258-63, 2002.
[7] H. Schneckenburger, K. Koenig, "Fluorescence decay kinetics and imaging of NAD(P)H and flavins as metabolic indicators," Opt. Eng., vol. 31, p. 1447–1451, 1992.
[8] L. Huang, CP. Kirschke, J. Gitschier, "Functional characterization of a novel mammalian zinc transporter, ZnT6," J Biol Chem, vol. 277(29), pp. 26389-95, 2002.
[9] K. Nakayama, T. Yamaguchi, T. Doi, Y. Usuki, M. Taniguchi, T. Tanaka, "Synergistic combination of direct plasma membrane damage and oxidative stress as a cause of antifungal activity of polyol macrolide antibiotic niphimycin," J Biosci Bioeng., vol. 94(3), pp. 207-11, 2002.
[10] D. N. Romashko, E. Marban, B. O'Rourke, "Subcellular metabolic transients and mitochondrial redox waves in heart cells," in Natl. Acad. Sci., USA., 1998.
[11] A. S. R.Koti, M. M. G.Krishna, N. Periasamy, "Time-Resolved Area-Normalized Emission Spectroscopy (TRANES): A Novel Method for Confirming Emission from Two Excited States," J. Phys. Chem., vol. 105, pp. 1767-1771, 2001.

Publicity of the results

Results of the A2.3 study were **reported** at the SPIE/BIOS conference "Multimodal Biomedical Imaging" in San Francisco, USA (February, 2020), at the 78th International conference of University of Latvia in Riga (February, 2020) and at the SPIE Europe conference (remotely, April 2020), and published in SCOPUS-cited conference proceedings:

1. J. Spigulis, I. Kuzmina, V. Lukinsone, M. Tamošiūnas, I. Oshina, L. Ozolina, A. Maslobojeva, M. Kuzminskis, D. Ivanov, E. Borisova, "Towards combined multispectral, FLIM and Raman imaging for skin diagnostics", *Proc.SPIE* **11232**, 112320N-1 (2020).

2. V. Lukinsone, I. Kuzmina, M. Tamosiunas, A. Maslobojeva, M. Kuzminskis, U. Rubins, J. Spigulis, "Remitted photon path length in human skin, skin phantoms and cell cultures," *Proc. SPIE* **11363**, Tissue Optics and Photonics, 1136320 (2 April 2020); doi: 10.1117/12.2555822

A2.4. *Elaboration of algorithms for mapping of particular skin fluorophores*

November 2019 – April 2020

The main contributors: Dr.phys. Vanesa Lukinsone and Dr.phys. Uldis Rubins

Algorithm for NADH and FAD extraction and mapping

The measurement set-up specifications for autofluorescences lifetime imaging are presented in the chapters of this report related to project activities A2.1 and A2.2. The measurements algorithm was built based on the NADH and FAD excitation and emission spectral bands. The excitation was performed with 405 nm picosecond pulse laser; emission for NADH is in the range 440 – 460 nm, for FAD – in the range 510 – 530 nm (report on A2.3). The wavelength 460 nm was used for data collection of NADH fluorophore autofluorescence, and 520 nm for FAD autofluorescence. The obtained images have been processed with two exponential approximations in *SPCImage* programme from B&H.

Image processing.

The principle of a TCSPC imaging system is illustrated in Fig. 8-1. A laser scanning device scans the sample with a focused beam of a high-repetition-rate pulsed laser. For every detected photon the detector sends an electrical pulse into the TCSPC module. From this pulse, the TCSPC module determines the time, *t*, of the photon within the laser pulse sequence (i.e. in the fluorescence decay). Moreover, the TCSPC module receives scan clock signals (pixel, line, and frame clock) from the scan controller of the device. The sequencer of the TCSPC module is configured as a scanning interface. It contains two counters, X,Y, for the x and y location in the scanning area. Synchronously with the scanning action, the sequencer counts through x and y [*W. Becker, The bh TCSPC Handbook, 8th edition, 2019*].

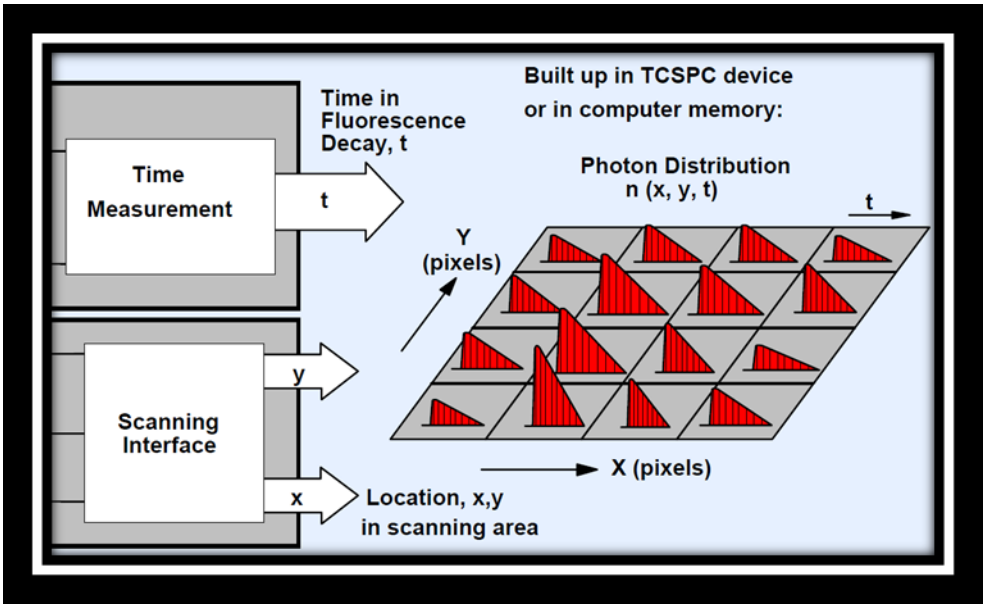

Fig.8-1. Multidimensional TCSPC architecture for fluorescence lifetime imaging.

***<u>The data collection and processing algorithm scheme</u>*.**

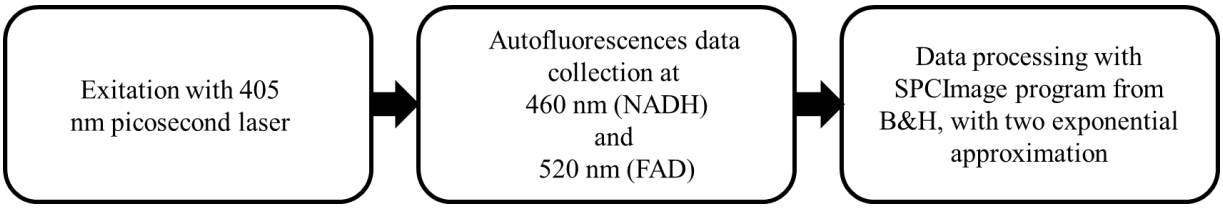

***Experimental validation of the algorithm*.**

The autofluorescences lifetime imaging measurements have been taken from ex-vivo skin samples comprising nevus, BCC and SCC. The obtained images are related to distribution of two decay rates corresponding to lifetimes τ_1 and τ_2. The data collected at 460 nm was associated with NADH and those at 520 nm - with FAD fluorophores.

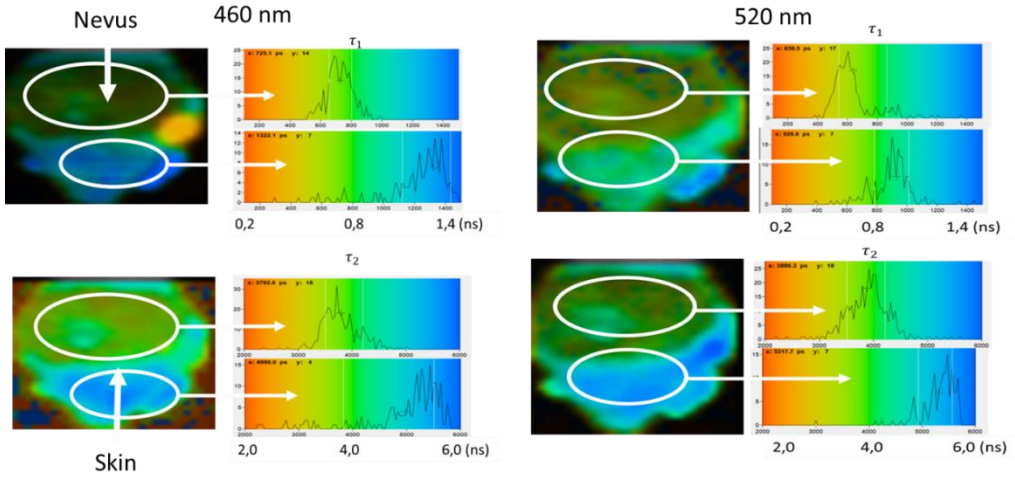

Fig. 8-2. The autofluorescences lifetime mapping of nevus with two exponential approximations (τ_1 and τ_2) at 460 nm and 520 nm.

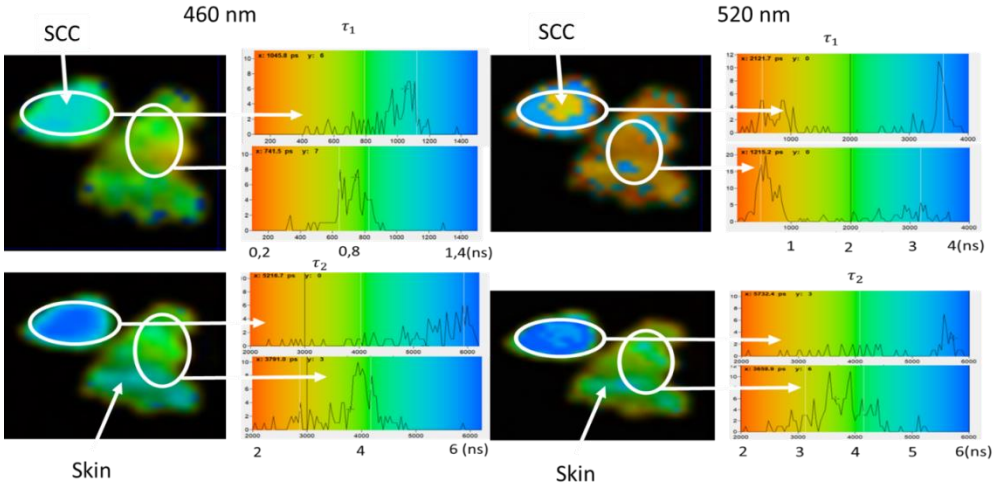

Fig.8-3. The autofluorescences lifetime mapping of SCC with two exponential approximations (τ_1 and τ_2) at 460 nm and 520 nm.

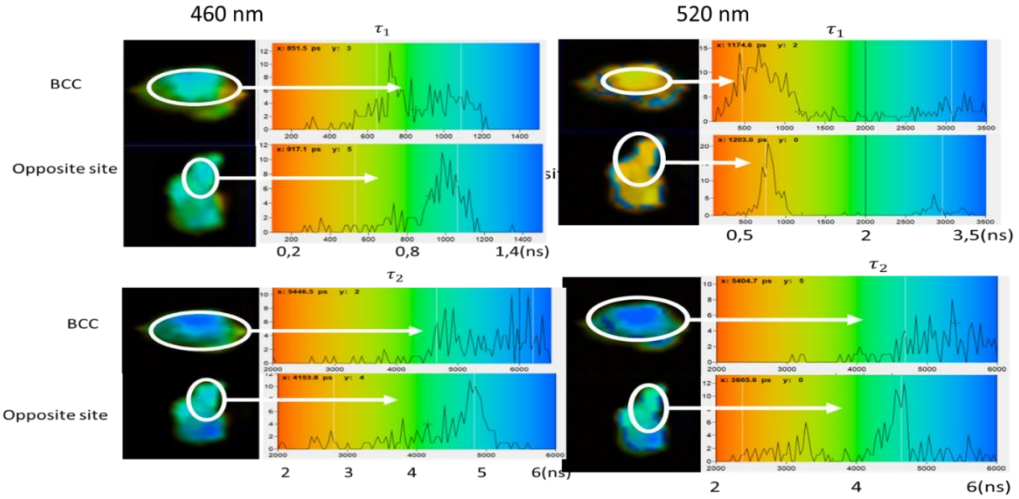

Fig.8-4. The autofluorescences lifetime mapping of BCC with two exponential approximations (τ_1 and τ_2) at 460 nm and 520 nm.

Table 8-1. The determined lifetime values for ex-vivo skin nevus, BCC and SCC at two detection wavelengths.

Life time (τ)	Detection wavelength 460 nm						Detection wavelength 520 nm					
	Nevus	Skin	SCC	Skin	BCC	Skin	Nevus	Skin	SCC	Skin	BCC	Skin
τ_1 (ns)	0,7-0,8	1,2-1,4	1-1,2	0,6-0,9	0,6-1,2	0,9-1,2	0,5-0,7	0,8-1	0,5-1; 3,5	0,5-1	0,5-1	0,5-1
τ_2 (ns)	3,5-4	5-6	5-6	3,5-4,5	4,5-6,5	4-5	**3,5-4,5**	**5-6**	**5,5-6**	**3,5-4,5**	**4,7-6**	**4-5**

The obtained results correlate with measurement data presented in the A2.3 report. For FAD fluorophores, the malignant tissues exhibit longer lifetime components if compared with the surrounding healthy skin. Consequently, this data processing algorithm allows detecting and mapping of malignant and healthy skin tissues.

A2.5. Clinical validation of the developed imaging technology: volunteer measurements

November 2019 – October 2020

The main contributors: Res.assist. Anna Berzina, Dr.phys. Vanesa Lukinsone, MSc student Anna Maslobojeva, MSc student Maris Kuzminskis

1. Statistics of the measured skin neoplasms

Clinical validation was performed in the University of Latvia (Riga, Latvia) from January to October 2020; preparations started in November 2019. Overall, **164 volunteers** have been involved. Volunteers with skin photo-types I, II or III (Fitzpatrick classification), aged between 12 and 88, were examined with their written consent under permission of the local Ethics Committee. The images of **292 different skin neoplasms** have been captured and **autofluorescence lifetime (AFLT)** signals have been measured on **44 of these malformations**. Table 9-1 provides detailed description of measured skin malformations. The measurements were taken accordingly to the protocols described A1.4.

The general procedure for measurements

1. A doctor explains to a patient the measurement procedure, an impact of the diagnostic device, as well as information in the patient consent form and patient rights.
2. The volunteer signs the patient consent form if he/she agrees to the procedure.
3. The doctor captures images of neoplasm(s) by a dermatoscope, puts markers near the neoplasm(s) that is (are) going to be captured with the devices and writes down the clinical diagnoses to each lesion.
4. Autofluorescences lifetime measurements are being performed according to the measurement protocol (see below).

Table 9-1. Statistics of the autofluorescences lifetime measured skin malformation from January to October 2020

Diagnosis	Number
Benign	
Junctional nevus	2
Combined nevus	17
Dermal nevus	12
Seborrheic keratosis	7
Haemangioma	4
Other	1
Malignant	
Malignant melanoma	
Basal Cell Carcinoma	1
Other	
Total	**44**

2. Autofluorescences lifetime measurements

The time-correlated single photon counting method was used for autofluorescences lifetime measurements; the equipment was described in the A2.2 and A2.3 sections.

In-vivo malformation clinical measurements were recorded at two/three spectral wavelength focusing to NAD(P)H 460 nm and FAD 520 nm and 530 nm fluorophores with irradiation 405 nm; the mesurements process and method was described in the A2.3 section. The autofluorescences lifetime imaging system A2.2. and A2.4. was tested ex-vivo and show applied method for in-vivo, during the clinical test

problems emerged with image stabilization and time for measurement. The clinical measurements proceed with singe point method by reason of image stabilization and measurement time.

The protocol for autofluorescences lifetime measurements

5. Measurements by AFLT system are taken as follows:
   a. Switch on the computer
   b. Open software SPCM (Becker&Hickl GmbH)
   c. Switch on laser
   d. Locate probe on patient malformation or skin
6. During the procedure, the patient is questioned if everything is all right and whether the patient feels comfortable.
7. After the measurement, the patient gets dressed, and, if patient has any additional questions, they are addressed accordingly.
8. The measurement is finished; the probe is being cleaned with a disinfectant wipe.

Results.

Measurements were taken from malformation at different body locations. The obtained signal was approximated by two exponential approximations. The results are presented in tables 9-2; 9-3; 9-4.

Table 9-2. The fluorescences lifetime of in-vivo **combined nevus**

Combined nevus	460 nm	520 nm	530 nm
τ_1	0,4±0,05	0,4±0,1	0,40±0,2
τ_2	3,8±0,1	**3,9**±0,4	**3,2**±0,3

Table 9-3. The fluorescences lifetime of in-vivo **dermal nevus**

Dermal nevus	460 nm	520 nm	530 nm
τ_1	0,5±0,1	0,5±0,1	0,4±0,05
τ_2	3,6±0,2	**3,4**±0,3	**3,2**±0,1

Table 9-4. The fluorescences lifetime of in-vivo **BCC**

BCC*	460 nm	520 nm
τ_1	0,4	0,6
τ_2	4,3	**5,0**

*BCC – only one case.

The main results show second exponent at 520 nm wavelength detection. The fluorescence at 520 nm with irradiation 405 nm correspond FAD fluorophore [1, 2, 3].

The fluorescence lifetime of malignant malformation appears significantly longer [1, 4] than that of benign malformation. More measurements are needed for reliable confirmation. The fluorescence lifetime result of malignant malformation was expected; similar results were obtained from ex-vivo measurements in A2.4 and for comparison are presented in Figure 9-1.

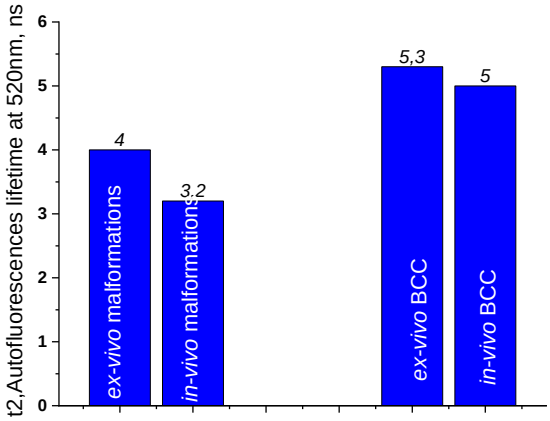

Fig. 9-1. The autofluorescences second component (τ_2) lifetime at 520 nm wavelength detection with irradiation 405 nm.

Conclusions

The *in-vivo* fluorescences lifetime measurements give promising results for diagnostics. The fluorescence signal at 520 nm with irradiation 405 nm, was approximated with two exponential approximation. In particular, the second component of fluorescence lifetime which correspond to FAD fluorophores show significant changes compare benign and malignant malformations (Fig 9-1). The FAD fluorescence lifetime longer component τ_2 for benign malformation is 3,5 – 4,5 ns and malignant 4,7 – 6 ns (tab. 8-1; 9-2; 9-3; 9-4, fig. 9-1). Measurements will continue during this project, imaging stabilization and time system, as well combined and compared with Raman spectroscopy.

[1] L. Marcu, P. M. W. French, D. S. Elson, Fluorescence lifitime spectroscopy and imaging, CRC Precc, 2015, pp. 47–85, 333.
[2] K. Konig, I. Riemann, “High-resolution multiphoton tomography of human skin with subcellular spatial resolution and picosecond time resolution,” J. Biom. Opt, vol. 8, pp. 432–439, 2003.
[3] D. Chorvat Jr. and A. Chorvatova, “Multi-wavelength fluorescence lifetime spectroscopy: a new approach to the study of endogenous fluorescence in living cells and tissues,” Laser Phys. Lett., vol. 6, 2008
[4] P. P. Provenzano, D. R. Inman, K. W. Eliceiri, J. G. Knittel, L. Yan, C. T. Rueden, J. G. White and P. J. Keely, Collagen density promotes mammary tumor initiation and progression, BMC Medicine, 2008.

A3.1. *Assembling and testing the equipment for single-point acquisition of skin Raman spectra*

May – October 2019

The main contributors: Dr.phys. Mindaugas Tamosiunas and PhD student Martins Osis

Report on the Raman spectroscopy measurement equipment test results

The aim of project activity A3.1 was to develop Raman point–spectroscopy system to measure spectra from cells and biological tissues. The system for single-point Raman spectra acquisition was built around iHR320 (Horiba, Japan) spectrophotometer with filtered NIR laser excitation (Cobolt 08-NLD, 785 nm, line width 200 pm) and fiber bundle probe supplemented with 785 nm low pass filter and dichroic mirror (Edmund Optics) for Raman Stokes spectral band detection. This was further combined with illumination and collection optics as indicated in Fig. 10-1.

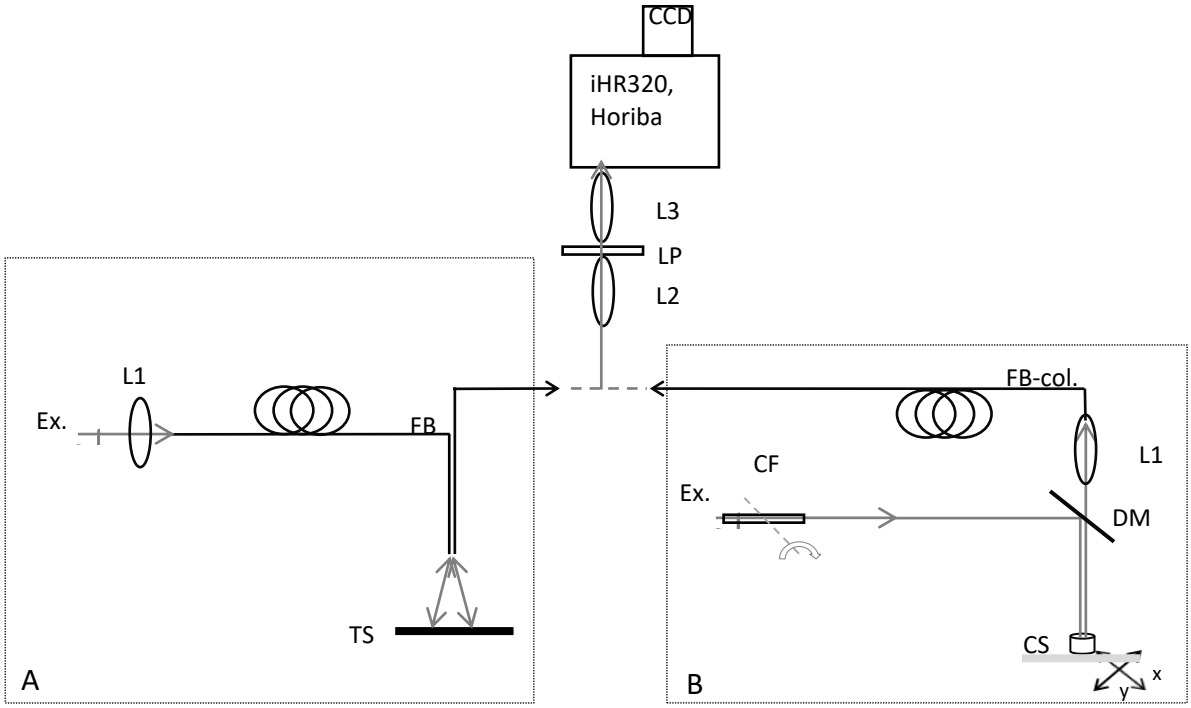

Fig. 10-1. Typical set-up for *in vivo* – A, and *in vitro* (or *ex vivo*) – B acquisition of Raman spectra. Required components: Ex. – NIR laser; L1 – fibre coupling lens; L2, L3 – collimating lenses; CF – laser clean-up filter; CS – cell sample container; LP – long pass filter; DM – dichroic mirror; FB – fibre bundle; TS – tissue sample; xy – translational stage.

The successful realization of Raman spectroscopy set-up (both *in vitro* and *in vivo*) was tightly bound to the optimization of instrumentation parameters, carefully done during M1 to M6 project implementation period. To test the assembled instrumentation, most common parameters related to entrance slit width, number of pixels for vertical (or horizontal) binning, grating-type, excitation power and averaging selection were adjusted with the reference to literature data. In overall, these parameters can be interdependent and heavily influence the final result of spectral resolution, SNR and spectra acquisition time. For example, one of the most important characteristics of a spectrometer is the spectral resolution ($\delta\lambda$). There are 3 main factors that determine the spectral resolution of a spectrometer: i) the slit width; ii) the diffraction grating; iii) the detector. The optimal slit width for our instrumentation set-up was determined by using Bayer aspirin powder for the reference (also with other Raman active materials, such as ethanol, methanol). As indicated in Fig.7-2, for 747 cm^{-1} Raman band (aspirin), 50μm slit width (W_s) was considered as optimal, resulting $\delta\lambda$ = 0,75 nm, calculated as $\partial\lambda = \frac{RF * \Delta\lambda * W_s}{n * W_p}$, where the spectral range of the spectrometer $\Delta\lambda$ = 269 nm (for 300 gr/mm grating), the detector pixel width (W_p= 26 μm), and the number of pixels in

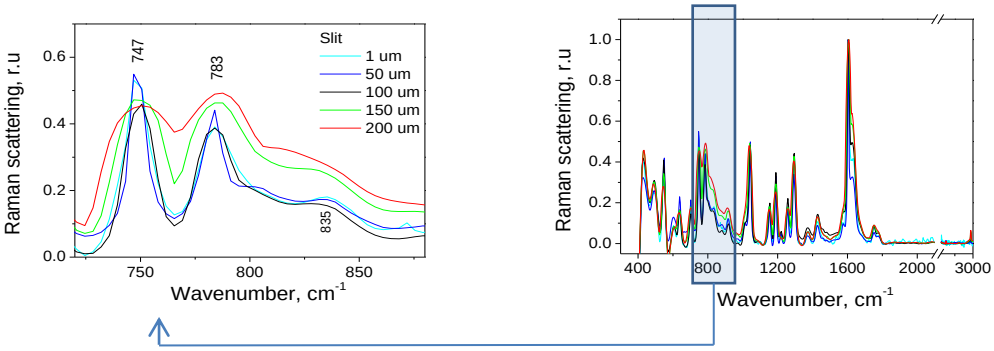

Fig. 10-2. Optimization of the slit width for Raman spectral measurements. Raman spectra of aspirin measured with 300 gr./mm grating; accumulation time 5 s, averaging 10, vertical binning 256 pixels.

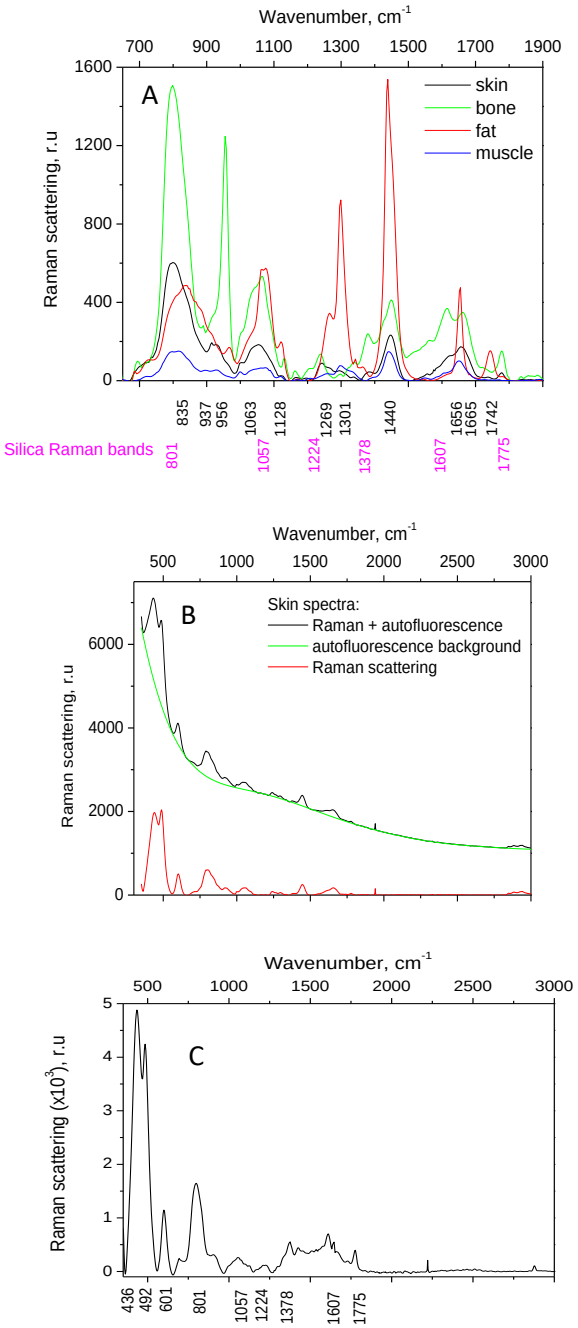

Fig 10-3. A) Ex vivo Raman spectra of skin, bone, fat and muscle tissues. B) Spectral data processing (autofluorescence subtraction). C) Raman spectra of silica fiber currently attached to the Horiba iHR320 spectrograph.

the detector (n=1024); for $W_s > 4W_p$, RF ≈ 1,5. For 600 gr/mm and 1200 gr/mm gratings, the spectral range Δλ do not cover the desired 300 – 3000 cm^{-1} scale for biological sample investigation, thus the grating is rotated automatically. This prolongsthe total accumulation time of a single Raman spectrum. Raman scattering is usually low in intensity (only ~1 out of 10^7 photons may undergo inelastic scattering) thus to avoid further increase of the accumulation time we probed few more options to improve the SNR: i) increase the light source output; ii) apply binning. Applying high averages also improved SNR, as indicated in Table 1. Thus, by applying N-averaging, our estimated optimal single spectrum acquisition time (10 to 90 s) ends up being multiplied by N-times. The resulting time period for the biological tissue measurements is acceptable for *ex vivo* specimens but still it could be considered long for *in vivo* patient use.

Four exemplary Raman spectra *ex vivo* of skin, bone, muscle and lipid-rich biological tissues are shown in Fig.10-3a. The bone tissue has unique Raman Stokes band signature at 956 cm^{-1} ascribed to symmetric stretching of tetrahedral P–O bonds in phosphate $(PO_4)^{3-}$ group [1]. Few other Raman spectral bands detected *ex vivo* have relatively high intensities (that can differ from strong autofluorescence background of biological tissues, subtracted as shown in Fig. 10-3b): lipid specific

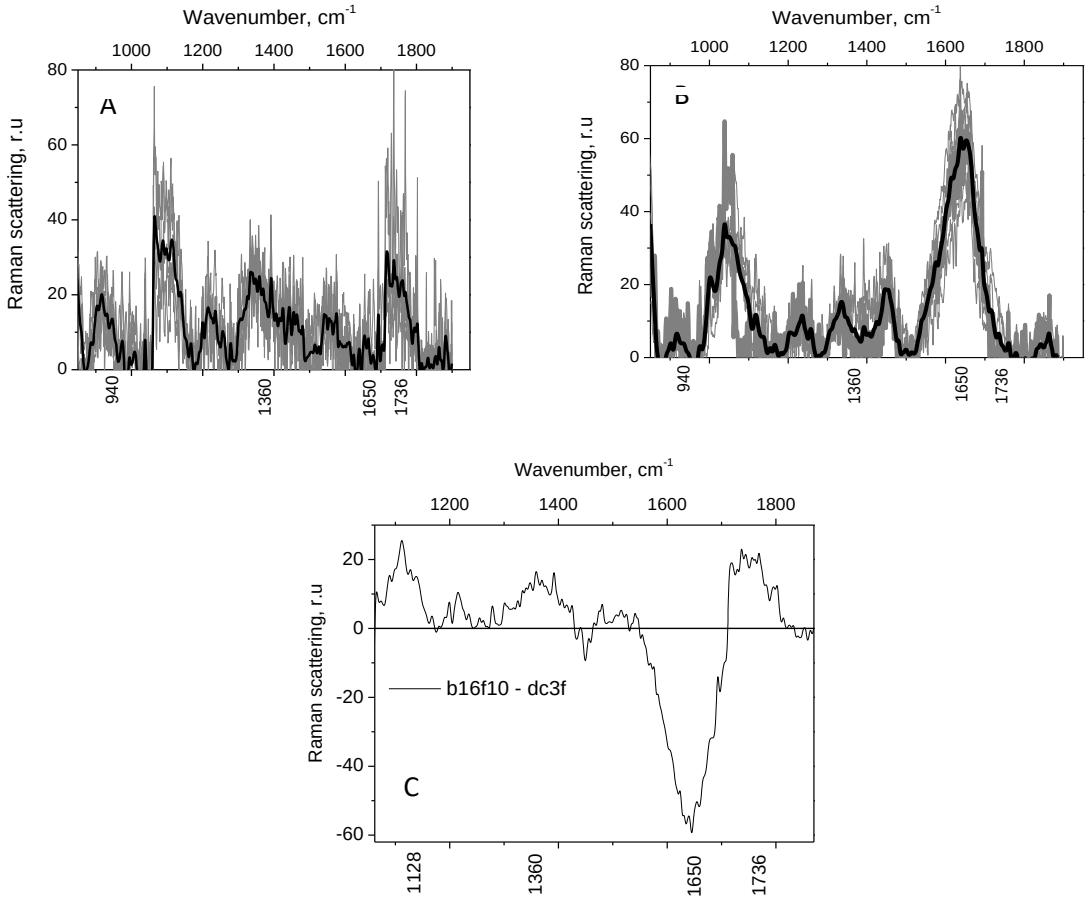

Fig.10-4. *In vitro* Raman spectra of melanoma b16-f10 cells (A) and dc-3f cells (B). Bold lines indicate the average spectral values. Result of average spectra subtraction (b16f10 - dc3f) is shown in C. Single spectra aquisition time 90s; 50 μm slit; 1200gr/mm grating;256 pixels vertical binning. During the measurement cells were resuspended in 1X PBS.

band around 1440 cm^{-1}, assigned to triolein and ceramide H–C–H bending; ceramide lipid C–C symmetric (or asymmetric) skeletal stretching at 1128 (or 1063) cm^{-1}; H–C–H twisting and wagging modes in lipids at 1301 cm^{-1} and C=C stretching in lipids at 1656 cm^{-1}. The former mentioned lipids (triolein and ceramide) are also the major components of skin epidermal surface. Ceramide comprises half of the lipids in *stratum corneum* and triolein is found within the sebaceous glands [2]. As seen from Fig. 10-3a, skin spectra possess some similarity with fat and muscle spectra, but some specific spectral features of skin can arise from C–C stretching of proline (and valine) amino acids at 937 cm^{-1} from keratin; also from collagen and elastin

backbone C–C stretching at 940 cm^{-1}. Also from amide-III specific band contribution around 1269 cm^{-1} which is assigned to α-helix conformation, C–N stretching, N–H (in plane) bending specific to collagen, elastin and keratin. In proteins, C–O stretching mode of amide-I contributes to Raman signal at 1653 cm^{-1}. The characteristic peak of cell nucleus at 835 cm^{-1} is assigned to O–P–O symmetric stretching vibration of the DNA backbone and tyrosine.

The plot Fig.10-3c also allows comparing Raman spectra of biological tissues *ex vivo* with area normalized Raman spectra of silica fiber. Major peak similarities were found at 801, 1057, 1224, 1378, 1607 and 1775 cm^{-1}, which means that these distinct spectral bands correspond to Raman spectra of silica. For Raman spectroscopy applications *in vitro,* we successfully removed silica fiber background by using set-up depicted in Fig. 10-1b.

We measured Raman spectra *in vitro* from b16-f10 (melanoma) and dc-3f murine cells suspended at 6×10^7 u./ml concentration in PBS (pH=7,1). The cell sample volume (V = 50 μl) was placed into a cylinder shaped and bottom flat container (h = 3mm; r = 2,5 mm) tightly covered with 24" gold folia. Gold itself is not Raman active therefore, what we measured was the Raman signal of cell sample alone.

Fig.10-4 shows the mean averaged Raman spectra *in vitro*. Melanin bands peaking around 1360 – 1400 cm^{-1} allowed discriminating b16-f10 melanoma cells from dc-3f cells. Apart from pigmentation criteria, amide-I band intensity at 1650 cm^{-1} was decreased and lipid specific band intensity at 1736 cm^{-1}, assigned to C–O stretch vibrations, was increased in b16-f10 melanoma cells.

In-vivo Raman spectroscopy measurements are most commonly performed by using fiber optic probes being in contact with the skin. With respect to exposure time range of 10 to 10^3 s, the equation

$$\frac{P}{S} = 2 * 10^3 * 10^{0.002(\lambda-700)} \left[\frac{W}{cm^2}\right] \qquad (3)$$

was used for the maximum allowed light source (λ=785 nm) output power calculation [3], yielding maximal 296 $\left[\frac{mW}{cm^2}\right]$ fluence rate for *in vivo* Raman applications. Due to P = 500 mW output power, our excitation fiber (NA = 0,22) was positioned at 3,2 cm distance from the human volunteer skin surface, producing S = 1.7 cm^2 illumination area for Raman spectra acquisition (Fig. 10-1a).

Raman data *in vivo* comprise two different types of spectra – measured from normal skin and pigmented nevus. At Raman shifts of 900 – 1575 cm^{-1} the average signal of skin was ~1.6 times lower than the nevus. Fig. 10-5 depicts area normalized Raman spectra of skin and nevus allowing spectral shape comparison. Both skin and nevus spectra are characterized by the most intense Raman band peaking at 1443 cm^{-1}. This broadband signal represents overlapping bands of collagen, elastin and keratin (1450, 1454 cm^{-1}) and lipids (1440 cm^{-1}). Skin and nevus spectra also show increased intensity at 1301 cm^{-1} and 1080 cm^{-1} reflecting C–H vibration modes in lipids. The presence of poorly developed peaks at 1248 cm^{-1} (or 1336 cm^{-1}, respectively) originates from tertiary amides in collagen/elastin or amino acid crosslinks (desmosine-isodesmosine) in elastin. Lower spectral intensity bands at 937 cm^{-1} and 940 cm^{-1} characterize C–C

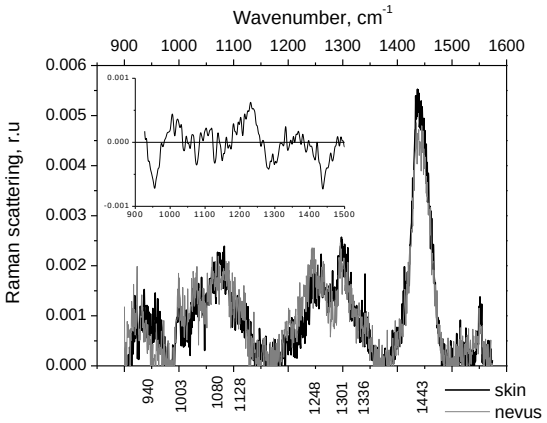

Fig. 10-5. Raman spectra of healthy skin and pigmented nevus (area normalized). The diference spectrum (nevus – skin) is shown in the insert. Human tissues were exposed to 27 J/cm^2 fluency per single measurement (P=300 mW/cm^2, collection time 90 s). 220 pixel vertical binnig was found optimal for *in vivo* spectra aquisition.

stretching vibrations in keratin and in collagen/elastin helical structure. Low intensity band at 1128 cm^{-1} characterizes the symmetrical C–C stretching in ceramide.

Spectra of healthy pigmented nevus were mostly identical to normal skin, except the relative increase of tertiary amide band intensity and decreased signal from keratin at lower wavenumbers (Fig.10-5 insert).

In **conclusion,** our test results show a promising opportunity for the assembled Raman spectroscopy set-up to differentiate between normal and cancerous cells providing metrics related to cell molecular composition.

A3.2. Development of a system for imaging of selected Raman spectral bands

November 2019 – July 2020

The main contributors: Dr.phys. Mindaugas Tamosiunas, PhD student Martins Osis

System for imaging of selected Raman bands

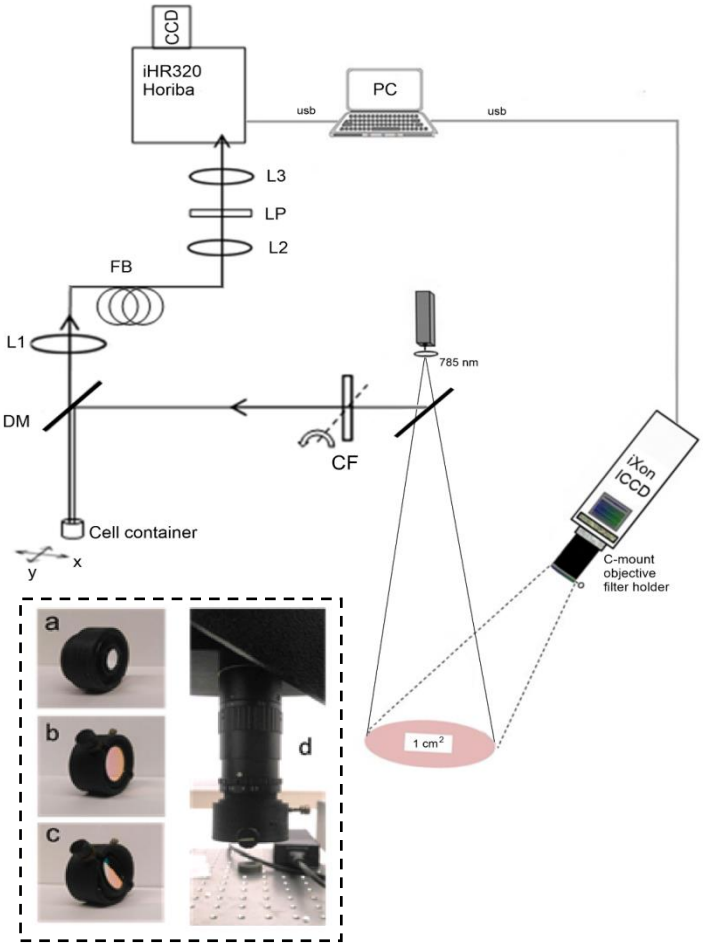

Figure 11-1. Combined set-up for acquisition of Raman macro images and spectra. Intensified CCD camera (iXon Ultra 888, Andor) records Raman images through the set of optical filters embedded into the filter holder, including 785 nm laser rejection filter (a) and rotated band pass filter positioned at 0 degrees(b) or at 5 degrees (c) perpendicular to the optical axis, mounted on Macro lens 35mm Focal Length,1.1" Sensor, f/2.8 - f/16 aperture objective (d). Additional components: CF – laser clean-up filter; DM – dichroic mirror; L1 – fiber coupling lens; L2, L3 – collimating lenses; FB – fiber bundle; LP – long pass filter (OD785 nm >6); xy – translational stage.

For Activity A3.2, we developed Raman spectral band imaging set-up to visualize the selected Raman bands from excised human tissues *ex vivo*. The first imaging approach included the acquisition of Raman spectral data cube combining sample point-scanning (in x-y directions) and Raman spectra measurement (λ). Fifteen human tissue samples classified histologically as seborrhea keratosis, nevi and basal cell carcinoma were investigated. The excised lesions were mounted on two-dimensional micrometer stage to allow the controlled positioning of the excitation beam. As indicated in Figure 11-1, Raman spectra were recorded by iHR320 imaging spectrometer equipped with 1200 g/mm grating and thermoelectrically cooled Syncerity-CCD camera (Horiba, Japan). A 785 nm diode laser (40 mW per 0.14 cm^2 area) was used for excitation, and the dichroic filter served to reflect the light onto the sample and also to transmit the Raman signal. Fiber optics, used together with the filter set were used for Raman spectra collection additionally filtering out the remaining excitation light and Raman bands of fiber silica.

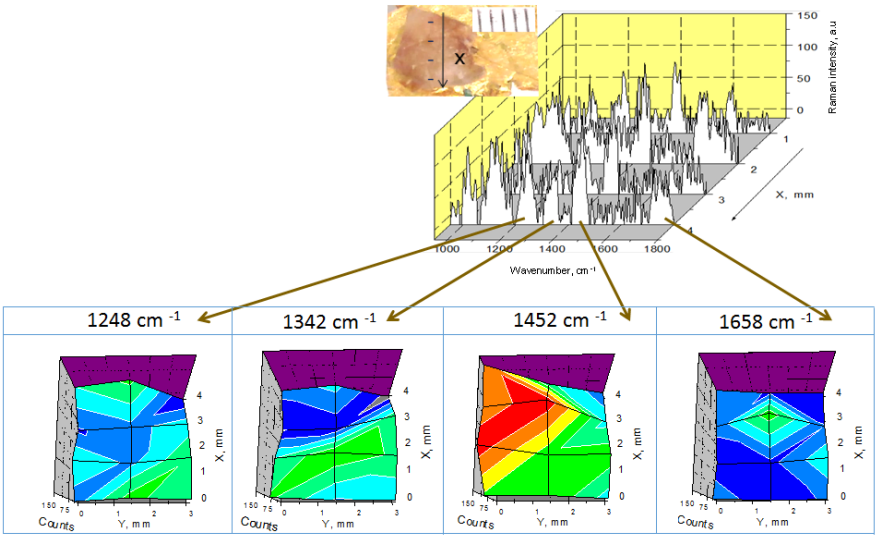

Figure 11-2. Representative Raman images of seborrheic keratosis sample (ex vivo) generated by raster scanning profile.

Representative image, Fig. 11-2, depicts the results of seborrheic keratosis tissue in the spectral range of 900 – 1800 cm^{-1}. The bands at 1658, 1450, 1342 and 1248 cm^{-1} were selected to represent the Raman peak intensity variations within the sample area. All spectral band images have millimeter scale resolution, as 2 x 2 mm area was illuminated for raster scanning.

Although point-spectroscopy method can be used *ex vivo* for identification of tissue histological type, the raster scanning cannot be applied easily for examination of large sample area due to several limiting factors. For 1200 gr/mm grating, the spectral range Δλ=61 nm would not fully cover the desired 300 – 3000 cm^{-1} wavenumber scale, thus the iHR320 grating has to be rotated automatically 5 times. This prolongs the total accumulation time of a single Raman spectrum. Raman scattering is usually low in intensity (only ~1 out of 10^7 photons may undergo inelastic scattering) thus to avoid further increase of the accumulation time more options are available to improve the SNR: i) increase the fluence rate; ii) apply binning; iii) apply averaging.

To protect the skin of human patients, the permitted fluence rate calculated [3], defined as:

$$Fluence\,rate = 2 \cdot 10^3 \cdot C_4 = 0.296 \quad [\frac{W}{m^2}] \qquad (1)$$

$$C_4 = 10^{0.002(\lambda - 700)} = 10^{0.17} = 1.479 \qquad (2)$$

The time period of 10 to 90 s for single spectra acquisition results 3 to 27 J/cm^2 light fluency delivered in situ per single spectra acquisition, even for N=1. By applying N-averaging, the single spectrum accumulation time (and fluency) ends up being multiplied by 5xN times. The total fluency transmitted to the biological tissue becomes even higher when multiple spectra are measured within the same sample. These issues indicate that Raman spectroscopy technique is not practical enough in combination with large FoV point-by-point scanning applications. To summarize, it is a time consuming process to scan a 1 cm^2 area (and above). Second, the biological tissues cannot be exposed to high levels of fluency due to dehydration of

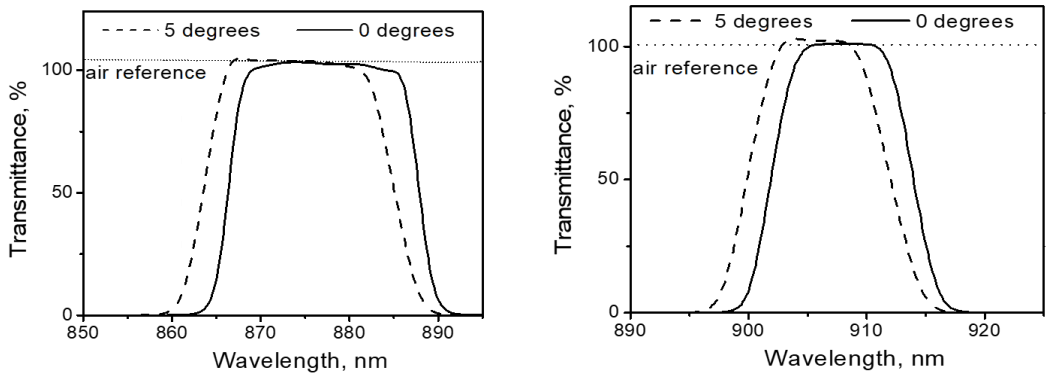

Figure 11-3. Filter FF01-880/11-25 (#1) and FF01-910/5-25 (#2) transmittance at 0 degrees or at 5 degrees pivot rotation angle. Transmittance measurements have been taken by using Beckman Coulter DU800 spectrometer.

Table 11-1. Spectral regions for Raman band imaging at 90% filter transmittance level.

#	Filter name	Transmittance band > 90% (nm)	Center wavelength (nm)	Transmittance spectral region **at 0 degrees,**(cm^{-1})	Transmittance spectral region **at 5 degrees** (cm^{-1})
1.	FF01-880/11-25	874.5 – 885.5	880	1217 – 1456	1185 – 1409
2.	FF01-910/5-25	903.8 – 912.1	908	1674 – 1775	1651 – 1747

the tissue, denaturation of proteins, and destruction of other biomolecules. Third, the constructed image will have low spatial resolution.

As alternative for Raman spectral imaging, we used a non-scanning, large area macro imaging method, based on tunable band pass filter application. Previously, such diagnostic method has been reported to detect microscopic bone like structures within the soft tissue [4]. The differentiation between muscle and bone has been achieved due to the unique Raman Stokes band signature at 956 cm^{-1} ascribed to symmetric stretching of tetrahedral P–O bonds in phosphate $(PO_4)^{3-}$ group. We built the imaging system (Figure 11-1) comprising intensified CCD camera (iXon Ultra 888, Andor Technology, UK), 785 nm excitation notch filter (NF03-785E-25, Semrock, USA) and a set of Semrock (USA) narrow-band optical filters attached to macro lens (35mm focal length, f/2.8 - f/16, Edmund Optics, USA). For selected Raman band of interest, the macro-imaging of $1cm^2$ sample area was performed. As indicated in Figure 11-3, angular tilt of tunable narrow-band Semrock filter by 5 degrees, FF01-880/11-25 (filter #1) or FF01-910/5-25 (filter #2) produced ~3 nm anti-Stokes shift at 90% of transmittance level. The final image of Raman scattered light was computed by subtracting two images transmitted at peak different wavenumbers, thereby removing the background autofluorescence of the sample. The pseudo coloring technique was applied to create the contrast maps corresponding to the spatial location of Raman spectral band of interest.

Validation data of the Raman imaging system

To test Raman macro imaging method *ex vivo*, 5 samples stored in formalin, including SCC, BCC, nevus, fat and skin were measured. As indicated in Table 11-1, angular adjustment of band pass filter #1 shifted the filter transmittance from 1456 – 1217 cm^{-1} to 1409-1185 cm^{-1} wavenumber range. Figure 11-4 show representative Raman images of healthy skin, bordering fat tissue and nevus ex vivo. Raman spectra of skin are composed of vibrational modes of proteins, amino acids and lipids [5]. At 0 deg. filter #1 rotation, Raman images comprise the intense band near 1450 cm^{-1} originating from epidermal keratin, dermal collagen and lipids (ceramide and triolein). At 5 deg. filter rotation, only low intensity bands peaking at 1248, 1271, 1301, 1342 cm^{-1} contribute to the Raman image of skin. These band assignments are indicated in Table 11-2.

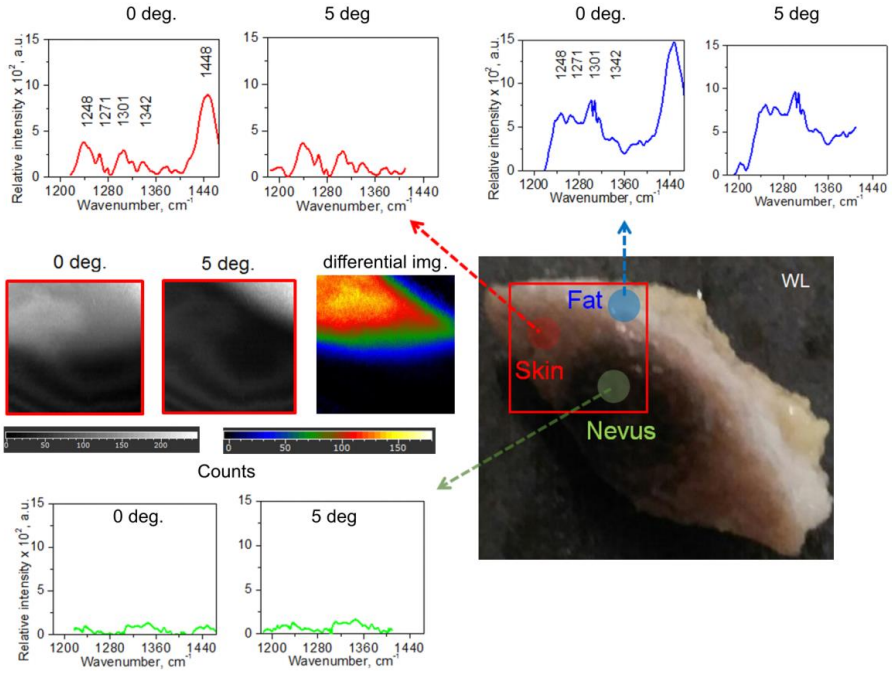

Figure 11-4. Representative image of skin, fat and nevus tissue depicted in white light (WL) and Raman signals at 0 degrees and 5 degrees pivot filter #1 (FF01-880/11-25) rotation. Fat locations show significant signal while the Raman signal of nevus is suppressed and merged with the background at both transmittance angles. The spectra of skin, fat and nevus is shown in relative numbers corresponding to >90% filter (#1) transmittance region. Spectral signatures serve as a proof for the obtained Raman spectral band imaging results. Only the signal of the skin at 5 deg. filter rotation is much weaker as compared to the signal at the filter normal position (0 degrees). The differential image was calculated by subtracting images "5 deg." from "0 deg." Thereffore by subtraction of the images, a resulting differential image shows only the difference from the skin Raman emission.

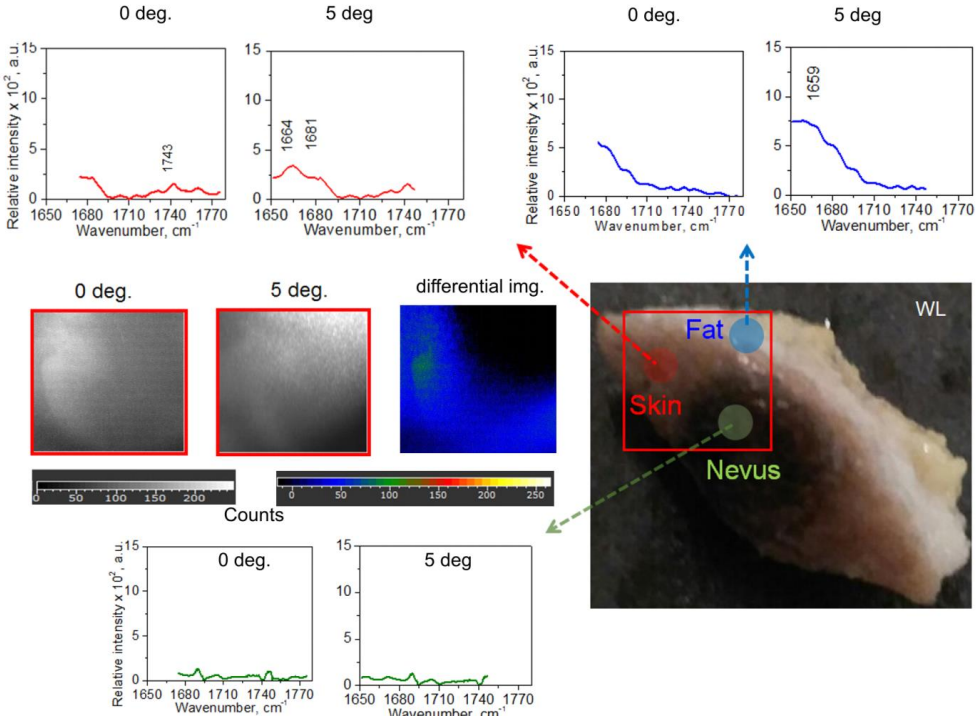

Figure 11-5. Representative image of skin, fat and nevus tissue depicted in white light (WL) and Raman signals at 0 degrees and 5 degrees pivot filter #2 (FF01-910/5-25) rotation. Fat locations show significant signal while the Raman signal of nevus is suppressed and merged with the background at both transmittance angles. The spectra of skin, fat and nevus is shown in relative numbers corresponding to >90% filter (#2) transmittance region. The subtracted differential image (5 deg. from 0 deg.) is also depicted in pseudo colors. To interpret the relative image intensity values, the regions of tissue morphology are co-localized with Raman spectral data.

Figure 11-5 displays the imaging results from the same sample, obtained by using filter #2 as Raman band differentiator. The filter positioning at 0 degrees (or at 5 degrees) allowed capturing Raman image at 1674 – 1775 cm^{-1} (or at 1651 - 1747 cm^{-1}) wavenumber interval. The most intense Raman peak near 1660

Table 11-2. Peak positions of the main Raman bands.

$\tilde{\nu}$, [1/cm]	**Peak assignments**
622	C-C twisting mode of phenylalanine
718	C-S stretching (protein); C-N stretching of choline (membrane phospholipid head—phospholipids); nucleic acids (adenine); CH_2 rocking
789	Thymine & cytosine phosphodiester: –O–P–O–N stretch; thymine/uracil C=O out-of-plane bending
801	Fiber silica
813	CCH bending (aliphatic) of proteins; C-C stretching (collagen); O-P-O phosphodiester stretching of nucleic acids; proline; hydroxyproline;
815/32/53	Tyrosine
939	C-C stretching of proline and valine and protein backbone;C-C stretching of protein backbone
1004	Phenylalanine
1016	Tryptophan
1028/34	Phospholipid & nucleic acid; PO_2- symmetric. stretch; C-N stretch -proteins, lipids; C-C skeletal stretching of proteins; C-H stretching/bending of phenylalanine; proline
1063	C-C asymmetric skeletal stretching of lipids (transconformation); PO_2 symmetric stretch of phospholipids; O-H bending (very weak); C-O and C-C stretching of glycogen; glutamine; proline
1127	C–C stretching (proteins); C–C stretching (lipids)
1209	Tyrosine, phenilalanine
1248	Amide III (β-sheet and random coil conformations)—C-N stretching and CH2 wagging; PO2 asymmetric stretching in nucleic acids; β sheet/ thymine/ cytosine (DNA base/ DNA & RNA base) nucleus;
1261	Pyrimidine ring stretching—thymine/uracil
1271	Amide III (α-helix conformation)—C-N stretching and N-H in-plane bending (proteins); =C−H ethylene deformations —cis conformation from unsaturated fatty acids (triolein and phospholipids);
1301	CH modes (CH_2 twisting and wagging) of lipids and collagen; =C−H bending (cis conformation) of lipids; Amide III mode (α-helix conformation)—C-N stretching and N-H in-plane bending (proteins)
1342	Amide III; CH vibrations (CH_2 and CH_3 wagging) of proteins; C-C stretching of aromatic ring (proteins); melanin (C-C stretching of aromatic ring and C-H bending—broadband); tryptophan; nucleic acids (guanine); actin
1360/1400	Melanin
1448	CH_2/CH_3 bands; C-H bending, stretching, scissoring, asymmetric deformations, lipids and proteins
1552/66	Tryptophan; amide II; C–C stretching and C–N–C bending/rocking—porphyrins
1647/54 1659/61	Amide I, C=C lipid stretch C=O stretching of amide I (α-helix, β-sheet and random coil conformations) of structural proteins; C=C alkyl stretching of lipids—cis conformation; C=C stretching of squalene (strong peak at 1670 cm^{-1}); nucleic acids; bending of H_2O
1743/56	Lipids, C=O stretch

cm^{-1} characterizes both skin and subcutaneous fat tissue. It is a Raman biomarker of ceramide and triolein, and originates from C=C stretching of primary amides. C-O vibration of primary amides in collagen and elastin also contribute Raman intensity at 1660 cm^{-1}. At 5 deg. filter #2 rotation, the decreased Raman intensity of skin was detected. This is a specific Raman signature of healthy skin, absent in lipid tissue, nevus and cancerous tissue.

In comparison to adjacent skin and subcutaneous fat tissue, Raman images of nevus collected by filters # 1 and # 2 show the decreased intensity (Figures 11-4 and 11-5). The mean Raman spectra of nevus, indicating low contribution of 1450 cm^{-1} and 1660 cm^{-1} spectral peaks to Raman images, are also included.

Figures 11-4 and 11-5 include differential Raman images. The differences of Raman intensity within 1456 – 1409 cm^{-1} wavenumber interval were revealed by using filter #1. By subtracting the resulting two images (5 deg. from 0 deg.) good differentiation between skin and nevus was achieved due to low Raman intensity from nevus, compared to high Raman intensity to localize the normal skin. The subtraction of images produced by filter #2 suppressed Raman signal at 1674 – 1747 cm^{-1} spectral region and contributed Raman map mainly from 1651 – 1674 cm^{-1} wavenumber range. By tuning the filter to 5 degrees, the intense fat signal was captured within the transmittance window, however the intense skin signal was left outside, contributing only from 1747 – 1775 cm^{-1} spectral region, characterized by Raman scattering of skin lipids.

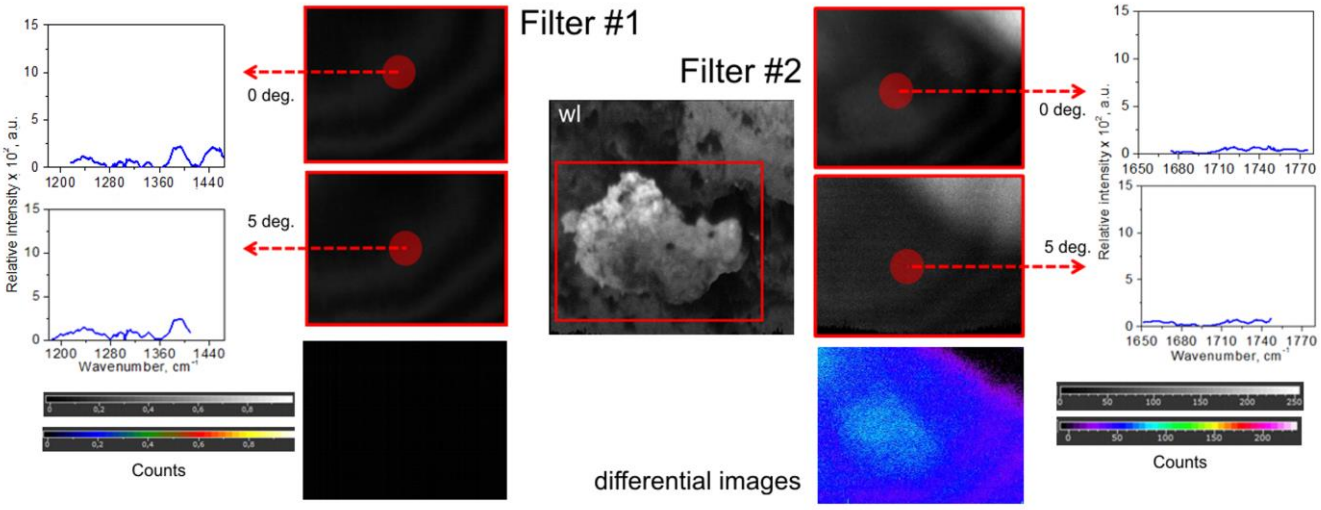

Figure 11-6. Representative image of BCC tumour in white light (WL) and Raman signals at 0 degrees and 5 degrees pivot filter #1 (FF01-880/11-25) and filter #2 (FF01-910/5-25) rotation. Raman signal from tumour is suppressed and merged with the background at both transmittance angles. Tuning the narrow-band filter #2, the heterogenous intensity from BCC is extracted from differential images. Above the backgroubdnoise of the tissue.

Further experiments conducted showed that Raman spectral band imaging pattern of BCC or SCC skin cancer can be more likely related to nevus than to normal skin. As observed in the images, the decrease of Raman band intensity near 1450 cm^{-1} and 1660 cm^{-1} is related to the appearance of BCC skin cancer (Figure 11-6). The images of SCC were also characterized by lower Raman scattering intensity within the filter #1 and #2 transmittance regions, both at 0 deg. and 5 deg. rotation (Figure 11-7). In line with previous studies, Raman signal reduction in BCC and SCC skin cancer indicate lower amount of collagen and triolein *in situ* [6]. Tumour-secreted metalloproteinases induce the degradation of collagen and prohibit pro-collagen biosynthesis. Less triolein could be due to lowering of subcutaneous volume of fat during the lesion formation. Our data show that decrease in 1450 and 1660 cm^{-1} Raman peak intensity (dominated by proteins and lipids) occurs with the appearance of tissue malignant transformation, independently of the tissue type (BCC or SCC) investigated.

In conclusion, the strength of Raman macro imaging is that it can provide a wide field of view (cm2), fast acquisition (10 seconds/image) and safe imaging conditions (< 300 mW/cm^2 fluence rate) that make it

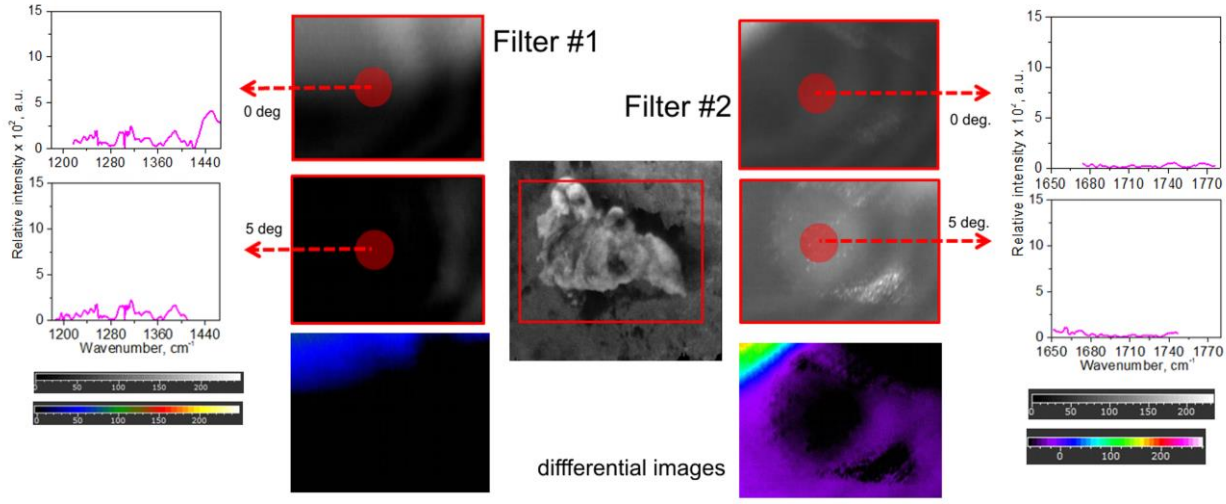

Figure 11-7. Representative image of SCC tumour in white light (WL) and Raman signals at 0 degrees and 5 degrees pivot filter #1 (FF01-880/11-25) and filter #2 (FF01-910/5-25) rotation.Raman signal from tumour is suppressed and merged with the background at both transmittance angles for filter #1. Tuning the narrow-band filter #2, the differential Raman intensity from SCC tumour is below the background signal of the tissue

ideal for clinical application (Table 11-3). However, more testing is necessary to demonstrate the reliability of this method for tumour diagnosis.

Within the next step of ERDF project (in particular, activity A4) autofluorescence lifetime and Raman band bi-modal imaging modalities will be combined to study challenges for further improvement of tumour diagnostic performance. New criteria for improved separation between BCC and SCC skin malformations will be sought by further development of technology for tri-modal skin imaging by combining autofluorescence life-time imaging, Raman spectral band imaging and a smartphone-based multispectral imaging device [7].

Table 11-3. Comparison of Raman imaging instrumentation approaches

Method	Advantages	Limitations
Point-by-point mapping	• High spectral resolution • Spectral coverage within 300 – 3000 cm-1 range • Hyperspectral data cube acquisition.	• Slow (limited by single spectra acquisition time which is ~2 min); • Laser induced sample damage (via light dose accumulation) ; • Low spatial resolution (single data point is 2x2 mm size for our set-up).
Spectral band imaging	• Highly efficient imaging: large areas (cm2 range) and fast acquisition (1 min/ whole image); • Diffraction limited spatial resolution; • Single photon sensitivity (by Andor iXon or iStar); • Optimized for NIR region (Andor iXon, QE at 920nm ~30%)	• Low spectral resolution • Raman band imaging selection depends on filter availability;

Publication:

J.Spigulis, V.Lukinsone, I.Oshina, E.Kviesis-Kipge, M.Tamosiunas, A.Lihachev, "Recent Results of Riga Group on Laser Applications for Skin Diagnostics", *J.Phys.:Conf. Series* (2020, accepted).

A3.3. Development of software for image acquisition and data processing

February – July 2020

The main contributors: Dr.phys. Mindaugas Tamosiunas, res. assist. Oskars Cizevskis

Seborrheic keratosis and nevi are among the benign skin lesions that can be visually misinterpreted as the skin cancer. Depending on patient data availability, Raman spectroscopy and imaging software was developed to classify these benign skin lesions, in particular aiming i) to distinguish between pigmented skin lesions (dermal, junctional or combined nevi); ii) distinguish seborrheic keratosis from other pigmented skin lesions. This is a different approach from some previous research that aimed to differentiate between skin cancer and benign skin lesions.

Data analysis unit (DAU) comprises personal computer with Python software configured to execute the method and algorithms for Raman spectroscopy data processing and to generate the tissue diagnostic metrics. The software instructions, that enable DAU processor to extract diagnostic metrics are written in Python programming language and are provided in a form of a program product.

The first step for processing Raman spectroscopy data is performed by *Labspec 6* software:

- to remove autofluorescence background (Fig. 10.3B);
- to remove cosmic rays;
- apply smoothing, if necessary;
- apply silica fiber band subtraction (Fig 10.3 C);
- input of additional information related to sample unique number and histopathology class;
- data storage.

After extracting pure Raman signal from biological tissue, *Origin2019b* software receives Raman spectra for near real time batch processing by performing:

- Data input automatization
- Creation templates for
    - * Raman spectra normalization;
    - ** Raman spectra averaging;
- loading the reference dataset (e.g. the set of stored principal components);
- execution methods to perform classification between the groups of tissues, based on at least one analysis method of the acquired Raman spectrum:
    - * principal component analysis (PCA);
    - ** k-means cluster analysis;
    - *** partial least squares (PLS) regression;
    - **** discriminant analysis;
- extraction of diagnostic metrics;
- display classification plot between the tissue types;
- display classification accuracy results;
- calculation of receiver operating characteristic (ROC) for discrimination between pairs of:
    - * seborrheic keratosis *vs* pigmented skin lesions;
    - ** between pigmented skin lesions;
- calculation of posterior probability for each measured tissue to be classified as seborrheic keratosis, combined nevus or dermal/junctional nevus;
- display and storage of classification output.

Raman spectral data analysis can be used separately or in combination with image analysis. The input data comprise loading Raman spectral data within the wavenumber range of 600 – 1800 cm^{-1} and loading four sets of images within 1185 – 1409, 1217 – 1456, 1651 – 1747 and 1674 – 1775 cm^{-1} wavenumber subranges. Software used for processing Raman spectroscopy data leads to generating metrics for tissue classification, based upon the features of Raman spectra, while image analysis derives the distribution of Raman scattered light intensity corresponding to the analysed wavenumber sub-ranges.

Data processor initially executes the software configured to process a Raman spectrum decomposing it into components corresponding to the Raman spectra of specific molecules within issue. This is a first step of Raman spectra analysis that allows obtaining diagnostic metrics from direct identification of Raman

spectral features, indicating whether a tissue is more likely affected by seborrheic keratosis or is it a type of pigmented nevi.

The second step is to extract the various metrics based on the applied method of multivariate data analysis for determination of the tissue type. After the loading the Raman spectra, the software derives the first set of metrics based on PCA, classifying which of the type of tissue was measured (seborrheic keratosis or nevus). Particularly, Raman spectrum processing involves assessing PC loadings and scores for multiple PCs. For additional metrics, processing of the Raman spectra may include evaluation of the PLS factor scores over many predetermined PLS factors. For additional spectra analysis, the principal component scores are determined for multiple PC and a canonical discriminant analysis is applied to the PC scores (or PLS factor scores). The embedded ROC plot reveals the sensitivity and specificity for identification between two groups of tissues.

Optionally, the software also allows diagnostic metrics to be obtained, showing the type of nevus. For more efficient classification of nevus, the program is designed to rely only on the reduced wavenumber range. For example, the software is configured in a way, to derive the first metrics from the whole Raman spectrum (600 - 1800 cm^{-1}) to discriminate combined nevus from dermal/junctional nevus, then the second metrics to discriminate between nevi repeatedly, by using the reduced wavenumber range, e.g. using high (1250 – 1800 cm^{-1}) or low (600 – 1250 cm^{-1}) subranges. Each correctly identified spectrum is added into a database that can be used further as a reference spectra for tissue discrimination. The same data analysis algorithm type can be also executed for differentiation between seborrheic keratosis and nevi. The multiple data subranges can be also used for spectral data analysis, matching with the wavenumber regions for Raman band imaging at 90% filter transmittance level.

The next step of patient data analysis incorporates the user selectable mode for execution of image analysis algorithms, configured to process Raman macro images of tissues. The macro-images acquired from $1cm^2$ sample area are displayed in grayscale (or in pseudo colours) in a figure window of *Andor Solis 4.1* software. For selected Raman band of interest, the final image of Raman scattered light is computed by subtracting two images at peak transmitted wavenumbers. More functions can be selected (+; -; *; /) based upon the user demand. The pseudo colouring technique optional to create the contrast maps corresponding to the spatial location of Raman spectral band of interest enhanced by image subtraction. The ROI of the processed image can be selected manually and exported as a *.jpeg file. Advanced algorithms for classification of skin lesion in specific areas of 2D image plane with capability to recognize specific cancer type are under development.

A3.4. Clinical validation of the Raman imaging technology: volunteer measurements

November 2019 – October 2020

The main contributors: Res.assist. Anna Berzina, Dr.phys. Mindaugas Tamosiunas

Raman spectra analysis was carried out using iHR320 spectrophotometer data, processed by *OriginLab 9* software for PC analysis, as described above. A total spectra of 17 patients were analysed, who attended multimodal diagnostics (Raman, AF lifetime and multispectral imaging) procedures at University of Latvia, Institute of Atomic Physics and Spectroscopy. The histological dataset for the 17 patients is presented in Table 13-1, which highlights the distribution of four sample groups: dermal nevus, junctional nevus, combined nevus and seborrheic keratosis. Only a single Raman spectrum was collected per patient for the most of the lesions.

Two approaches were tested to analyse Raman spectral data: i) direct identification of Raman spectral features; ii) application of multivariate data analysis. The spectra resulting from averaging four different groups of tissues are displayed in Figure 12-1. One of the first evidences of benign epithelial tumor, seborrheic keratosis presence, is in the Raman spectral bands located near 1127 and 1248 cm^{-1}. The most intense Raman peak for seborrheic keratosis was located near 813 cm^{-1} with other major Raman bands present at 939, 1458, 1552 and 1659 cm^{-1}. Other skin lesions investigated have lower intensities at 939, 1342, 1552, 1659 and 1762 cm^{-1}, in comparison to seborrheic keratosis. With the support of references [5, 6, 8], the peak assignments of Raman bands are described in Table 11-3.

Table 13-1. Data on the diagnosed lesions and patients.

Patient #	Lesion type
119	Combined nevus
122	Junctional nevus
123	Combined nevus
124	Junctional nevus
124-2	Junctional nevus
125	Junctional nevus
126	Combined nevus
129	Combined nevus
14th Oct (patient #1-1)	Dermal nevus
14th Oct (patient #1-2)	Seborrheic keratosis
14th Oct (patient #2)	Dermal nevus
14th Oct (patient #4)	Seborrheic keratosis
14th Oct (patient #5)	Combined nevus
14th Oct (patient #6)	Dermal nevus
14th Oct (patient #10)	Dermal nevus
14th Oct (patient #11)	Dermal nevus

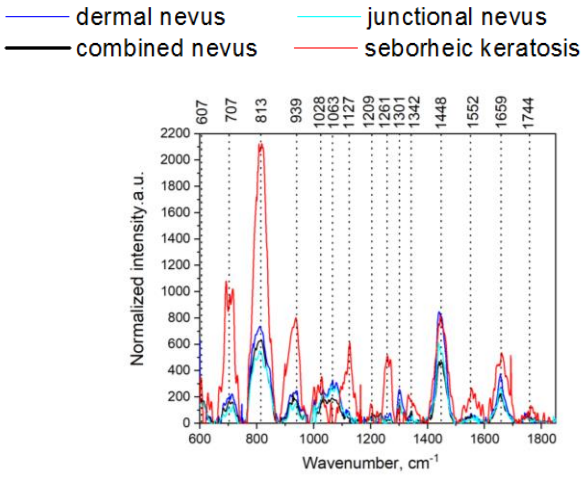

Figure 13-1. Mean Raman spectra of the examined skin lesions.

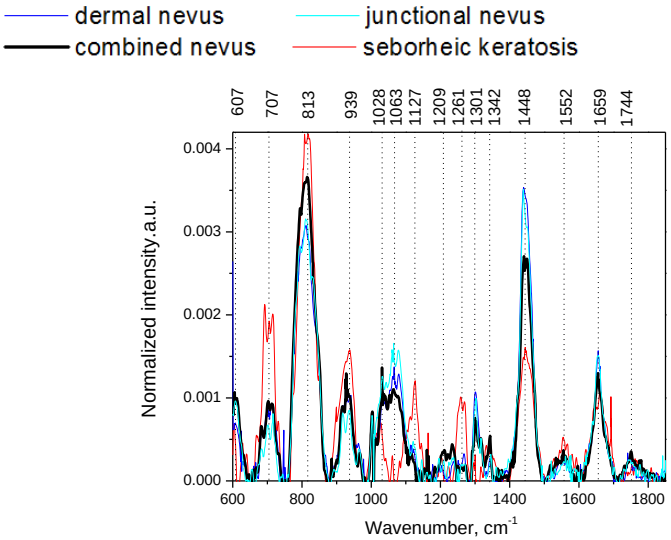

Figure 13-2. Area normalized mean Raman spectra of the examined skin lesions

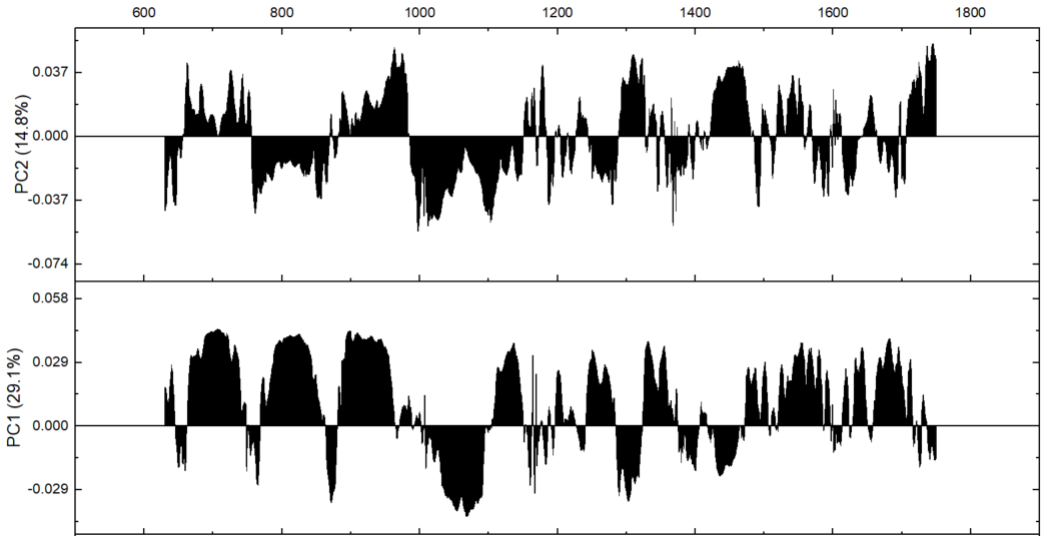

Figure 13-3. The loading plot of PC1 and PC2.

Raman spectra were normalized to their area under the curve to extract the differences related to the spectral shape (Fig. 13-2). All normalized spectra demonstrated similar Raman peaks however the relative intensities varied among the skin lesions. Pigmented skin lesions such as dermal nevus, junctional nevus and combined nevus had higher relative intensities at 813, 1028, 1063, 1301 and 1448 cm^{-1} after normalization.

The elevated Raman intensity near 1380 cm^{-1} and 1580 cm^{-1} indicate the presence of melanin [9]. Raman signal from melanin was previously reported to be higher for pigmented lesions, such as nevus, than that of seborheic keratosis [8]. Conversely, our study suggest that melanin signal did not effect significantly on the spectra shape and intensity, indicating the importance of selection other non-melanin based criteria for tissue differentiation. For example, tyrosin an phenylalanine serve as the precursors for melanin synthesis in human skin and few reports suggested the possibility of tryptophan as the precursor for melanin synthesis [10]. Indeed, our study revealed that pigmented lesions differentiate from seborrheic keratosis by the elevated Raman intensity corresponding to phenylalanine (1031 cm^{-1}) and tryptophan (1016 cm^{-1}) spectral bands.

Spectra corresponding to nevi were very similar by the spectral shape, despite belonging to different patients. The strongest variation of Raman peak intensity between dermal nevus, junctional nevus and combined nevus was found at 813 cm^{-1} and 1448 cm^{-1}. The Raman bands centred at 1028, 1063 and 1301 cm^{-1} were absent for seborrheic keratosis lesions.

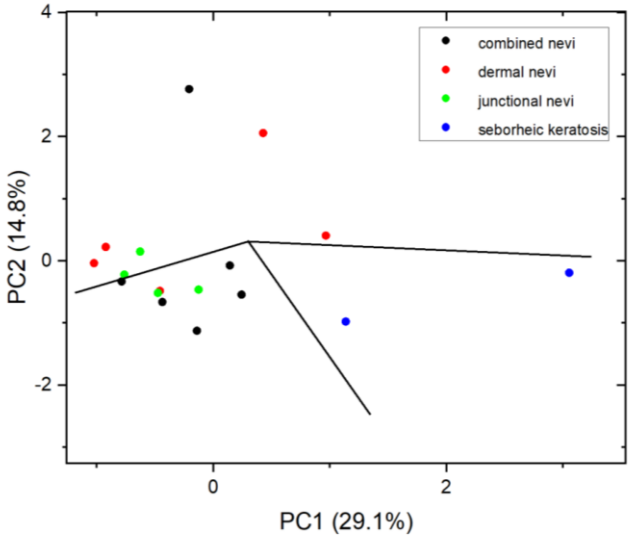

Figure 13-4. The scatter plot of PC1 and PC2 scores.

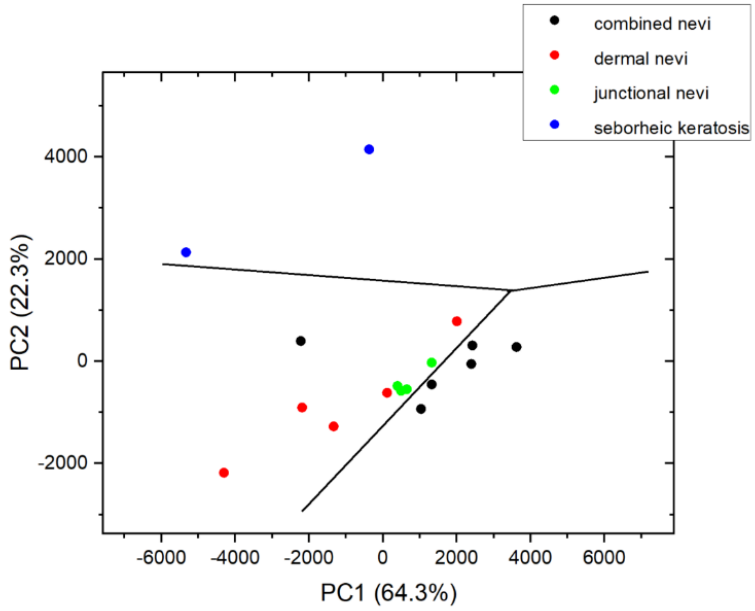

Figure 13-5. The scatter plot of PC1 and PC2 scores for 1250 -1750 cm^{-1} spectral region, without spectra normalization to the area under the curve.

The principal component (PC) analysis extracts the most important variations that occur in tissue spectra, contributing to the discrimination of tissue type. Figure 13-3 shows the loading plot of PC1 and PC2 in 600 – 1750 cm^{-1} spectral region. The loadings represent the weights for each original variable identifying which variables have the largest effect on each PC. The score plot of the first two PCs is shown in Fig. 13-4, which included 43 % of all spectral variations. In order to separate between the tissue types, the diagnostic lines were manually drawn. Based on different combinations between PC1 and PC2 scores, the seborrheic keratosis and different nevus tissues can be clustered into the separate groups. The sensitivity and specificity results, relevant for diagnosis for the type of nevus (a) or between seborrheic keratosis and nevus are indicated in Table 13-2. Junctional nevi and dermal nevi could not be separated by PCA analysis.

Table 13-2. Results of tissue discrimination (sensitivity, specificity).

	Discrimination based on PCA score		
Histopathology	Dermal & Junctional nevi	Combined nevi	Seborheic keratosis
Dermal & junctional nevi (9)	6	3	0
Combined nevi (6)	1	5	0
Seborheic keratosis(2)	0	0	2
Sensitivity	[a]100 %; [b]66%		
Specificity	[a]100%; [b]83.3%		
Dermal & junctional nevi (9)	9	0	0
Combined nevi (6)	1	5	0
Seborheic keratosis(2)	0	0	2
Sensitivity	[a]100 %; [b]100%		
Specificity	[a]100%; [b]83.3%		

[a] percentage chance that the test will correctly identify seborrheic keratosis compared to both nevi;
[b] considering the differential diagnosis between combined nevi and dermal/junctional nevi.

Previous research has shown that it was necessary to normalize the data before performing PCA [11, 12, 13]. However, PCA resulted in a score plot separating seborrheic keratosis and nevi without overlapping areas, when the normalization step was skipped during the diagnostic algorithm implementation and the Raman spectral region was limited to 1200 - 1750 cm^{-1} (Figure 13-5). Although junctional nevi could not be distinguished from dermal nevi, the score plot explained increased number (86 %) of spectral variations and the PCs gained the capability to discriminate between combined nevi and dermal/junctional nevi with higher sensitivity.

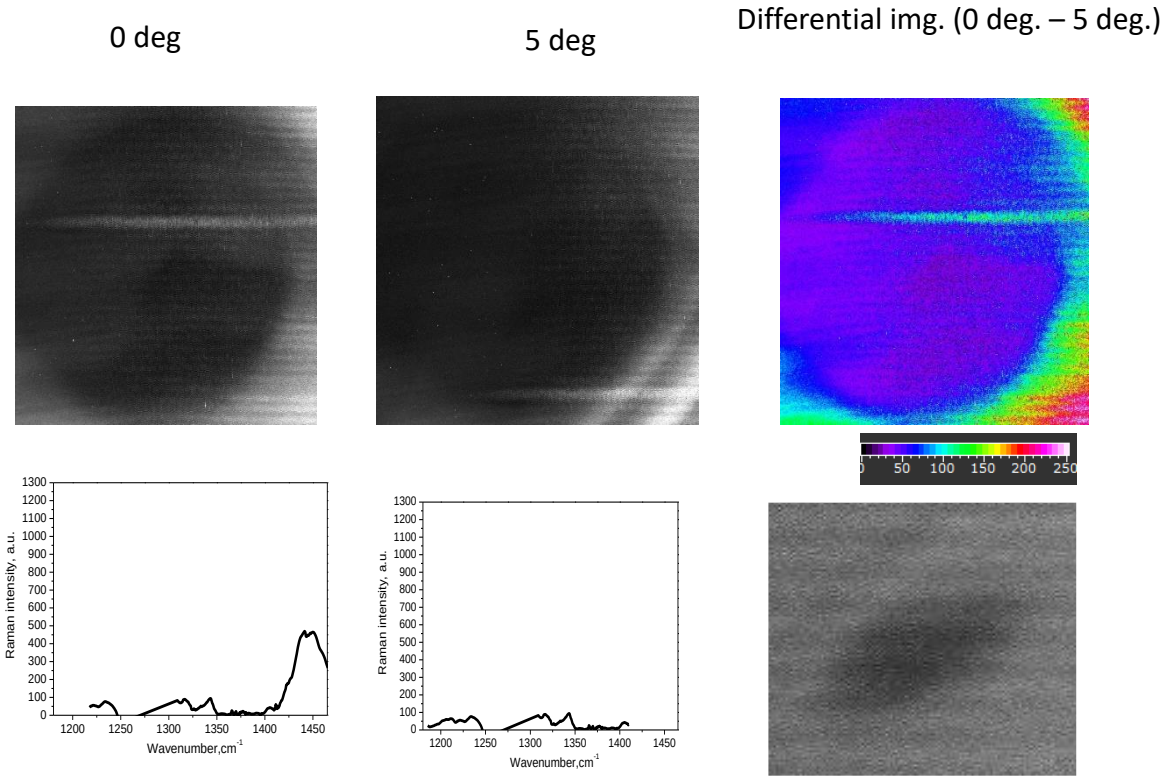

Figure 13-6. Raman imaging *in vivo:* combined nevus, filter #1.

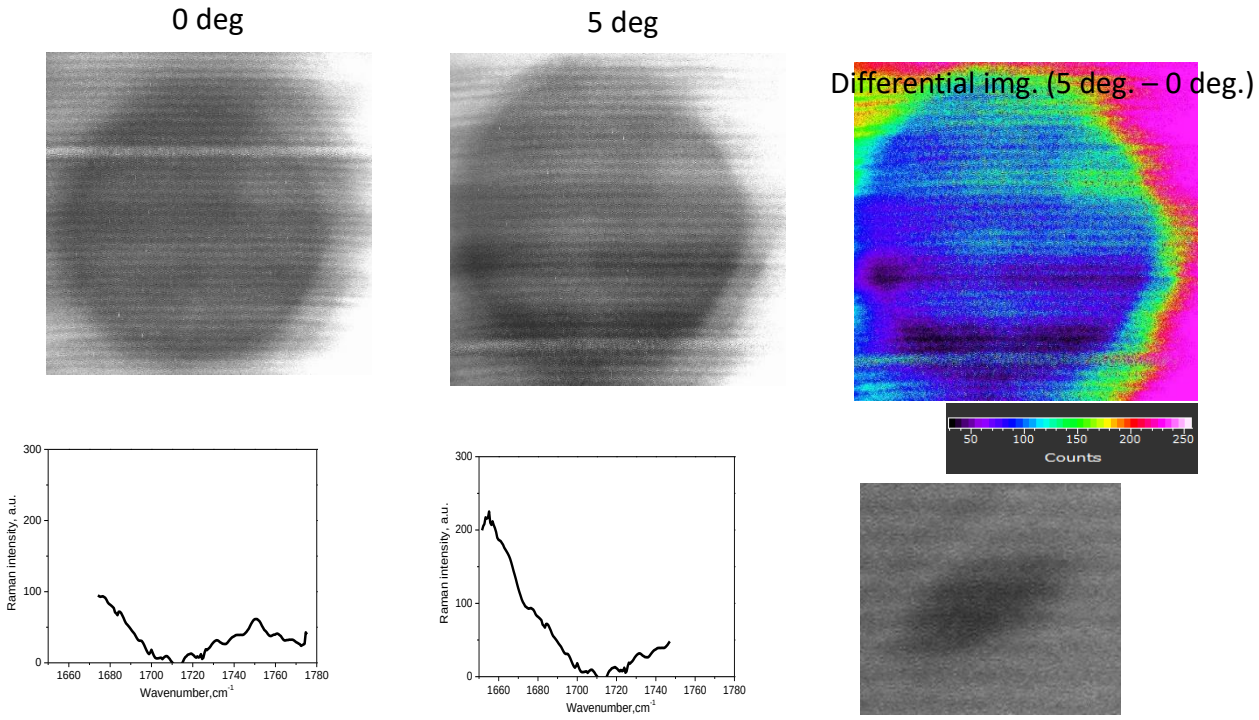

Figure 13-7. Raman imaging in vivo: combined nevus, filter #2.

The spectral region of 1200 – 1750 cm^{-1} was further tested for Raman spectral band imaging *in vivo*. We challenged such diagnostic technology to image the lowest Raman spectral intensity tissues, such as combined nevus being surrounded by the normal skin. Combined nevus exhibits up to 1.5 times lower Raman signal compared to dermal/junctional nevi or seborrheic keratosis at 1448 cm^{-1} or at 1659 cm^{-1} (Fig. 13-2). As indicated in Fig. 13-6, to obtain the image that shows only the Raman band emission from combined nevus, we subtracted background signals of nevus tissue captured at 5 deg. filter #1 rotation from image captured at 0 deg. filter #1 rotation. Similar results on the differential Raman intensity of combined nevus Raman have been also measured by using tunable filter #2 (Fig. 13-7). The image of combined nevus has been achieved due to the enhanced Raman signal of nevus at 5 deg. filter rotation.

We intend to continue this work with clinical imaging applications, promoting the method of fast and wide-field Raman imaging.

References related to A4:

1. N. J. Crane, T. S. Brown, K. N. Evans, J. S. Hawksworth, S. Hussey, D. K. Tadaki, and E. A. Elster, "Monitoring the healing of combat wounds using Raman spectroscopic mapping," Wound Repair and Regeneration, vol. 18, pp. 409-416, 2010.
2. D. T. Downing, "Lipid and protein structures in the permeability barrier of mammalian epidermis," J. Lipid Res. 33(3), 301–313 (1992).
3. Safety of laser products – Part 1: Equipment classification and requirements. 2007, CENELEC.
4. A. Papour, J.H. Kwak, Z. Taylor, B. Wu, O. Stafsudd, W. Grundfest, "Wide-field Raman imaging for bone detection in tissue," Biomed. Opt. Express, vol. 6 (10), pp.3892-3897, 2015.
5. L. Silveira, C.A. Pasqualucci, B. Bodanese, M.T.T. Pacheco, R.A. Zângaro, "Normal-subtracted preprocessing of Raman spectra aiming to discriminate skin actinic keratosis and neoplasias from benign lesions and normal skin tissues," Lasers Med Sci, vol. 35, pp.1141-1151, 2020.
6. X. Feng, A.J. Moy, H.T.M. Nguyen, J. Zhang, M.C. Fox, K.R. Sebastian, J.S. Reichenberg, M.K. Markey, J.W. Tunnell, "Raman active components of skin cancer," Biomed Opt Express, vol. 8 (6), pp. 2835-2850, 2017.
7. J. Spigulis, I. Kuzmina, V. Lukinsone, M. Tamošiunas, I. Oshina, L. Ozolina, A. Maslobojeva, M. Kuzminskis, D. Ivanov, E. Borisova, "Towards combined multispectral, FLIM and Raman imaging for skin diagnostics," Progress in Biomedical Optics and Imaging - Proceedings of SPIE, 11232, art. no. 112320N, 2020.
8. A.M.F. Lima, C.R. Daniel, R.S. Navarro, B. Bodanese, C.A. Pasqualucci, M.T.T. Pacheco, R.A.Zângaro, L. Silveira, "Discrimination of non-melanoma skin cancer and keratosis from normal skin tissue in vivo and ex vivo by Raman spectroscopy," Vibrational Spectroscopy, vol. 100, pp. 131-141, 2019.
9. Z. Huang, H. Lui, M.X.K. Chen, A. Alajlan, D.I. McLean, H. Zeng, "Raman spectroscopy of in vivo cutaneous melanin," J. Biomed. Opt, vol. 9(6), pp.1198–1205 (2004).
10. S. Ahmad, M. Mohammed, L.P. Mekala, S. Chintalapati, V.R. Chintalapati, "Tryptophan, a Non-canonical Melanin Precursor: New L-tryptophan Based Melanin Production By Rubrivivax Benzoatilyticus JA2," Scientific Reports, vol. 10(1), p. 8925, 2020.
11. S.J. Baek, A. Park, J.Y. Kim, S.Y. Na, Y. Won, J. Choo, "Detection of basal cell carcinoma by automatic classification of confocal raman spectra". Proceedings of the 2006 international conference on Computational Intelligence and Bioinformatics - Volume Part III. Springer-Verlag, Berlin, Heidelberg, pp. 402-411, 2006.
12. B. Bodanese, F.L. Silveira, R.A. Zângaro, M.T. Pacheco, C.A. Pasqualucci, L. Silveira, "Discrimination of basal cell carcinoma and melanoma from normal skin biopsies in vitro through Raman spectroscopy and principal component analysis," Photomed Laser Surg, vol. 30(7), pp. 381-387, 2012.
13. E. Brauchle, S. Noor, E. Holtorf, C. Garbe, K. Schenke-Layland, C. Busch, "Raman spectroscopy as an analytical tool for melanoma research," Clin Exp Dermatol. vol. 39(5), pp. 636-645, 2014.